Modélisation de la mécanique de la cellule et son noyau dans le cadre de la migration confinée

Solenne Deveraux

▶ To cite this version:

Solenne Deveraux. Modélisation de la mécanique de la cellule et son noyau dans le cadre de la migration confinée. Autre. Université Paris Saclay (COmUE), 2018. Français. NNT : 2018SACLC063 . tel-01968076

HAL Id: tel-01968076
https://theses.hal.science/tel-01968076

Submitted on 2 Jan 2019

université
PARIS-SACLAY

CentraleSupélec

NNT : 2018SACL063

THESE DE DOCTORAT
DE
L'UNIVERSITE PARIS-SACLAY
PREPAREE A
CENTRALESUPELEC

ECOLE DOCTORALE N° 579
Sciences Mécaniques et Énergétiques, Matériaux et Géoscience

Spécialité de doctorat : Génie Mécanique

Thèse présentée et soutenue à Gif-sur-Yvette, le 11 septembre 2018, par

Mme Solenne Mondésert-Deveraux

Modeling cellular and nuclear mechanics in the context of confined migration

Composition du Jury :

M. Jose Muñoz	Associate Professor, Universitat Politècnica de Catalunya	Rapporteur
M. Claude Verdier	Directeur de recherche CNRS, Université Grenoble Alpes	Rapporteur
M. Abdul Barakat	Directeur de recherche CNRS, École Polytechnique	Examinateur
Mme Nathalie Lassau	Professeur, Université Paris-Sud	Examinateur
M. Yves Rémond	Professeur, Université de Strasbourg	Président du Jury
M. Denis Aubry	Professeur, CentraleSupélec	Directeur de thèse
Mme Rachele Allena	Maître de conférences HDR, ENSAM	Co-Directrice de thèse

"All models are wrong, but some are useful."
George E. P. Box

Acknowledgements

This thesis is the result of three years of work, collaboration and sharing with great people to whom I wish to express my deepest gratitude.

First and foremost, I would like to say a huge "Thank you" to my two PhD advisors, Denis Aubry and Rachele Allena, for pushing me forward, supporting me and helping me grow all along this journey, through animated, but always cheerful, meetings. The shortest speeches always being the best, I will stop at that, despite all there would be to be thankful for.

Then, I would like to thank all the persons who made my stay at Cornell University possible. First, Bertrand David who took the time to teach me about cell culture and experimental biology before I left. Then, a special thanks to Jan Lammerding for welcoming me into his lab so generously. Eventually my gratitude goes to all his students who took upon their time to teach me, show me around and even hosted me: Pragya, Alex, Emily, Philipp, Greg and Ashley.

If there is a lot of work involved in a PhD, there were also a lot of friendship moments. Thank you to all those with whom I shared an office, particularly to Xue, Marwa, Ahmed, Khalil, Hélène, Matthieu, Gabriel and Marion, and to everyone from the lab for the good times shared around a tea cup !

Coming to the end, I thank deeply Jose Muñoz and Claude Verdier who accepted to reed my thesis and provided me with their insightful reviews. My gratitude also goes to Yves Rémond, for accepting to be president of my jury, and to the other members of my jury for their presence at my defence. A special thank you to Nathalie Lassau, who also supervised my educational journey at Gustave Roussy which nurtured my scientific interest for clinical issues and helped me define my professional project.

Last but not least, I would like to thank my flatmates, Brune and Claire-Marie, my whole family, and more particularly my husband, for their support during this thesis and their constant curiosity for this little cell passing by on my computer screen. Thank you to all those who came to my defence to surround and support me on this day: it meant a great deal to me.

Contents

Introduction

Cells are the fundamental units of life. If we look at a living organism and try to unveil what lies behind its global function, we may consider it as a sum of its organs: a human being for instance is made up of skin, bones, muscles, a beating heart, lungs, a liver, a stomach, etc... Going further down, we can wonder what governs the function or malfunction of these organs, what is the underlying structure keeping it all together. At some point, we get down to cells: the smallest autonomous life unit. In a multicellular organism, cells are not isolated. They constantly interact with each other and with their environment to ensure the biological processes essential to life. From the very dawn of life, during embryogenesis, to potential lethal diseases, like tumor metastasis, one characteristic of cells is persistent: their ability to migrate from one site to another. Nonetheless, migration within an organism is not a trivial process. Indeed, the surrounding cells and extra-cellular matrix create a dense and confined environment in which cells cannot move freely. To migrate to the right place at the right moment, cells must then develop strategies to overcome obstacles and perform their mission within the organism. This capacity is a crucial property of multicellular organisms to ensure their development and their homeostasis. Cell migration can indeed occur in response to various situations, such as a mere need to feed, or a stimulus that could be chemical or mechanical. These stimuli may originate from larger vital biological processes that govern the activity of the organism : morphogenesis of embryos, which requires cells to be able to migrate to a very specific and potentially distant location, or homeostasis of adult organisms. Therefore, a pathologically impaired cell migration can have disastrous effects on the development of the organism, resulting in birth defects, autoimmune syndrome, ineffective wound healing or tumor metastasis. The latter is estimated to be responsible for 90 % of cancer deaths [Chaffer and Weinberg, 2011], thus emphasizing the emergency of better understanding the mechanics of confined cell migration. Let us dive inside the cell to fathom its internal structure and mechanical behaviour.

Making a close up on a eukariotic cell (see Fig. 1), the first thing to be seen is the plasma membrane that surrounds the cytoplasm in which all organelles bathe. It is composed of a double layer of phospholipids with embedded protein complexes assuring the communication between the environment and the interior of the cell. In

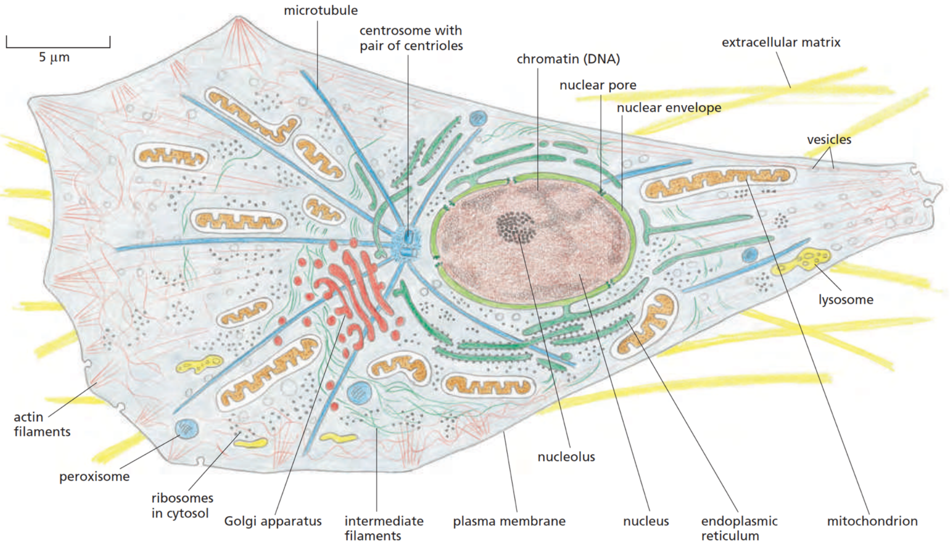

Figure 1: Internal structure of a eukariotic cell [Alberts et al., 2014].

the cytoplasm, we can find mitochondria (the power units of the cell), the endoplasmic reticulum (the proteins and lipids factory), the Golgi apparatus (the macromolecules transport center),ribosomes (the interpreters from genetic information to proteins) and the cytoskeleton (the backbone of the cell, composed of various types of filaments, that can adapt to the environment (its stiffness for instance [Abidine et al., 2018]). The nucleus, the largest organelle of all, is made up of a nuclear envelope and a lamina enclosing and protecting the nucleoplasm where the chromatin, i.e. the genetic material, can be found (see Fig. 2).

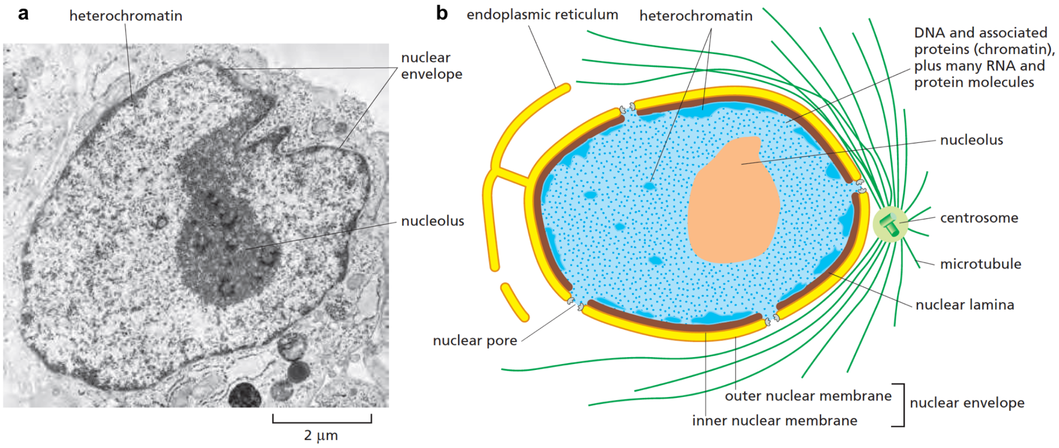

Figure 2: A cross-sectional view of a typical cell nucleus. a) Electron micrograph of a thin section through the nucleus of a human fibroblast and b) Schematic drawing of the nucleus [Alberts et al., 2014]

To efficiently shield the chromatin from extensive deformation and potential genetic damage, the lamina is much stiffer than the cytoplasm. Then, the nucleus may impede the ability of cells to migrate in a confined environment. Interestingly enough, cells can adopt different migratory behaviours in order to overcome obstacles. Depending on the cell type, its environment and the force ratio between adhesion, contraction and actin-network polymerization, cells are able to rapidly switch from one behaviour to the other (see Fig. 3). Migration can occur collectively as a group of cells moving to a specific location, or individually as an immune cell translocates to the inflammation site or a cancerous cell leaving the primary tumor for instance. Rapid single cell crawling is usually referred to as 'amoeboid' migration, in opposition to the slower 'mesenchymal' migration. The former gathers various migration modes that all have in common the cyclic protrusion and retraction of cellular extensions, i.e. active cell deformation during the migration process. These modes can fall into two main categories: protrusive and contractile. Protrusive migration mostly relies upon actin-network polymerization of pseudopods while, in contractile migration, the contraction of the acto-myosin network drives the formation of blebs – actin-free protrusions – as will be later developed in this manuscript. Eventually, the cell can use a combination of these strategies to enhance the migration efficiency.

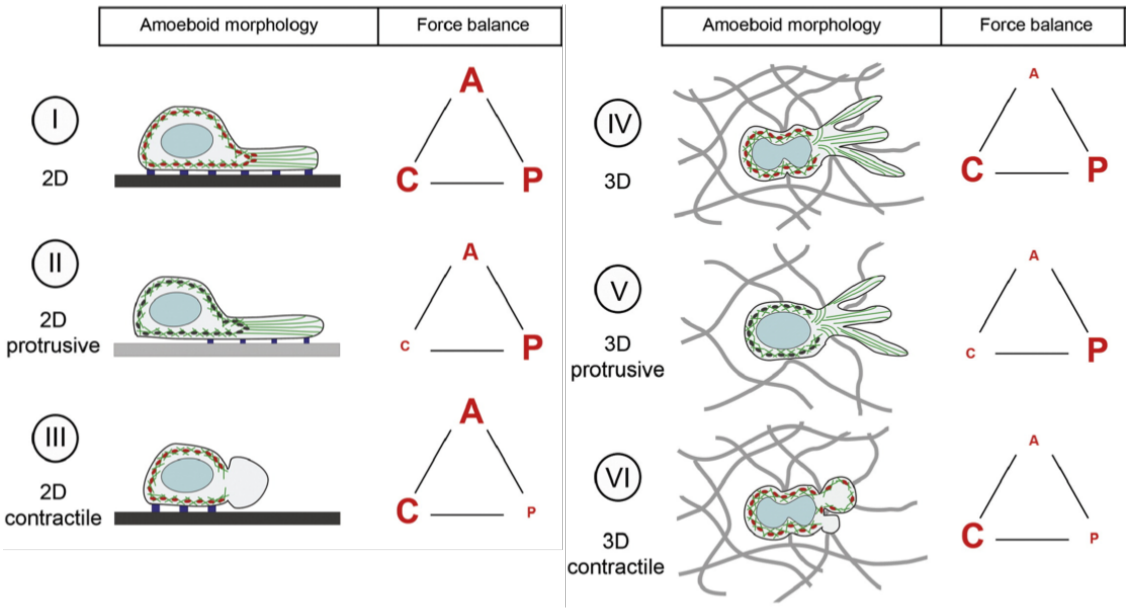

Figure 3: The force-relationship between adhesion, contraction and polymer-network expansion determines the 'amoeboid' phenotype. The three major forces in cell migration are adhesion (A), contraction (C) and polymer-network expansion (P). The color code is the following: actin filaments in green, Myosin-II as red ellipses (black ellipses if this function is impaired), adhesions points in blue, fibrillar network in gray and cell nucleus in light blue. Thick black lines represents high adhesive surfaces while thick gray lines stand for low adhesive surfaces [Lämmermann and Sixt, 2009]

In this thesis, we aim at further unveiling the mechanisms behind cell migration in confined environment. When confined, the cell and consequently its nucleus are strongly deformed. As there is large deformation, a few questions arise on the mechanics of this system: What are the stresses inside the cell ? Can we characterize the mechanical behaviour of cells and their constituents ? Cell migration is being extensively scrutinized under the frame of molecular biology, but the question that drives the present work really is : what can mechanics tell us about the unfolding of cell migration ? This is such a vast topic that we need to choose a relevant angle of attack. In previous work, a visco-elastic model of a cell migrating in a micro-channel was developed [Aubry et al., 2014]. Taking that model as a starting point, we choose to tackle three questions, raised by experimental observations from biologists, that will be addressed in the first three chapters:

1. First, we investigate the mechanical behaviour of the nucleus and its interaction with the cytoplasm during the passage through a sub-nuclear constriction.
2. Then, we focus on one particular migration mode called 'chimneying' and the mechanism allowing the confined cell to move efficiently without adhesions.
3. Eventually, we developed a model to explore the behavior of the nucleus during the spreading of cells on a micro-pillared substrate and answer that question: is the nucleus being pushed or pulled towards the bottom of the substrate ?

Given the great variability of parameters found in the literature, all three models will feature a generic cell type rather than a specific one. If need be, the mechanical parameters can then be adapted to fit a particular phenotype. All our results have been (or are in the process of being) published. The model of the nucleus has been published in *Journal of Theoretical Biology* [Deveraux et al., 2017], the chimneying model has been accepted for publication in *Molecular Cell Biology* and the spreading model has been submitted to *Physical Biology*.

Bibliography

Abidine, Y., Constantinescu, A., Laurent, V. M., Rajan, V. S., Michel, R., Laplaud, V., Duperray, A., and Verdier, C. (2018). Mechanosensitivity of Cancer Cells in Contact with Soft Substrates Using AFM. *Biophysical Journal*, 114(5):1165–1175. 12

Alberts, B., Johnson, A., Lewis, J., Morgan, D., Raff, M., Roberts, K., and Walter, P. (2014). *Molecular Biology of the Cell*. Garland Science, New York, NY, 6 edition. 12, 153

Aubry, D., Thiam, H., Piel, M., and Allena, R. (2014). A computational mechanics approach to assess the link between cell morphology and forces during confined migration. *Biomechanics and Modeling in Mechanobiology*, 14(1):143–157. 14

Chaffer, C. L. and Weinberg, R. A. (2011). A Perspective on Cancer Cell Metastasis. *Science*, 331(6024):1559–1564. 11

Deveraux, S., Allena, R., and Aubry, D. (2017). A numerical model suggests the interplay between nuclear plasticity and stiffness during a perfusion assay. *Journal of Theoretical Biology*, 435:62–77. 14

Lämmermann, T. and Sixt, M. (2009). Mechanical modes of 'amoeboid' cell migration. *Current Opinion in Cell Biology*, 21(5):636–644. 13, 153

Chapter I

Mechanical behaviour of the confined nucleus

Contents

I.1 Introduction

Cancerous cells are not only subject to various genetic and molecular modifications, but they also display altered mechanical properties. Their nucleus ,particularly, can be made softer and more prone to breaking [Davidson and Lammerding, 2013]. During confined migration, as occurs in cancer metastasis, cells endure substantial deformations to squeeze through tight gaps as small as 10% of the size of the nucleus [Friedl et al., 2011; Wolf et al., 2013]. As the largest and stiffest organelle, the nucleus can strongly impedes migration [Zwerger et al., 2011] and a softer or weaker nucleus enhances the migratory abilities of the cell [Bell and Lammerding, 2016; Denais et al., 2016]. Most publications investigate cancer metastasis [Wolf and Friedl, 2006], mechanical properties of the nucleus [Friedl et al., 2011] and mechanical coupling between the nucleus and the cell's cytoskeleton [Schwartz et al., 2017; Skau et al., 2016] under the spectrum of molecular biology. Our aim here is to tackle these issues through a purely mechanical perspective. Since nuclear mechanics is at stake here, numerical simulation appears as a very interesting tool to investigate the mechanical interplay between cellular components, such as the lamina and the cytoplasm, and to get new insights on some biological assumptions. As for quantitative values of the cell mechanical parameters, many techniques are accessible to study specific features of the nucleus, as will be discussed in the following paragraphs.

I.1.1 Structures of the nucleus

We first need to apprehend further the internal organization of the nucleus in order to understand its behaviour. Its mechanical properties mainly arise from two components: the lamina – a dense meshwork composed of A-type (lamin A/C), B-type lamins and lamin-associated proteins [Ho and Lammerding, 2012] – and the nucleoplasm. The components of the nucleus interact with each other and with the cytoskeleton through protein complexes in order to transmit mechanical information throughout the cell (see Fig. I.1). Various studies have shown that Lamin A/C is the dominant protein in determining nuclear stiffness and structural stability and its decrease correlates with an increase in nuclear fragility [Zwerger et al., 2015]. Also, Lamin A/C upregulation could improve resistance of the cell to high shear stress[Mitchell et al., 2015]. Lamin A/C has been thoroughly investigated since its expression levels can widely vary from one cell to another and it is involved in many diseases that impact cell mechanics, such as laminopathies [Dialynas et al., 2015; Ho et al., 2013; Mitchell et al., 2015; Schäpe et al., 2009; Zwerger et al., 2013]. Additionally, it was found to play a great role in the ability of cells and nuclei to adjust their stiffness to that of the surrounding environment [Guilluy et al., 2014; Schwartz et al., 2017]. On the contrary, the role of lamin B is not understood as deeply. Some studies suggest that it has a minor effect on nuclear mechanics although disruption of these lamins may be lethal during brain development [Jung et al., 2013]. The lamina surrounds and protects the nucleoplasm which is mostly made up of chromatin: densely packed DNA that is organized and compacted around various proteins, such as histones, to form chromatin fibers. It should be noted that other bodies are present inside the nucleus, as well as a nucleoskeleton. The latter is made of structural proteins like actin, spectrin, myosin or lamins that may be involved in chromatin organization and thus in the nucleoplasm mechanical behaviour [Dahl and Kalinowski, 2011; Naetar et al., 2017]. In the decades following the discovery of its structure, the DNA double-helix was described as an elastic rod and, later, as a worm-like chain [Smith et al., 1992; Marko and Siggia, 1995; Bustamante et al., 2003]. In the nucleus, the DNA strands, as well as the other nuclear bodies, are surrounded by fluid: the nucleoplasm can thus be seen as a viscoelastic material. The lamina however, as a dense meshwork where fluid cannot circulate, can be seen as a solid elastic material [Rowat et al., 2006]. With sheer observation of its internal organization, we can already qualitatively propose a visco-elastic model of the nucleus.

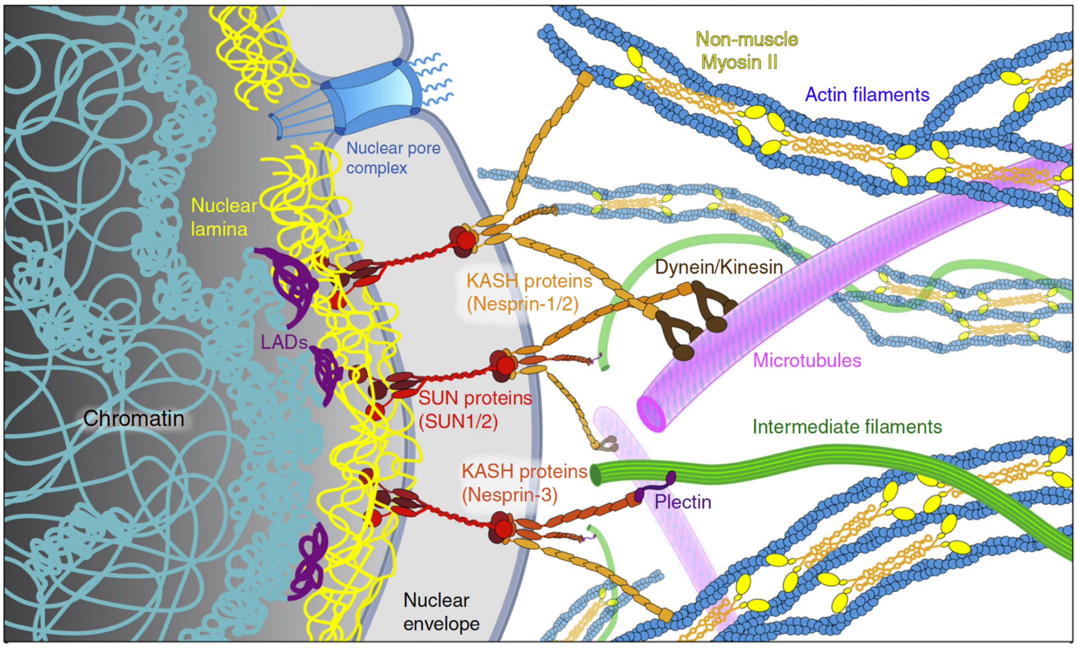

Figure I.1: Schematic overview of the internal organization of the nucleus and its connection to the cytoskeleton. Inside the nucleus, chromatin interacts with lamins at lamina-associated domains (LADs). Various proteins proteins form the LINC complex that mechanically couples the nuclear interior with the cytoskeleton. Modified from [McGregor et al., 2016]

I.1.2 Experimental techniques to probe the nucleus

A wide range range of experimental techniques are available to investigate the mechanical properties of the different components of the cell, and more specifically the nucleus, at various scales [Lim et al., 2006] (see Fig. I.2). Most of the them give access to a global mechanical information on the whole nucleus (perfusion [Isermann et al., 2012], micropipette aspiration - possibly coupled with relaxation experiments - [Guilak et al., 2000], microplate compression [Caille et al., 2002], substrate strain, shear flow or micro-pillars [Ermis et al., 2016]), while others unveil a more local information (Atomic Force Microscopy (AFM), active or passive micro-rheology through magnetic or optical tweezers [Monticelli et al., 2016], micro-needle manipulation [Lombardi et al., 2011], and cyto- and microindentation [Nava et al., 2014; Guillou et al., 2016]). The choice of the technique then determines the scale and the type of information obtained. The techniques using cells in suspension – and not adhering on a substrate – offer the advantage of reducing the bias induced by cyto- and nucleoskeleton reorganization due to substrate stiffness. These methods can also be applied to isolated nuclei, in order to get rid of the mechanical coupling with the cytoskeleton, although the results may then not reflect the reality of a nucleus inside a cell. A new non-invasive method has recently emerged: microsprectroscopy offers sub-micrometric resolution information on the viscoelastic properties of the cell components [Mattana et al., 2018]. This method appears very interesting to access unbiased parameters and the results should be closely monitored.

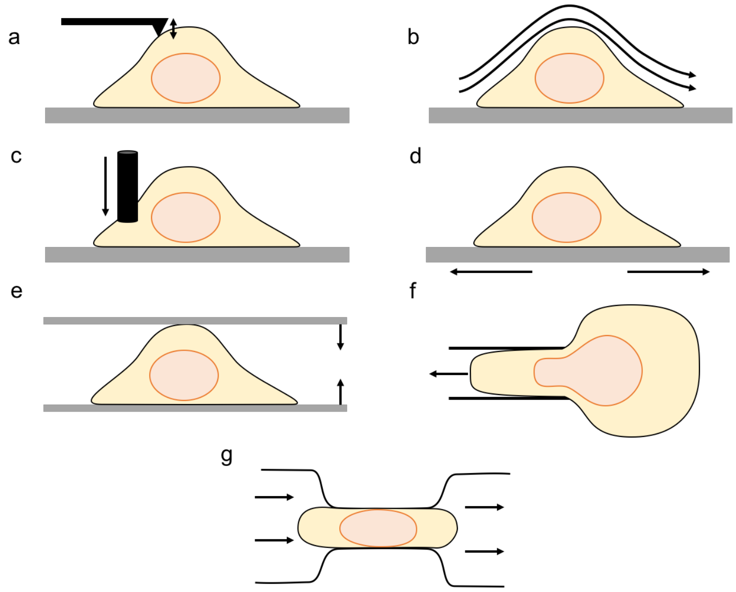

Figure I.2: Common experimental methods to probe cell and nuclear mechanics: a) AFM, b) shear flow, c) cytoindentation, d) substrate strain, e) microplate compression, f) micropipette aspiration and e) perfusion.

I.1.3 Mechanical behaviour of the nucleus

The overall nucleus

The nucleus has widely been found to behave as a visco-elastic material, all through different techniques that enlightened various specific aspects of its behaviour [Erdel et al., 2015; de Vries et al., 2007]. The perfusion and aspiration assays give a good assessment of purely passive mechanical properties of both the cell and the nucleus since they are fast enough to assume no cyto- or nucleoskeleton reorganization occurs. Indeed, cells pass through in less than a second [Isermann et al., 2012; Hou et al., 2009; Luo et al., 2014]. Such assays showed that the nucleus was 2-10 times stiffer and twice more viscous than the cytoplasm [Guilak et al., 2000; Caille et al., 2002; Lammerding, 2011]. The viscoelasticity of the nucleus is mostly accepted, but a hyperelastic behaviour of the nucleus is sometimes assumed in order to fit the simulation with the experimental data and to deduce the mechanical parameters of the nucleus [Caille et al., 2002]. Using these global measurement techniques, the Young modulus of the cell nucleus has been estimated around 0.5-8 kPa [Caille et al., 2002; Dahl et al., 2005; Guilak et al., 2000; Liu et al., 2014], but has sometimes been found to be much higher depending on the experimental method [Tomankova et al., 2012]. This illustrates one of the limits of the global techniques: they raise various uncertainties due to the interaction between the nucleus and the rest of the cell. Some recent advances in AFM techniques are used to get rid of this bias by probing the nucleus more locally [Liu et al., 2014].

The nuclear envelope (NE) and the lamina

Information on the whole nucleus is essential and easier to get, but the tight interaction between mechanical forces and gene regulation induces to look more closely and precisely at local properties of the nucleus at the scale of specific proteins such as chromatin and lamins. Studies of the nuclear envelope alone are scarce, but combined techniques of micropipette aspiration and confocal microscopy were used to characterize the nuclear envelope as purely elastic [Rowat et al., 2005]. Underlying the nuclear envelope is the lamina, a stiff material ensuring the nuclear stability, sometimes described as viscoelastic, although more thorough and velocity-dependent testing would be necessary to rigorously prove it [Swift et al., 2013; Swift and Discher, 2014]. Together, the lamina and the nuclear envelope form a very thin layer of 10-200 nm surrounding the nucleus [Gruenbaum et al., 2003]. Given the very high stiffness of the lamina, the impact of the NE, as well as the lamina's viscosity, can be neglected. The lamina protects the cell and its genetic information, but can also be a rate-limiting factor during confined migration by preventing sufficient nucleus deformation. In fact, cells have to find a good compromise between viability and motility.

The nucleoplasm

The nucleoplasm behaves as a sponge-like material that initially does not present much resistance to deformation but this resistance increases as the chromatin gets compacted [Dahl et al., 2005]. Besides, chromatin exhibits a plastic behaviour, i.e. irreversible deformation, at long time-scales and after shear stresses, which decreases with up-regulation of Lamin-A [Pajerowski et al., 2007; Deguchi et al., 2005]. This suggests that the nucleoplasm sets the rheological character of the nucleus while the lamina dictates the extent of the deformation. Such plasticity is an advantage during confined migration, since the nucleus stays elongated after going through a narrow space, making it easier for the cell to migrate through successive constrictions. Most often, the lamina is considered as the main load-bearing element in the nucleus, but recent findings suggest that chromatin itself is actually a major structural component of the nucleus [Stephens et al., 2017].

I.1.4 Computational mechanical models of the nucleus

The interest for cell computational models has been rising in the last two decades, as it becomes more and more obvious that mechanics plays a crucial role during cell migration and even in gene transcription. One strategy for representing the cell and the nucleus is discrete modeling, just considering the cell membrane or the nuclear envelope [Ujihara et al., 2011; Banigan et al., 2017]. Another is an energetic approach [Giverso et al., 2014], and finally, the cell or nucleus can be modeled through continuum mechanics [Aubry et al., 2014]. Most continuum models describe the whole cell, with or without its nucleus as a separate compartment, but fewer model focus on the isolated nucleus, as reviewed in [Vaziri et al., 2007] and [Nava et al., 2014]. The nucleus, if proven to be visco-elastic, is sometimes modeled as a hyperelastic material in order to simplify the simulation and to investigate specific mechanical issues [Caille et al., 2002; Vaziri et al., 2006; Giverso et al., 2014]. A visco-elastic model was later developed to simulate a micro-pipette aspiration assay [Vaziri and Mofrad, 2007], with the lamina and nuclear envelope taken into account. A more advanced model was proposed with the nucleus described as a poroelastic material with a plastic behaviour [Cao et al., 2016]. Interestingly, this model faithfully reproduced the irreversible deformation found in Lamin A/C deficient cells after transmigration. Although we acknowledge the validity and the interest of all these models, we observe that each one of them is designed to fit a specific experiment and can wonder whether one single model could describe several different assays. This is specifically what we aim to tackle in this chapter: a unified model of the whole cell that can be confronted with various experimental techniques.

I.1.5 Motivation for our model

Given the major role of nuclear mechanics during confined cell migration, we present here a two dimensional (2D) Finite Element (FE) implementation of a cell nucleus model, representing the nuclear lamina as elastic and the nucleoplasm as visco-elasto-plastic. Even though a three dimensional (3D) model would be more accurate, we chose a 2D representation to facilitate the computation, since it was shown that for a cell entering a micro-channel, the model is insensitive to depth [Leong et al., 2011]. Our approach is to propose a model which can be employed for both the isolated nucleus and the whole cell. While the whole nucleus is generally described as merely viscoelastic, we design a new model to be able to account for a more complex behaviours including plasticity. Besides, we aim at developing a model that is able to be tested in various experiment-like setups, but we focus here on modeling a purely passive cell to fully understand the mechanics at stake without migration or cyto- and nucleoskeleton reorganization. In this regard, we first build a model of an isolated nucleus that is tested under compression, mimicking the experimental setup from Caille et al. [2002] (see Fig. I.3 a). This model being thoroughly investigated, we implement it in a whole cell model, including also the cytoplasm, described as in previous work [Aubry et al., 2014]. This complete model is then tested to reproduce a perfusion experiment [Isermann et al., 2012] (see Fig. I.3 b). The results presented in the following sections have been published in [Deveraux et al., 2017].

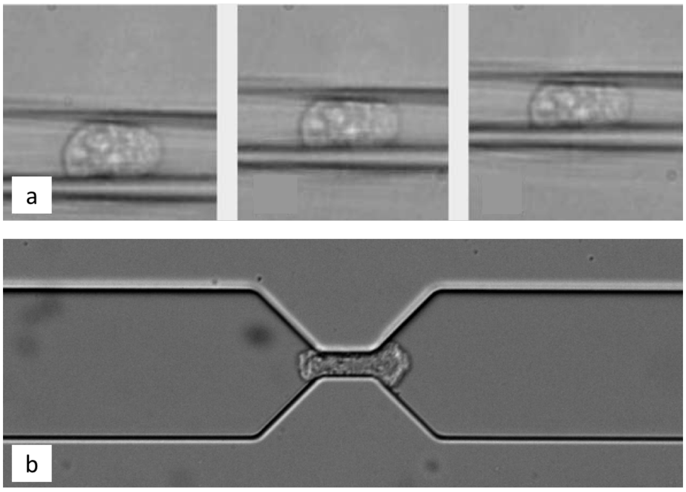

Figure I.3: Experimental setups to be reproduced by simulation: a) Microplate compression of an isolated nucleus (modified from [Caille et al., 2002] and b) Perfusion assay on MEF cells

I.2 Numerical simulation of the nucleus on a compression test

I.2.1 Nucleus geometry

The nucleus ($\Omega_{nucleus}$) has an initial circular geometry of radius $r_{nucleus} = 4\ \mu m$ and is composed of the 50 nm thick lamina (Ω_{lamina}) and the nucleoplasm ($\Omega_{nucleoplasm}$) (See Fig. I.4). Both the lamina and the nucleoplasm have been described through characteristic functions g_l and g_{np} which are a composition of a regularized Heaviside function and a level set function (see Appendices A and B). The characteristic function representing the whole nucleus is given by $g_n(\mathbf{x}) = g_{np}(\mathbf{x}) + g_l(\mathbf{x})$, where $\mathbf{x}$ indicates the current position of any particle of the system.

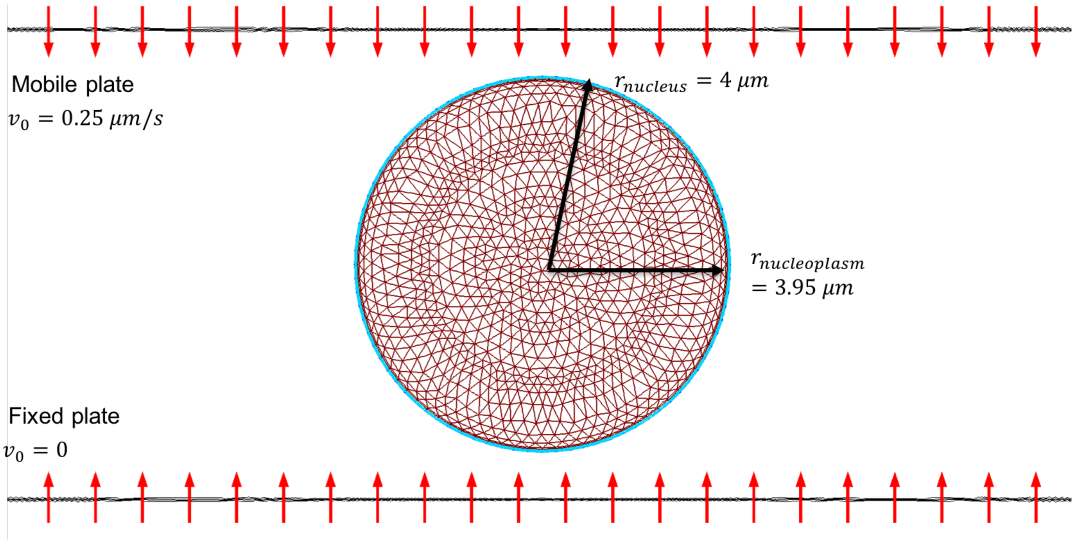

Figure I.4: Geometry of the nucleus (Dark red: nucleoplasm and Light blue: lamina) and compression plates (red arrows represent the outward normal to the plates $\mathbf{n_{plate}}$) and FE mesh

I.2.2 Constitutive model and mechanics of the nucleus

In most models, the nucleus is simply described as a viscoelastic material. In order to tackle its potential irreversible deformation, we chose to implement a visco-elasto-plastic material composed of the lamina, purely elastic, and the nucleoplasm, visco-elasto-plastic, as represented in the schema in Fig I.5. Both nuclear components are assembled in parallel since we consider the stress from both components to add up. Indeed, the lamina being very thin, the associated mesh would need to be too small. The mechanical influence of the lamina is thus not taken into account unless we homogenize the whole nucleus with volume ratios through the Voigt homogenization [Christensen, 1979] (See Equation 4). An Arbitrary Lagrangian Eulerian (ALE) formulation is used in all the simulations, which allows to consider only small strains in the moving frame and Cauchy stresses [Donea et al., 2004; Belytschko et al., 2000]. The total Cauchy stress $\boldsymbol{\sigma}_n$, where the subscript n stands for nucleus, and the small deformation tensor $\boldsymbol{\epsilon}_n$ are defined as

$$\begin{aligned} \boldsymbol{\sigma}_n &= (\boldsymbol{\sigma}_{np} + \boldsymbol{\sigma}_l) \\ \boldsymbol{\epsilon}_n &= (\frac{1}{2}(\mathbf{D_x u} + \mathbf{D_x u}^T)) = \boldsymbol{\epsilon}_{np} = \boldsymbol{\epsilon}_l \end{aligned} \tag{I.1}$$

where the subscripts np and l indicate the nucleoplasm and the lamina respectively, $\mathbf{u}$ is the displacement, $\mathbf{D_x u}$ is the usual displacement gradient.

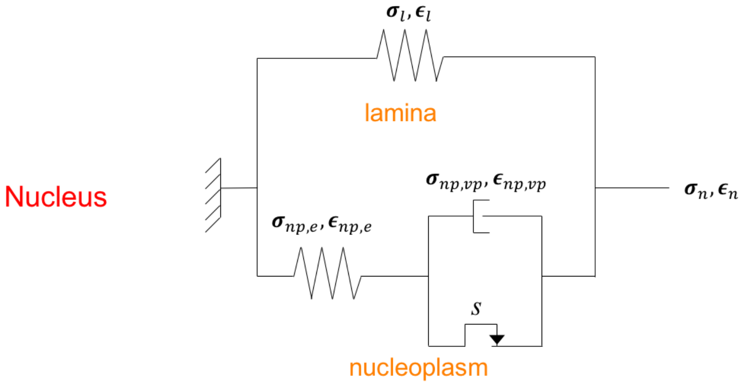

Figure I.5: Rheological model of the homogenized nucleus.

The nucleoplasm itself is decomposed into a visco-plastic part and a purely elastic part as follows

$$\begin{aligned} \boldsymbol{\sigma}_{np} &= \boldsymbol{\sigma}_{np,e} = \boldsymbol{\sigma}_{np,vp} \\ \boldsymbol{\epsilon}_{np} &= \boldsymbol{\epsilon}_{np,vp} + \boldsymbol{\epsilon}_{np,e} \end{aligned} \tag{I.2}$$

where the subscripts vp and e stand for visco-plastic and elastic, respectively.

The constitutive equations of each part reads more specifically:

$$\begin{aligned} \boldsymbol{\sigma}_l &= \lambda_l Tr(\boldsymbol{\epsilon}_n)\mathbf{I} + 2\mu_l \boldsymbol{\epsilon}_n \\ \boldsymbol{\sigma}_{np} &= \lambda_{np} Tr(\boldsymbol{\epsilon}_n - \boldsymbol{\epsilon}_{np,vp})\mathbf{I} + 2\mu_{np}(\boldsymbol{\epsilon}_n - \boldsymbol{\epsilon}_{np,vp}) \\ \dot{\boldsymbol{\epsilon}}^D_{np,vp} &= \frac{h(\boldsymbol{\sigma}_{np,VM} - s)|\boldsymbol{\sigma}_{p,VM} - s|}{\eta_{np}} \frac{\boldsymbol{\sigma}^D_{np}}{\|\boldsymbol{\sigma}^D_{np}\|} \end{aligned} \tag{I.3}$$

where λ_l, μ_l, λ_{np} and μ_{np} are the Lamé coefficients of the lamina and the nucleoplasm, respectively and defined as $\lambda_k = \frac{E_k \nu_n}{(1+\nu_n)(1-2\nu_n)}$ and $\mu_k = \frac{E_k}{2(1+\nu_n)}$, $k = \{l, np\}$. E_l,

E_{np} and ν_n are the Young moduli of the lamina and the nucleoplasm respectively and the Poisson ratio of the nucleus. Tr defines the trace operator, $\mathbf{I}$ is the identity matrix and $\boldsymbol{A}^D$ indicates the deviatoric part of the tensor $\boldsymbol{A}$ defined as $\boldsymbol{A}^D = \boldsymbol{A} - \frac{1}{2}Tr(\boldsymbol{A})\mathbf{I}$. We hypothesize that $\boldsymbol{\epsilon}_{np,vp}$ only has a deviatoric part. We note h the regularized Heaviside function, s the plasticity threshold, $\boldsymbol{\sigma}_{np,VM}$ the Von Mises stress of the nucleoplasm and η_{np} the viscosity of the nucleoplasm defined as $\eta_{np} = \tau_{np}E_{np}$, with τ_{np} its characteristic time [Vaziri et al., 2006].

Due to the very small thickness of the lamina (50 nm), the Young moduli were weighted with regard to the surface occupied by the lamina and the nucleoplasm as:

$$\begin{aligned} E_{np} &= E_{np,0}\frac{A_{np,0}}{A_{n,0}} \\ E_l &= E_{l,0}\frac{A_{l,0}}{A_{n,0}} \end{aligned} \tag{I.4}$$

with $A_{np,0}$, $A_{n,0}$, and $A_{l,0}$ being the initial areas of the nucleoplasm, the nucleus and the lamina, respectively.

The nominal values of the mechanical parameters $E_{l,0}$, $E_{np,0}$, τ_{np} and the Poisson ratio ν_n were taken from the literature and previous works. There is no experimental data allowing us to determine the value of the plasticity threshold s, so we performed various tests in order to find a consistent value. All parameters values and references are listed in Table I.1.

I.2.3 Compression experiment

Initially, the nucleus is placed between two rigid plates (Ω_{plate}) of length l_{plate} and height g_{plate}, the lower plate being fixed and the upper one being mobile, to simulate a compression experiment as the one presented by Caille et al. [2002]. All parameters were chosen so that the compression speed is the same as in the aforementioned paper and the nucleus is compressed up to 70 %. Gravity is applied to the nucleus before the compression cycle begins. The upper l_{up} and lower l_{lp} plates are described by two characteristic functions $g_{up}(\mathbf{x})$ and $g_{lp}(\mathbf{x}-\mathbf{u})$,where $\mathbf{x}-\mathbf{u}$ indicates the initial position of any particle of the system (see Appendix C), in order to give the obstacles position to evaluate the contact force.

The friction force between the plate and the cell when they are in close contact is neglected. A normal force is introduced to control the contact between the nucleus and the plates, as follows

$$\mathbf{f}_{plate}(\mathbf{x}-\mathbf{u}) = \mu_{plate}g_{plate}(\mathbf{x})\mathbf{n}_{plate} \tag{I.5}$$

where μ_{plate} is the penalization coefficient, $\mathbf{u}$ is the displacement and $g_{plate}(\mathbf{x}) =$

$g_{up}(\mathbf{x}) + g_{lp}(\mathbf{x})$ is a characteristic function that varies smoothly between 0 and 1 on a given interpenetration depth equal to 0.2 μm. This depth can be adjusted by varying the scaling parameter of the Heaviside function. Consequently, because of the property of the level set, no such force is applied when the plate and the nucleus are far from each other. When they become close enough, an eventual small overlap induces a large repulsive force cubically dependant of the overlap depth. Lastly, $\mathbf{n}_{plate}$ is the outward normal to the plates.

As described in previous work [Aubry et al., 2014], the global equilibrium of the system is expressed as

$$\rho_n \mathbf{a} = \mathbf{Div}(\boldsymbol{\sigma}_n) + \mathbf{f}_{plate} + \rho_n \mathbf{g} \tag{I.6}$$

where ρ_n is the nucleus density, $\mathbf{a}$ is the acceleration and **Div** is the usual divergence and $\mathbf{g}$ is the gravity acceleration. $\mathbf{f}_{plate}$ is the contact force, considered here as a localized body force in the neighbourhood of the contact with plate.

I.2.4 Results

The nucleus undergoes a loading/unloading cycle as defined in Appendix I.C. First, the nucleus settles down on the fixed lower plate under the action of gravity ($0 < t < T_1$). Then, the mobile upper plate goes down and compresses the nucleus up to 70% ($T_1 < t < T_1 + T_2$) and keeps the maximum compression for a time T_3, with T_1, T_2 and T_3 respectively being equal to 10, 27.5 and 2 s. Lastly, the upper plate goes back to its initial position as it unloads the nucleus.

In a first simulation, we set $E_{l,0}$ to 3000 Pa, $E_{np,0}$ to 25 Pa, τ_{np} to 2 s and the plasticity threshold to 4 Pa. Our model displays a non linear force-normalized deformation (with d_N the normalized vertical deformation of the nucleus) relationship during compression that shows a similar profile than those from Caille et al. [2002] (Figure I.6a). Additionally, a plastic behaviour is observed since the norm of the average deviatoric strain $\boldsymbol{\epsilon}_n^D$ reaches a peak of 70% at t = 30 s as expected, but does not drop back to zero once the nucleus is unloaded (between t = 35 s and t = 50 s). In fact a residual strain of about 8% is found (Figure I.6b).

Four test cases were implemented to study the influence of several parameters on the behaviour of the model. First, we examined the response of the nucleus model for $E_{l,0}$ equal to 100, 500, 1000, 3000 and 10000 Pa (Figure I.7). When the lamina's Young modulus increases, the force needed to compress the nucleus increases as well (Figure I.7a), while the plastic deviatoric strain after unloading decreases (Figure I.7b). To compress the nucleus up to 50 %, the force ranges from 6 $\mu N/m$ for $E_{l,0} = 100$ Pa to 80 $\mu N/m$ for $E_{l,0} = 10000$ Pa, while the plastic deviatoric strain after unloading ranges

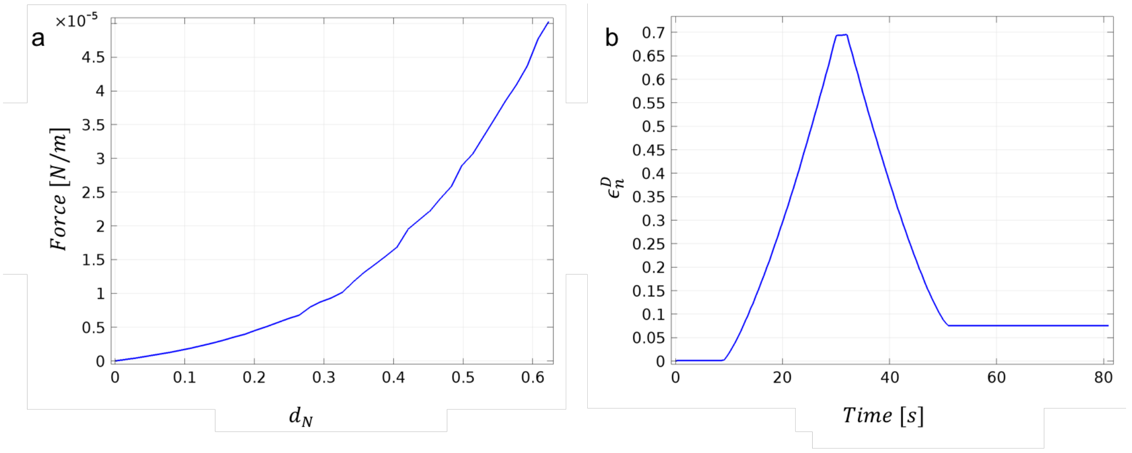

Figure I.6: Simulation of compression and release of the nucleus. (a) Force-Normalized displacement curve, (b) evolution of the deviatoric strain $\boldsymbol{\epsilon}_n^D$ in the nucleus with respect to time

from 30% to 2.5% (Figure I.7a).

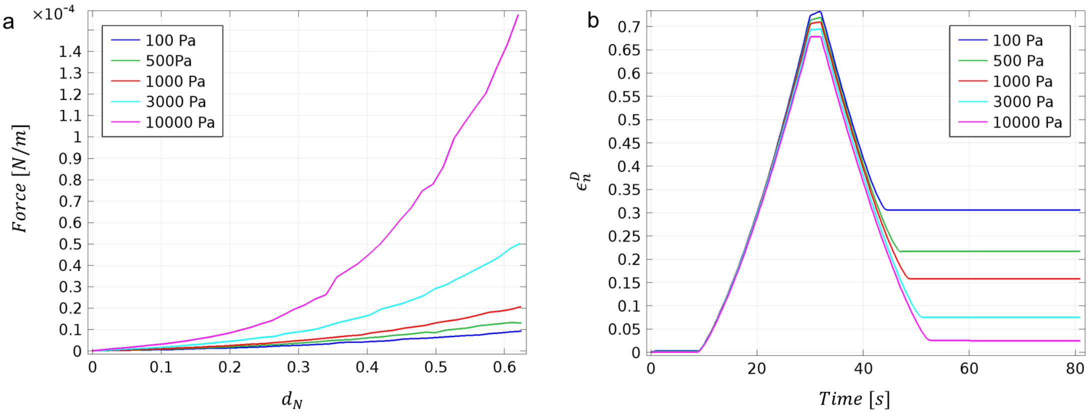

Figure I.7: Parametric study on $E_{lamina,0}$. (a) Force-Normalized displacement curve and (b) evolution of the nuclear deviatoric strain $\boldsymbol{\epsilon}_n^D$ with respect to time

Thus, the lamina seems to be a major load-bearing element of the nucleus and a lower Young modulus, which can be correlated with lamin-deficient nuclei, triggers higher nuclear plasticity. This result is consistent with a recent study on nuclear deformability [Cao et al., 2016] in which irreversible nuclear deformation was observed after transmigration of Lamin A/C deficient cells.

Although most reviews focus on the lamina [Harada et al., 2014; McGregor et al., 2016], the recent work of Stephens et al. [2017] highlighted the fact that chromatin may play a critical role as well. The influence of the stiffness of the nucleoplasm, in which the chromatin has a major impact, was then considered with $E_{np,0}$ equal to 1, 25, 100 and 1000 Pa (Figure I.8). As expected, the force required to compress the nucleus increased with the Young modulus (Figure I.8a). Contrarily to the previous case, a higher nucleoplasm stiffness yielded to an increased plasticity (Figure I.8b). The deviatoric strain upon unloading of the nucleus goes down at various speeds due to the definition of $\eta_{np} = \tau_{np} E_{np}$. Here, the force required for a 50 % compression ranges from 20 to 100 $\mu N/m$ (see Fig. I.8a). Thus, as well as the lamina, our model features the nucleoplasm as a potential load-bearing element.

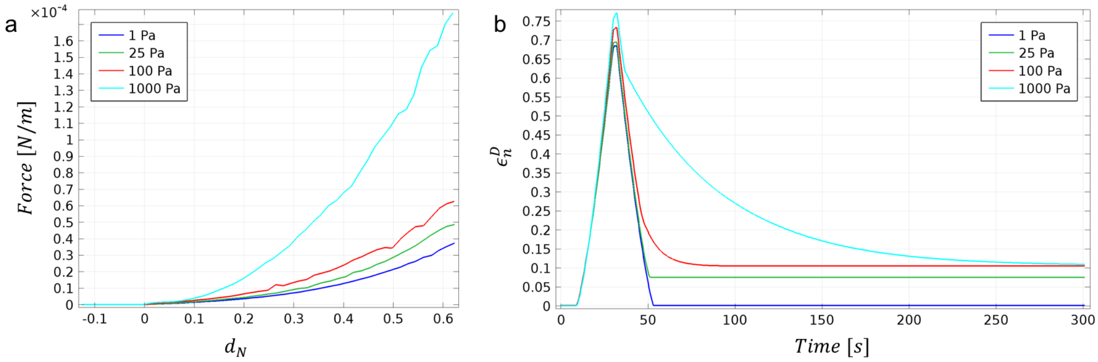

Figure I.8: Parametric study on $E_{nucleoplasm,0}$. (a) Force-Normalized displacement curve and (b) evolution of the nuclear deviatoric strain with respect to time

Finally, τ_{np} and s could also affect the overall mechanical behaviour of the nucleus. The nucleoplasm characteristic time has been found to be very disperse depending on the cell and experiment type. In this simulation, τ_{np} was set to 0.1, 1, 2, 10 and 30 s (Figure I.9b). Longer characteristic times gave less plastic behaviours down to only 2 %. As for the influence of s, with values of 0.1, 1, 2, 4, 10 and 30 Pa (Figure I.9a), the last two values yielded roughly no plastic strain. It is interesting to notice that there is an increased plasticity from 0 to 5 % when the threshold increases from 0.1 to 4 Pa (see Fig. I.9).

Nuclear plasticity correlates with the lamin levels and nucleoplasm stiffness

In conclusion, our model does reproduce the visco-elastic behaviour of the cell's nucleus, as well as its plasticity upon higher strains. Depending on the values of the Young's moduli of the lamina and the nucleoplasm, either of them can be the major load-bearing element of the nucleus. With respect to the experimental works in the literature, we choose to set the lamina as the major load-bearing element and the nucleoplasm as the one prone to plasticity. The aforementioned plasticity grows larger with increasing values of $E_{np,0}$ and with decreasing values of $E_{l,0}$ or τ_{np}. Smaller value of $E_{l,0}$ can be seen as the modeling equivalent of lamin-deficient nuclei, hence being in agreement with experimental results where Lamin A/C-deficient nuclei present a

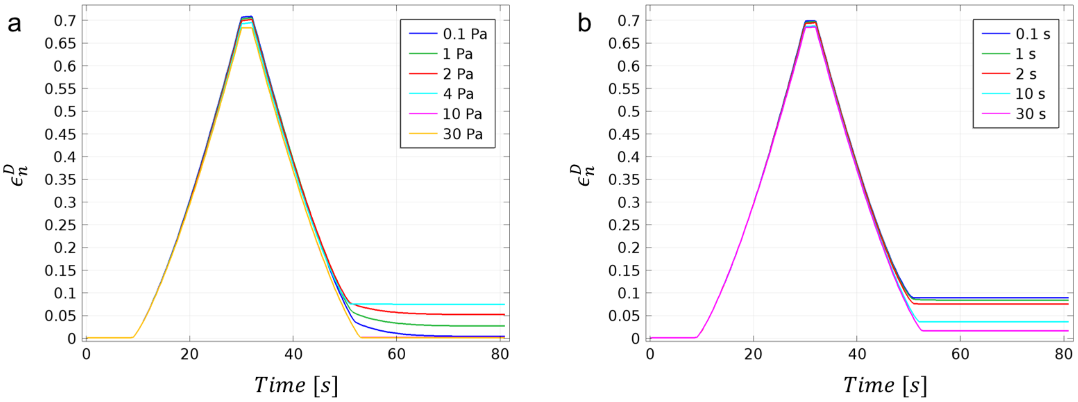

Figure I.9: Deviatoric strain for various values of plasticity threshold (a) and $\tau_{nucleoplasm}$(b)

larger plastic deformation [Cao et al., 2016]. Now that the compression study has been completed, we aim to implement the nucleus constitutive law into a whole cellular model to simulate a perfusion test.

I.3 2D model of a perfusion experiment

In this section we detail the 2D FE model developed to simulate a perfusion test. In this type of experiment, the cell passively flows through micro-channels in which a fluid flow is assured thanks to a pressure gradient [Isermann et al., 2012]. Cell deformability and passing time can be studied. The objective here is to analyze the influence of the nucleus visco-elasto-plastic behaviour during perfusion on the overall cellular response. Such influence will be studied more specifically on two phenotypes through variation of the mechanical properties of the lamina: a control model and a lamin-deficient model of the cell.

I.3.1 Cell geometry

Similarly to our previous works [Aubry et al., 2014; Allena, 2014], the cell (Ω_{cell}) is constituted by the surrounding actin cortex (Ω_{cortex}) and the cytosol ($\Omega_{cytosol}$), which form the cytoplasm ($\Omega_{cytoplasm}$), and by the lamina (Ω_{lamina}, Sec. I.2.2) and the nucleoplasm ($\Omega_{nucleoplasm}$, Sec. I.2.2), which form the nucleus ($\Omega_{nucleus}$, Sec. I.2.2) (Figure I.10). To describe the Ω_{cortex} and the $\Omega_{cytosol}$, we use, as we did for the lamina and the nucleoplasm (Sec. I.2.1) two characteristic functions $g_{cx}(\mathbf{x})$ and $g_{cl}(\mathbf{x})$ as described in the Appendix D (Figure I.10).

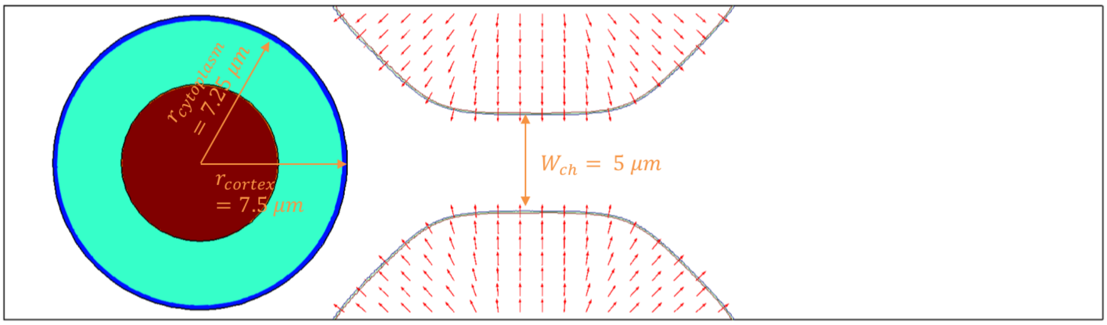

Figure I.10: Cell and micro-channel geometry. In red is the nucleoplasm, orange is the lamina (too thin to be visible here), light blue is the cytosol and dark blue is the cortex. Red arrows represent the outward normal to the channel $\mathbf{n}_{ch}$.

I.3.2 Perfusion experiment

The perfusion device is modeled as a constriction channel ($\Omega_{channel}$) defined by two rigid walls. The upper (g_{uc}) and the lower (g_{lc}) walls (Figure I.10) are defined by two characteristic functions (Appendix E).

We first performe a microfluidic study to obtain the velocity field inside the micro-channel. The fluid is described by the Navier-Stokes equation as follows

$$\rho_f \boldsymbol{a}_f = -\nabla p\mathbf{I} + \eta_f \Delta \boldsymbol{v}_f \tag{I.7}$$

where ρ_f is the volumetric mass of the fluid, $\boldsymbol{a}_f$ the fluid acceleration, ∇ the gradient operator, p the pressure, η_f the fluid viscosity, Δ the Laplacian and $\boldsymbol{v}_f$ the fluid velocity.

The boundary conditions include a pressure P_{in} at the left inlet and P_{out} at the right outlet. The fluid parameters are chosen in order to avoid turbulent patterns both at the entrance and the exit of the constriction (Figure I.11 and Table I.1). Finally, we assume that the velocity field calculated without the cell in the constriction does not vary over the perfusion assay, which constitutes a first step towards a more complex multiphysics model including fluid-structure interactions that will not be developed here.

The force $\mathbf{f}_{fluid}$ exerted by the fluid on the cell cytoplasm is then defined as

$$\mathbf{f}_{fluid}(\mathbf{x}) = f_{fluid,0}\boldsymbol{v}_f \tag{I.8}$$

with $f_{fluid,0}$ the amplitude of the force applied on the cell, chosen so that the cell always passes through the channel in $1s \pm 0.05s$ in order to be able to compare the results (experimentally, the passing time in such devices ranges from 20 ms to a few seconds [Philipp Isermann, 2013; Hou et al., 2009; Luo et al., 2014]).

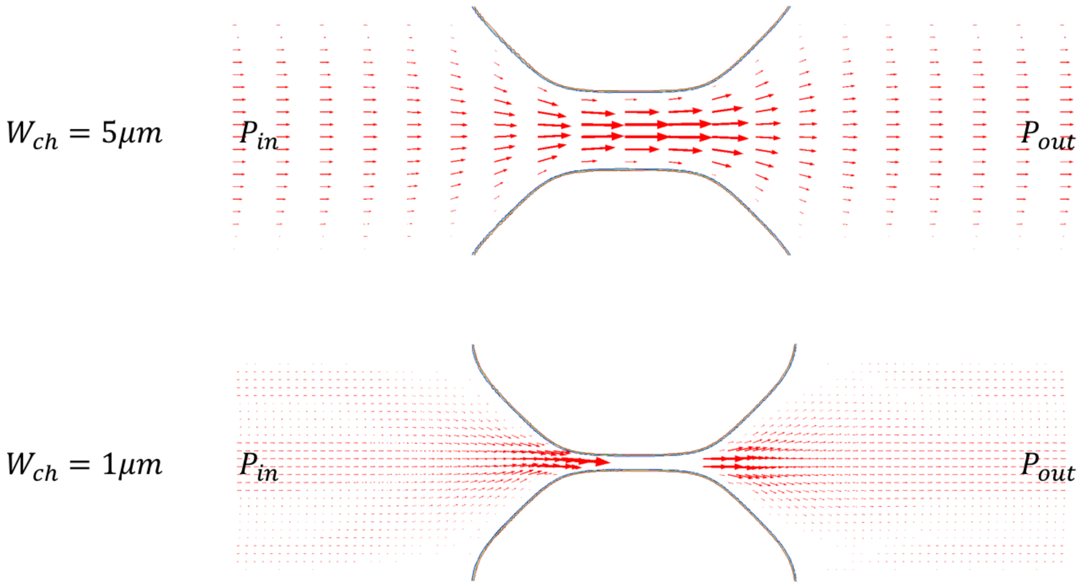

Figure I.11: Profile of the fluid velocity inside the device for two sizes of constriction W_{ch}=5 and 1 μm

Similarly to the compression test, a contact force is applied, now using the regularized characteristic function of the channel, as follows

$$\mathbf{f}_{ch}(\mathbf{x}) = \mu_{ch} g_{ch}(\mathbf{x}) \mathbf{n}_{ch} \tag{I.9}$$

where μ_{ch} is the penalization coefficient, $g_{ch} = g_{uc} + g_{lc}$ is a characteristic function as defined for g_{plate} in Section 2.3 and $\mathbf{n}_{ch}$ is the outward normal to the channel.

I.3.3 Constitutive model and mechanics of the cytoplasm

As the nucleus constitutive law has been presented in Sec. I.2.2, here we describe the mechanical behaviour of the other cell's components, namely the actin cortex and the cytosol. We assume that the cortex behaves as an isotropic elastic material, whereas the cytosol is described as viscoelastic, the whole cytoplasm thus being described by a generalized Maxwell model [Allena, 2014; Allena and Aubry, 2012; Aubry et al., 2014] (Figure I.12). As previously developed, the cytoplasm is considered as a Voigt homogenized material from its two constituents, namely the cortex and the cytosol. The whole cell is then a heterogeneous material composed of the homogenized cytoplasm and the homogenized nucleus, such that $\boldsymbol{\sigma} = g_n \boldsymbol{\sigma}_n + g_{cp} \boldsymbol{\sigma}_{cp}$. The boundary conditions between these components are handled by the level set functions and the finite elements.

The Cauchy stress of the cytoplasm $\boldsymbol{\sigma}_{cp}$ is given by

$$\boldsymbol{\sigma}_{cp} = g_{cp}(\mathbf{x})(\boldsymbol{\sigma}_{cx} + \boldsymbol{\sigma}_{cl}) \tag{I.10}$$

where the subscripts cp, cx and cl represent the cytoplasm, the cortex and the cytosol respectively, and g_{cp} represents the characteristic function of the cytoplasm (see Appendix D).

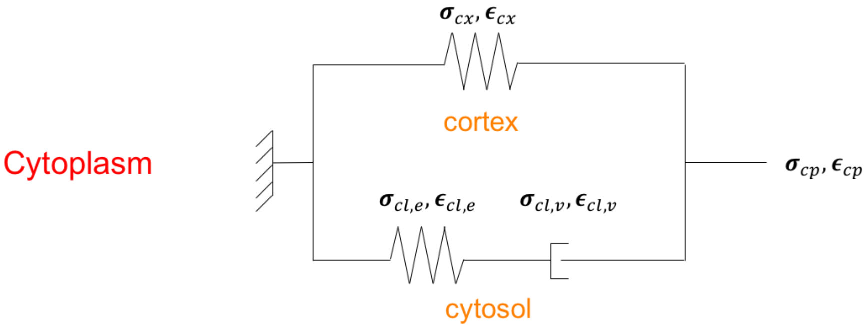

Figure I.12: Rheological model of the cytoplasm [Aubry et al., 2014].

The cytosol itself is decomposed into a viscous part and a purely elastic part as follows

$$\begin{aligned} \boldsymbol{\sigma}_{cl} &= \boldsymbol{\sigma}_{cl,e} = \boldsymbol{\sigma}_{cl,v} \\ \boldsymbol{\epsilon}_{cl} &= \boldsymbol{\epsilon}_{cl,v} + \boldsymbol{\epsilon}_{cl,e} \end{aligned} \tag{I.11}$$

where the subscripts v and e respectively stand for viscous and elastic.

Additionally, we have

$$\begin{aligned} \boldsymbol{\sigma}_{cx} &= \lambda_{cx} Tr(\boldsymbol{\epsilon}_{cp})\mathbf{I} + 2\mu_{cx}\boldsymbol{\epsilon}_{cp} \\ \boldsymbol{\sigma}_{cl} &= \lambda_{cl} Tr(\boldsymbol{\epsilon}_{cp} - \boldsymbol{\epsilon}_{cl,v})\mathbf{I} + 2\mu_{np}(\boldsymbol{\epsilon}_{cp} - \boldsymbol{\epsilon}_{cl,v}) \\ \dot{\boldsymbol{\epsilon}}^{D}_{cl,v} &= \frac{\boldsymbol{\sigma}^{D}_{cl}}{\eta_{cl}} \end{aligned} \tag{I.12}$$

where λ_{cx}, μ_{cx}, λ_{cl} and μ_{cl} are the Lamé coefficients associated to the cortex and the cytosol respectively, defined as $\lambda_k = \frac{E_k \nu_c}{(1+\nu_c)(1-2\nu_c)}$ and $\mu_k = \frac{E_k}{2(1+\nu_c)}$, $k = \{cx, cl\}$. E_{cx}, E_{cl} and ν_c are the Young moduli of the cortex and the cytosol respectively and the Poisson ratio of the cytoplasm. η_{cl} is the viscosity of the cytosol defined as $\eta_{cl} = \tau_{cl} E_{cl}$, with τ_{cl} its characteristic time [Vaziri et al., 2006]. As before, we assume that $\boldsymbol{\epsilon}_{cl,v}$ only has a deviatoric part.

As previously, and due to the very small thickness of the cortex (10 nm), the Young moduli were homogenized with regard to the surface occupied by the cortex and the cytosol as:

$$\begin{aligned} E_{cx} &= E_{cx,0}\frac{A_{cx,0}}{A_{cp,0}} \\ E_{cl} &= E_{cl,0}\frac{A_{cl,0}}{A_{cp,0}} \end{aligned} \tag{I.13}$$

where $A_{cx,0}$, $A_{cp,0}$, and $A_{cl,0}$ are the initial areas taken respectively by the cortex, the cytoplasm and the cytosol.

The nominal values of the mechanical parameters $E_{cx,0}$, $E_{cl,0}$, τ_{cl} and the Poisson ratio ν_{cp} were taken from the literature and previous work as listed in Table I.1.

Similarly to the nucleus computation, an ALE formulation with updated frame and moving mesh is adopted. The contact force is also considered as a body force only applied in the possible overlapped region between the cell and the channel whenever it takes place and measured by the intersection level set of the channel and the cell and the global equilibrium of the system is expressed as

$$\rho\mathbf{a} = \mathbf{Div}(\boldsymbol{\sigma}) + \mathbf{f}_{fluid} + \mathbf{f}_{ch} \tag{I.14}$$

where ρ is the cell density defined as $\rho(\mathbf{x}) = \rho_n g_n(\mathbf{x}) + \rho_{cp} g_{cp}(\mathbf{x})$, $\mathbf{a}$ is the acceleration and $\boldsymbol{\sigma}$ is the Cauchy stress that reads $\boldsymbol{\sigma} = g_n\boldsymbol{\sigma}_n + g_{cp}\boldsymbol{\sigma}_{cp}$. $\mathbf{f}_{fluid}$ and $\mathbf{f}_{ch}$ respectively indicate the fluid force exerted on the cell cytoplasm and the contact force between the cell and the channel.

I.3.4 Results

In this study, we tackle two channel widths: $W_{ch} = 5\mu m$ (slightly sub-nuclear) and $W_{ch} = 1\mu m$ (highly sub-nuclear). The large channel corresponds to a common size for perfusion experiment [Isermann et al., 2012], while the 1-micron channel was chosen to study the behaviour of the cell under higher constriction at a size close to the 10% limit impeding cell migration completely [Wolf et al., 2013]. The fluid force applied to the cell is designed so that the passing time through the constriction is of the order of seconds, as can be found experimentally [Philipp Isermann, 2013; Hou et al., 2009; Luo et al., 2014]. In each case, we are first interested in the displacement of the cell inertia center $\mathbf{d}_c$ that decomposes as $d_{c,x}$ and $d_{c,y}$ on both directions with $d_{c,y}$ equal to 0. Then we study the evolution of the norm of the nucleus deviatoric strain ϵ_n^D, the value and distribution of the Von Mises stress, the ratio of nucleus area over cell area $\frac{A_{nuc}}{A_{cell}}$ and the vertical and horizontal component of the positive part of the resultant of the fluid force acting on the cell ($|F_{fluid,x}|$ and $|F_{fluid,y}|$ respectively), all with respect to $d_{c,x}$. To better understand the structural role of the lamina and the chromatin, we implement one model for a "wild-type" cell and another for a "lamin-deficient" one, in which $E_{l,0}$ is set to 3000 and 30 Pa, respectively.

a 5 microns-wide constriction

We first look at the "wild-type" model in the larger channel. The cell rapidly plugs the channel ($d_{c,x} = 4\mu m$) and then requires more time until the nucleus itself clogs the channel ($d_{c,x} = 12\mu m$). Once this is accomplished, the cell goes through very rapidly (it takes here 1-2 ms, which is consistent with the results presented in [Isermann et al., 2012]) and can then go back to a relaxed state (Figure I.13 and Movie 1 in Supplementary Material).

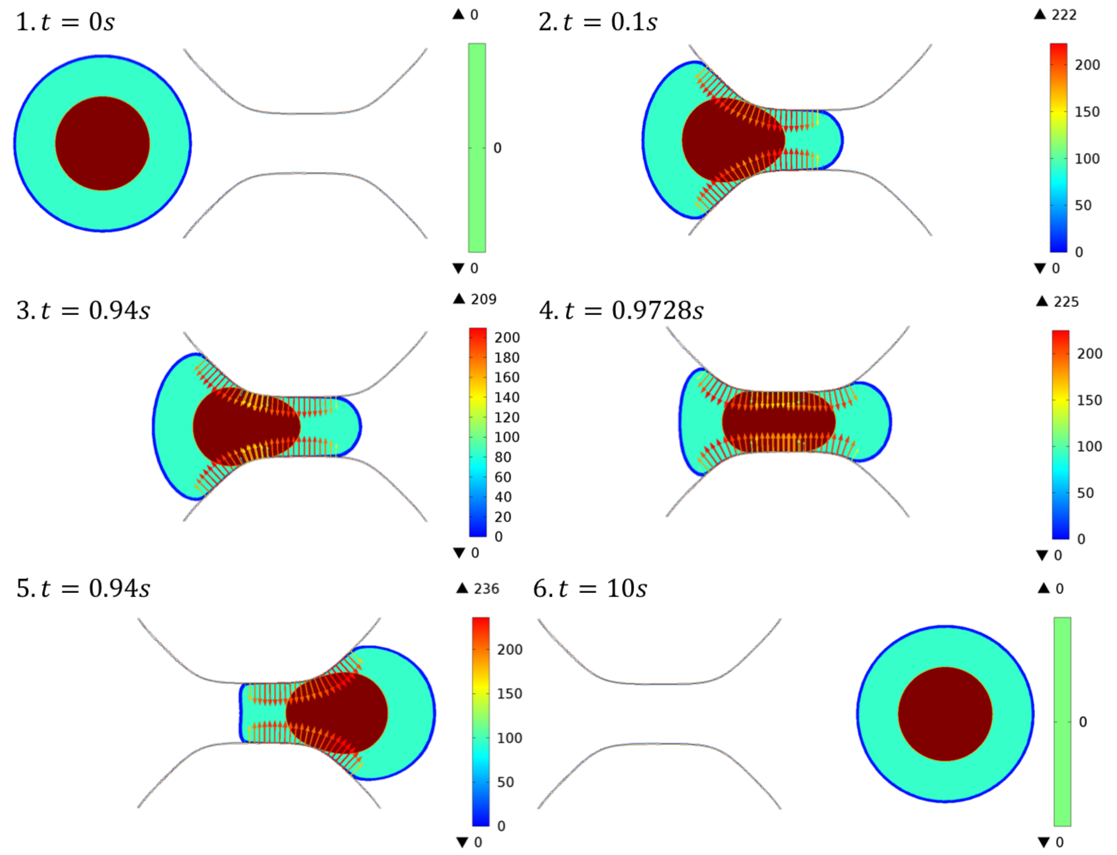

1. $t = 0s$ 2. $t = 0.1s$ 3. $t = 0.94s$ 4. $t = 0.9728s$ 5. $t = 0.94s$ 6. $t = 10s$

Figure I.13: Simulation results of the perfusion test in the 5 μm-wide micro-channel for a wild-type cell. Arrows represent the norm of the contact force (refer to the color scale for the value)

The horizontal displacement of the cell center of inertia $d_{c,x}$ illustrates this phenomenon clearly (Figure I.14.a). The deviatoric strain of the nucleus reaches a maximum of 35% at the center of the constriction and no plastic deformation is found in the nucleus (Figure I.14.b). The Von Mises stress reaches a maximum of 5.39 Pa in the constriction, which is barely above the plasticity threshold, thus explaining the absence of plasticity (Movie 1 in Supplementary Material). Initially, the cell and the nucleus area are equal to 176 μm^2 and 50 μm^2 respectively. The ratio of the nucleus over the cell area then is 28.5 % before entering the constriction. As expected, this ratio grows larger as the cell enters the constriction to reach a peak of 40% for $d_{c,x} = 16\mu m$ and it goes back to its initial value once the cell is completely out of the constriction after a displacement of 30 μm (Figure I.14.c)). The resulting force applied on the fluid reaches 80 and 17 pN in the vertical and horizontal direction respectively (Figure I.14.d). If the absolute value of the force is not specifically relevant by itself, it will be interesting to compare these value with the other test cases.

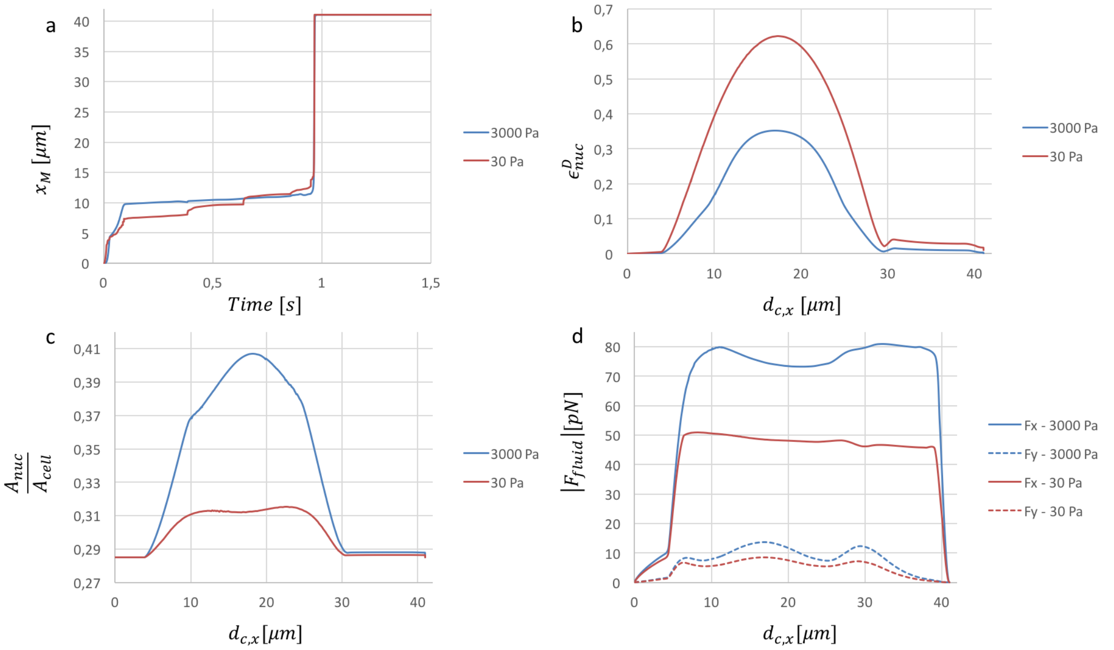

Figure I.14: Comparison of the perfusion test results in the 5 μm-wide micro-channel for the wild-type (blue: $E_{l,0} = 3000 Pa$) and the lamin-deficient (red: $E_{l,0} = 30 Pa$) model. a) Horizontal displacement of the cell inertia center $d_{c,x}$, b) Nucleus deviatoric strain, c) Nucleus area relative to whole cell area and d) Resulting fluid force (vertical and horizontal components)

In the lamin-deficient model, the displacement of the cell's center of inertia follows a similar curve, but the other parameters present significant differences (Figure I.14). ϵ^D_{nuc} goes up to 62%, which means a 77% higher nucleus compression than for the wild-type model. The Von Mises stress reaches a maximum of 7.3 Pa in the constriction, which is slightly higher than before and should yield a higher plasticity not observed here (Movie 2 in Supplementary Material). This seemingly contradictory result will be discussed later in this section. The area ratio curve shows two local maxima of 31 and 31.5 % for $d_{c,x}$ =12 and 24 μm. Both values are around 20% lower than previously, which reinforces the earlier finding that the nucleus undergoes more deformation when the lamina does not "shield" it from stress. As it could be expected, the force required to get the nucleus through the constriction is lower now that the lamina is depleted as it reaches 51 and 9 pN in the vertical and horizontal direction respectively.

b 1 micron-wide constriction

With the strongly sub-nuclear channel and the wild-type model, we could have expected a similar behaviour as previously, only slower. However, the cell undergoes a different path to go through the smaller constriction. Indeed, as previously, the cell rapidly clogs the constriction ($d_{c,x} = 4\mu m$), but then, the nucleus rapidly clogs the constriction ($d_{c,x} = 12\mu m$). Eventually, the nucleus gets gradually squeezed inside the constriction until the cell center of inertia displacement reaches $14\mu m$, where the cell finally goes through at once (Figures I.15 and I.16a. and Movie 3 in Supplementary Material).

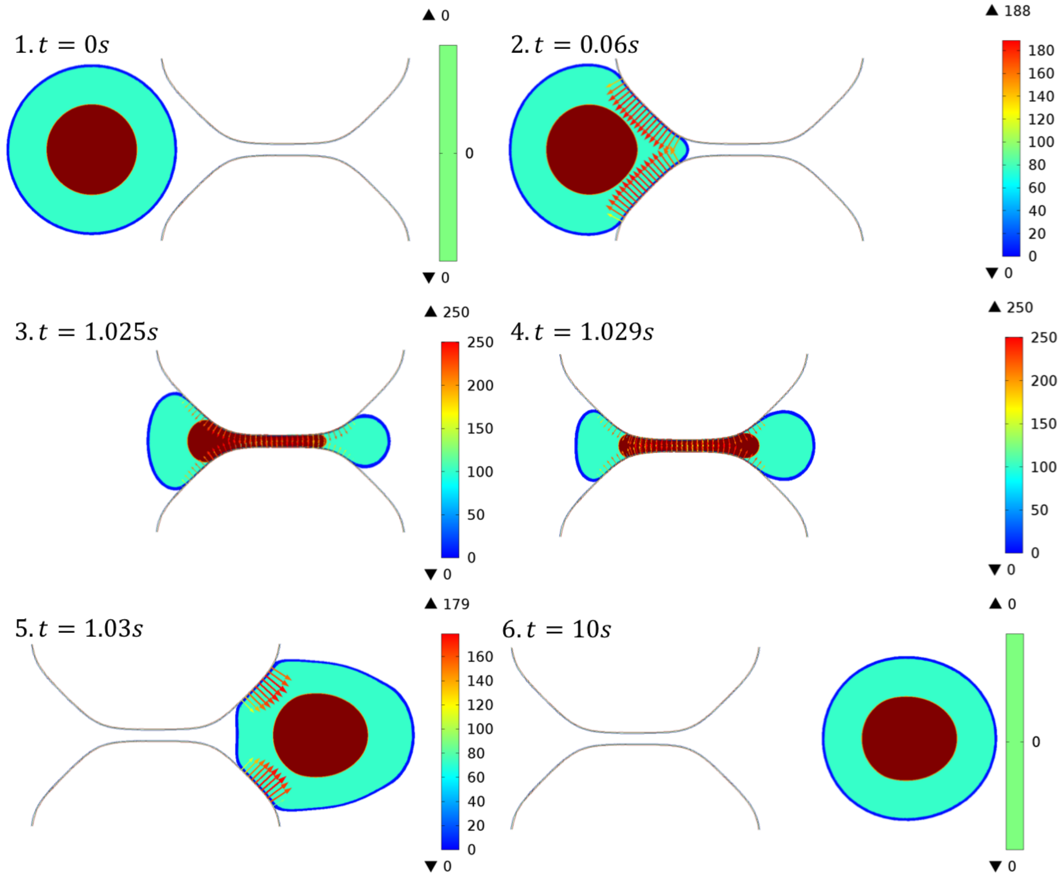

Figure I.15: Simulation results of the perfusion test in the 1 μm-wide micro-channel for a wild-type cell. Arrows represent the norm of the contact force (refer to the color scale for the value)

In this test case, the average nucleus deviatoric strain reaches 88% at $d_{c,x} = 18\mu m$ (Figure I.16b.), which corresponds to the time when the rear of the nucleus is fully inside the constriction. Here, the nucleus presents a plastic strain of 8 % after reaching the other side of the constriction. The Von Mises stress reaches a maximum of 13.7 Pa at the center of the constrained the nucleus as it first clogs the channel and then displays a relaxation (Movie 3 in Supplementary Material). Looking at the ratio of the nucleus area over the cell area, the behaviour is significantly different from the 5 μm-wide channel since two maxima are clearly visible (Figure I.16c.). The ratio reaches a maximum of 38 % at $d_{c,x} = 6.5\mu m$, corresponding to the nucleus starting to plug the channel, the front of the cytosol thus being already squeezed inside the constriction. The ratio then decreases as the nucleus makes its way through the constriction and there is a second peak at 40% for $d_{c,x} = 28\mu m$ as the rear of the nucleus exits the constriction, before it settles down to 28.4% at the end of the perfusion test (Figure I.16c.). The force needed for the cell to go through the constriction reaches 120 and 22 pN in the x and y direction respectively (Figure I.16d.), which is 50% higher, for the vertical component, as in the 5-μm channel.

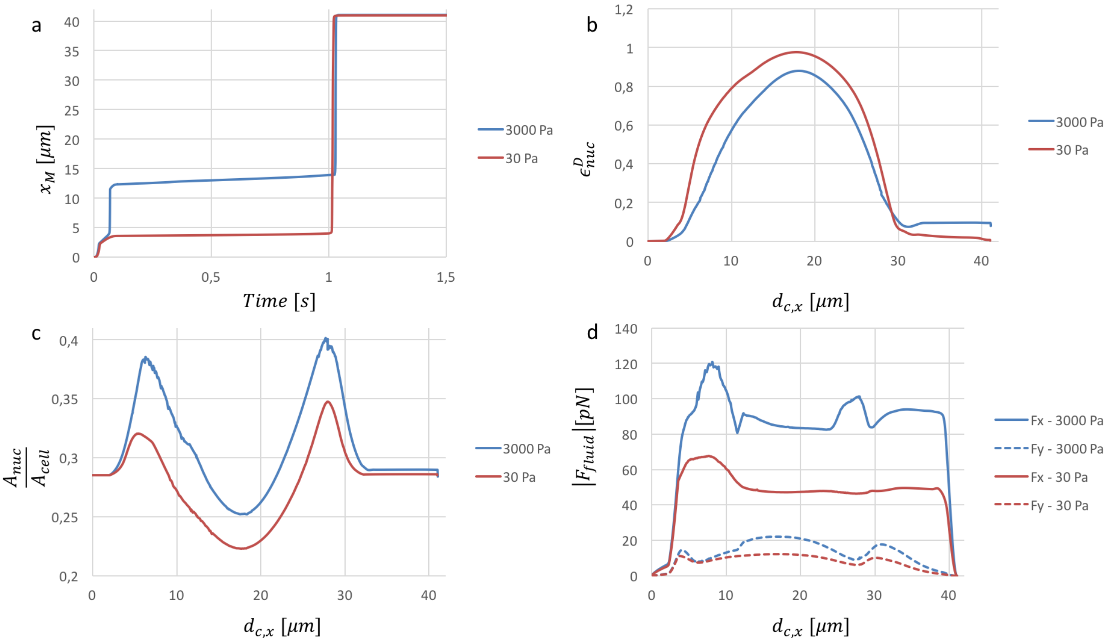

Figure I.16: Comparison of the perfusion test results in the 1 μm-wide micro-channel for wild type and lamin deficient cells. a) Horizontal displacement of the cell inertia center $d_{c,x}$, b) Nucleus deviatoric strain, c) Nucleus area relative to whole cell area and d) Resulting fluid force (vertical and horizontal components)

As for the lamin-deficient model, starting with the displacement of the cell's center of inertia, differences can be spotted from the wild-type case (Figure I.16). The cell first plugs the channel ($d_{c,x} = 3.5\mu m$) and, as soon as the cytoplasm tip starts getting into the constriction ($d_{c,x} = 4\mu m$), the whole cell goes through. Thus, the nucleus itself does not seem to be a barrier to transmigration anymore. The deviatoric strain reaches 98%, which is 10% higher than for the wild-type model. However, there is no plastic strain anymore compared to the wild-type, which is in contradiction with experimental results from Cao et al. [2016]. This result will be further discussed in the following section. The Von Mises stress reaches a maximum of 16.2 Pa at the center of the constrained part of the nucleus as it starts clogging the constriction and then displays a relaxation (Movie 4 in Supplementary Material). Again, this value, superior than in the wild-type cell should result in an increase of the plasticity. The area ratio between the nucleus and the cell follows the same pattern than previously although with lower values: it reaches a first maximum of 32% for $d_{c,x} = 5.5\mu m$ and second one of 35% for $d_{c,x} = 28\mu m$. Together with the values of deviatoric strain, this shows, as in the larger channel, that the nucleus gets more squeezed if no lamina protects it. The force of the fluid on the cell reaches 67 and 12 pN for its vertical and horizontal component respectively, which is almost half the force needed for the wild-type cell, once again comforting us in the idea that the nucleus is a major barrier during transmigration through small constrictions, and the lamina seems to be a crucial structural constituent of the nucleus allowing it to resist to large deformation. The decrease of plastic strain in the lamin-deficient model however raises the question of the role of the nucleoplasm as a load-bearing element of the nucleus.

The cytoplasm can "pull" on a too soft nucleus

The complete cell model with a visco-elasto-plastic nucleus was tested in 5 μm-wide and a 1 μm-wide perfusion channel both as a wild-type cell ($E_{l,0} = 3000$ Pa) and a lamin-deficient one in which the lamina was considered a hundred times weaker ($E_{l,0} = 30$ Pa). In both cases, the cell first plugs the device and then goes through very rapidly once it has progressed far enough in the constriction with a passage time of the order of 1 ms. In the larger channel, once the nucleus is in contact with both the upper and lower channels, it is sufficiently compressed for the cell to go through directly. However, in the smaller constriction, an additional step is necessary for the nucleus to fully plug the channel and only once the cell center of inertia has progressed far enough in the constriction, the whole cell can pass through.

The study of the lamin-deficient model gives very interesting results and insights of the importance of the interaction between the cytoplasm and the nucleus. First, the lamin-deficient nucleus undergoes significantly higher deformation than the wild-type one, hence showing the importance of the lamina as a load-bearing component of the nucleus. This seems to back up studies stating that the lamina is the major structural constituent in the nucleus. However, a closer look on the behaviour of the nucleus with regards to plasticity shows that the wild-type model displays a 10% plastic strain after exiting the smaller constriction, while the lamin-deficient one does not display any irreversible deformation (a similar but less intense phenomenon is observed in the larger constriction regarding the Von Mises stress). This property of our model appears in contrast with the latest experimental results as discussed by Cao et al. [2016].

Further analysis of our results revealed that the cell cytoplasm seems responsible for this loss of plasticity as it forces the lamin-deficient soft nucleus to return to its original shape. This is an exciting result that meets the experimental observations of Keeling et al. [2017]. It also backs the recent thesis defended by Stephens et al. [2017] that not only does the lamina play a role but chromatin also plays a major part as a load-bearing element in the nucleus.

I.4 Conclusion and Discussion

All in all, our model of an isolated nucleus does display a plastic behaviour under extensive compression, as shown experimentally [Pajerowski et al., 2007], and shows that both the lamina and the nucleoplasm have an impact on the mechanical behaviour of the overall nucleus. A softer lamina and a stiffer nucleoplasm yield a higher irreversible deformation after unloading the nucleus. Implementing this model in a whole cell model under a perfusion test allowed us to unveil the mechanical influence of the cytoplasm on the nucleus. In the 1 μm constriction, the plastic deformation significantly decreased with the depletion of the lamina, which we explain by the cytoplasm "pulling" on the now softer nucleus to get it back to its original shape. This is further confirmed by the fact that in the isolated nucleus model, a decreased lamina Young modulus resulted in an increased plasticity. Thus, in order to observe plastic deformation, either the nucleoplasm should be stiffer, or the cytoplasm softer. This mechanical interplay between nuclear stiffness and its plasticity reveals the ability of numerical simulation to tackle biological issues and to shed light on different mechanisms.

Our model however presents some limitations and some improvements can be included. First of all, a 2D FE model was used, whereas a three-dimensional (3D) one would be needed in order to faithfully reproduce 3D experiments. This point is particularly sensitive looking at the compression test: a more valid reduction would be an axi-symmetric model. We still chose to develop a purely 2D model since it fits the perfusion test: the compression test model is a step towards a more complete cell model and a 2D reduction will not give faithful quantitative results, but the qualitative trends stay valid.

Moreover, we chose to cope with the thinness of the cortex and the lamina through weighted Young's moduli with respect to the relative area of each cell component. Nevertheless, a shell model would surely fit better and could provide new insights on the relation between the various cell components [Aubry et al., 2016].

Lately, some very interesting models of the cell nucleus were developed [Giverso et al., 2014; Cao et al., 2016] in which the interaction between the nucleus and the cytoplasm is represented by an active force puling on the nucleus. Our model gives a new insight on the passive interaction between these 2 cellular compartments: the comparison between the isolated nucleus model and the complete cell model proves the major mechanical influence the cytoplasm can have on the nucleus in a passive state. This interaction would be increasingly important during an active phenomenon like transmigration and our results thus open new investigation focuses.

Parameter	**Description**	**Value (unit)**	**References**
r_{cell}	Cell radius	7.5 μm	
r_{cortex}	Cortex radius	7.5 μm	
$r_{cytosol}$	Cytosol radius	7.25 μm	
r_{lamina}	Lamina radius	4 μm	
$r_{nucleoplasm}$	Nucleoplasm radius	3.95 μm	
t_{cortex}	Cortex thickness	250 nm	[Aubry et al., 2014]
t_{lamina}	Lamina thickness	50 nm	[Bridger et al., 2007; Kaminski et al., 2014]
$E_{cx,0}$	Nominal cortex Young modulus	100 Pa	[Aubry et al., 2014; Allena, 2014]
$E_{cl,0}$	Nominal cytosol Young modulus	10 Pa	[Kamgoue et al., 2007; Ayala et al., 2016; Aubry et al., 2014; Allena, 2014]
$E_{l,0}$	Nominal lamina Young modulus	3000 Pa	[Aubry et al., 2014; Allena, 2014]
$E_{np,0}$	Nominal nucleoplasm Young modulus	25 Pa	[Vaziri et al., 2006; Vaziri and Mofrad, 2007; Aubry et al., 2014; Allena, 2014]
E_{cx}	Equivalent cortex Young modulus	9.08 Pa	
E_{cl}	Equivalent cytosol Young modulus	9.16 Pa	
E_{l}	Equivalent lamina Young modulus	74.53 Pa	
E_{np}	Equivalent nucleoplasm Young modulus	24.38 Pa	
ν_c	Cytoplasm Poisson ratio	0.3	[Aubry et al., 2014]
ν_n	Nucleus Poisson ratio	0.4	[Aubry et al., 2014]
τ_{cl}	Cytosol characteristic time	1 s	[Milner et al., 2012; Guilak et al., 2000]
τ_{np}	Nucleoplasm characteristic time	2 s	[de Vries et al., 2007; Celedon et al., 2011; Vaziri and Mofrad, 2007; Guilak et al., 2000]

s	Nucleoplasm plasticity threshold	4 Pa	
ρ_{cp}	Cytoplasm density	1000 kg/m^3	[Milo and Phillips, 2015]
ρ_n	Nucleus density	1400 kg/m^3	[Milo and Phillips, 2015]
$A_{cp,0}$	Initial cytoplasm area	126 μm^2	
$A_{cx,0}$	Initial cortex area	11 μm^2	
$A_{cl,0}$	Initial cytosol area	115 μm^2	
$A_{n,0}$	Initial nucleus area	50 μm^2	
$A_{np,0}$	Initial cytoplasm area	49 μm^2	
$A_{l,0}$	Initial cortex area	1 μm^2	
T_1	First characteristic time for $y_p(t)$	10 s	
T_2	Second characteristic time for $y_p(t)$	27.5 s	
T_3	Third characteristic time for $y_p(t)$	2 s	
v_0	Velocity of the compression plate	0.25 $\mu m/s$	[Caille et al., 2002]
$x_{p,0}$	x-coordinate of the plates	0	
$y_{up,0}$	y-coordinate of the upper plate	6 μm	
$y_{lp,0}$	y-coordinate of the lower plate	6 μm	
l_{plate}	length of the plates	30 μm	
h_{plate}	vertical width of the plates	1 μm	
x_0	Geometric parameter of the perfusion constriction	15 μm	
a_1	Geometric parameter of the perfusion constriction	11 μm	
a_2	Geometric parameter of the perfusion constriction	16 μm	
d_0	width of the constriction	$W_{ch,1} = 1\mu m$ or $W_{ch,5} = 5\mu m$	
P_{in}	Inlet pressure in perfusion device	1 Pa	
P_{out}	Outlet in perfusion device	0	
ρ_f	Fluid density in perfusion device	1000 kg/m^3	
η_f	Fluid viscosity in perfusion device	10^{-2} Pa.s	

Table I.1: Set of parameters describing the visco-elasto-plastic model

Supplementary Material

We compiled movies of the results of the perfusion assay for each cell type and channel width and plotted the Von Mises stress inside the nucleus in order to understand better the plasticity process. For each movie, the frame is set at 60 images per second. In the 5-μm channel models, the time step between each frame is 0.01 s from 0 to 1.2 s and 0.1 s from 1.2 to 10s (Movies 1 and 2). In the 1-μm channel wild-type model, the time step between each frame is 0.01 s from 0 to 1.028 s, 0.001 s from 1.028 s to 1.03 s, 0.01 s from 1.03 to 1.2 s and 0.1 s from 1.016 to 10s. In the 1-μm channel lamin-deficient model, the time step between each frame is 0.01 s from 0 to 1.014 s, 0.001 s from 1.014 s to 1.016 s, 0.01 s from 1.016 to 1.2 s and 0.1 s from 1.016 to 10s.

Movie 1 - Wild type cell perfusing across the 5-μm channel (Color scale corresponds to the Von Mises stress).

Movie 2 - Lamin-deficient cell perfusing across the 5-μm channel (Color scale corresponds to the Von Mises stress).

Movie 3 - Wild type cell perfusing across the 1-μm channel (Color scale corresponds to the Von Mises stress).

Movie 4 - Lamin-deficient cell perfusing across the 1-μm channel (Color scale corresponds to the Von Mises stress).

Appendices

I.A Characteristic functions

Throughout the paper, each cellular component is geometrically defined through a characteristic function g, which is a composition of a Heaviside function h and a spatial level set l as follows

$$g_i(\mathbf{x}) = h \circ l_i(\mathbf{x}) = \begin{cases} 1 & \text{for } l_i(\mathbf{x}) > 0 \\ 0 & \text{for } l_i(\mathbf{x}) < 0 \end{cases} \tag{I.15}$$

where i = np, l, cl, cx. The nucleoplasm and the lamina constitute the nucleus ($g_n = g_{np} + g_l$), while the cytosol and the cortex constitute the cytoplasm ($g_c = g_{cl} + g_{cx}$).

I.B Nucleus geometry

$$g_l(\mathbf{x}) = \begin{cases} 1 & \text{if } r_{nucleoplasm} < \|\mathbf{x} - \mathbf{c}_{nucleus}\| < r_{lamina} \\ 0 & \text{otherwise} \end{cases} \tag{I.16}$$

$$g_{np}(\mathbf{x}) = \begin{cases} 1 & \text{if } \|\mathbf{x} - \mathbf{c}_{nucleus}\| < r_{nucleoplasm} \\ 0 & \text{otherwise} \end{cases} \tag{I.17}$$

where $\mathbf{c}_{nucleus}$ is the position of the center of the nucleus, $r_{nucleoplasm}$ and r_{lamina} are the nucleoplasm and lamina radii, respectively and $\mathbf{x}$ is the actual spatial position.

I.C Compression experiment

The compression plate are defined by the following Heaviside functions

$$g_{up}(\mathbf{x} - \mathbf{u}) = \begin{cases} 1 & \text{if } l_{up} > 0 \\ 0 & \text{otherwise} \end{cases} \tag{I.18}$$

$$g_{lp}(\mathbf{x} - \mathbf{u}) = \begin{cases} 1 & \text{if } l_{lp} > 0 \\ 0 & \text{otherwise} \end{cases} \tag{I.19}$$

such that $g_{plate} = g_{up} + g_{lp}$, with l_{up} and l_{lp} two level set functions expressed as

$$\begin{aligned} l_{up} &= -(\frac{x - x_{p,0}}{l_{plate}})^8 - (\frac{y - y_{up,0} - y_p(t)}{g_{plate}})^4 - 1 \\ l_{lp} &= -(\frac{x - x_{p,0}}{l_{plate}})^8 - (\frac{y + y_{lp,0}}{g_{plate}})^4 - 1 \end{aligned} \tag{I.20}$$

where $(x_{p,0}, y_{lp,0})$ and $(x_{p,0}, y_{up,0})$ are coordinates of the two plates, respectively and $y_p(t)$ is the vertical displacement applied on l_{up}, the lower plate being fixed, and defined as:

$$y_p(t) = \begin{cases} -v_0(t - T_1) & \text{if } T_1 \leq t \leq T_1 + T_2 \\ -v_0 T_2 & \text{if } T_1 + T_2 \leq t \leq T_1 + T_2 + T_3 \\ -v_0(-t + T_1 + 2T_2 + T_3) & \text{if } T_1 + T_2 + T_3 \leq t \leq T_1 + 2T_2 + T_3 \end{cases} \tag{I.21}$$

with v_0 the compression velocity and T_1, T_2 and T_3 the time parameters defining the loading/unloading of the plate (see Fig. I.C.1).

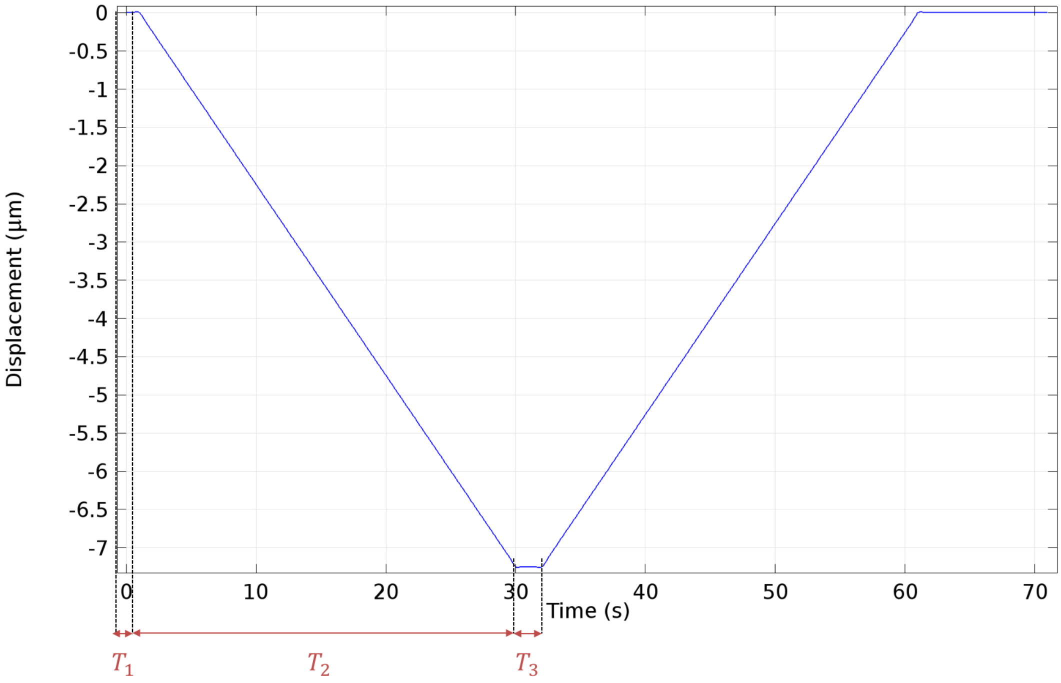

Figure I.C.1: Displacement of the mobile upper plate.

I.D Cell geometry

$$g_{cx}(\mathbf{x}) = \begin{cases} 1 & \text{if } r_{cytosol} < \|\mathbf{x} - \mathbf{c}_{nucleus}\| < r_{cortex} \\ 0 & \text{otherwise} \end{cases} \tag{I.22}$$

$$g_{cl}(\mathbf{x}) = \begin{cases} 1 & \text{if } \|\mathbf{x} - \mathbf{c}_{nucleus}\| < r_{cytosol} \\ 0 & \text{otherwise} \end{cases} \tag{I.23}$$

with $r_{cytosol}$ and r_{cortex} being the cytosol and cortex radii, respectively.

I.E Perfusion experiment

I.E.1 Geometry

$$g_{uc}(\mathbf{x}-\mathbf{u}) = \begin{cases} 1 & \text{if } l_{uc} < 0 \\ 0 & \text{otherwise} \end{cases} \tag{I.24}$$

$$g_{lc}(\mathbf{x}-\mathbf{u}) = \begin{cases} 1 & \text{if } l_{lc} < 0 \\ 0 & \text{otherwise} \end{cases} \tag{I.25}$$

such the $g_{ch} = g_{uc} + g_{lc}$, where l_{uc} and l_{lc} are two level set functions defined as

$$\begin{aligned} l_{uc} &= (\frac{x-x_0}{a_1})^{16} + (\frac{y-y_0}{a_1})^{16} + (\frac{x-x_0-y+y_0}{a_2})^{16} + (\frac{x-x_0+y-y_0}{a_2})^{17} \\ l_{lc} &= (\frac{x-x_0}{a_1})^{16} + (\frac{y+y_0}{a_1})^{16} + (\frac{x-x_0-y-y_0}{a_2})^{16} + (\frac{x-x_0+y+y_0}{a_2})^{17} \end{aligned} \tag{I.26}$$

where x_0, a_1 and a_2 are geometric parameters and $y_0 = a_1 + d_0/2$, d_0 being the width of the constriction.

I.E.2 Parametric study

The perfusion model involves 41 parameters (see Table I.1), but not all are of the same importance. We can classify them in three categories:

1. The parameters that purely define the system geometry and its dynamics (r_{cell}, r_{cortex}, $r_{cytosol}$, r_{lamina}, $r_{nucleoplasm}$, t_{cortex}, t_{lamina}, $A_{cp,0}$, $A_{cl,0}$, $A_{cx,0}$, $A_{n,0}$,$A_{np,0}$, $A_{l,0}$ T_1, T_2, T_3, v_0, $x_{p,0}$, $y_{up,0}$, $y_{lp,0}$, l_{plate}, h_{plate}, x_0, a_1, a_2, d_0, P_{in}, P_{out}, ρ_f, η_f)

2. The parameters that have been well defined in the literature (ν_c, ν_n, ρ_{cp}, ρ_n)

3. The parameters that present a high variability ($E_{cx,0}$, $E_{cl,0}$, $E_{l,0}$, $E_{np,0}$, τ_{cl}, τ_{np}, s)

We assume that the parameters of the 1^{st} and 2^{nd} categories do not influence the overall results of our work. Among the last category, we chose to focus on those that may play a critical role during the perfusion assay. Considering our interest in the interaction between cytosol and lamina, we chose to perform a parametric study on $E_{cl,0}$, $E_{l,0}$ and τ_{cl}. The plasticity threshold was not included since it was calibrated on the compression test and the value was then kept constant. The sensibility study was conducted on both the wild-type cell model and the lamin-deficient one. For each parameter, 3 simulations were performed using the initial value of the parameter and ±10%.

We analyzed the nuclear deviatoric strain $\boldsymbol{\epsilon}_n^D$ as function of the horizontal displacement of the cell center of inertia $d_{c,x}$ and that said displacement as a function of time in order to assess the influence of cell mechanical parameters on the passage time.

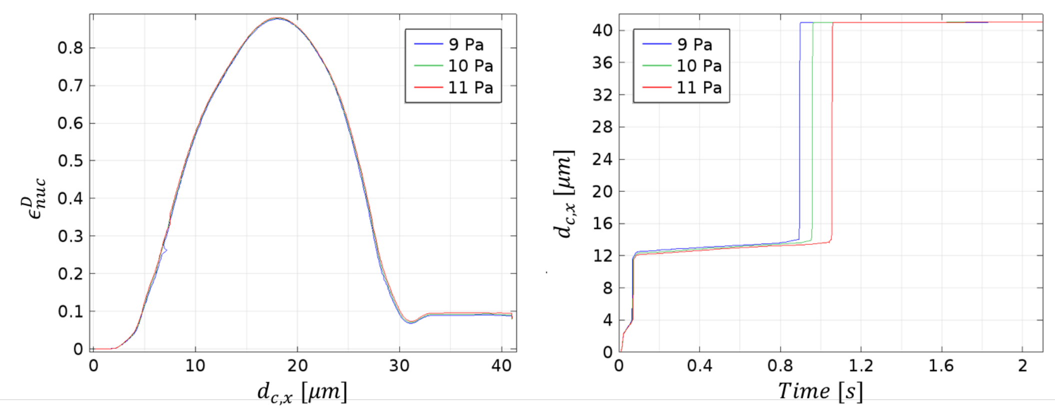

Figure I.E.1: Parametric study on $E_{cl,0}$. Left: Evolution of the nuclear deviatoric strain $\boldsymbol{\epsilon}_n^D$ as function of the horizontal displacement of the cell center of inertia $d_{c,x}$ and Right: Horizontal displacement of the cell center of inertia as a function of time during the 1 μm-wide micro-channel perfusion simulation for the wild-type model.

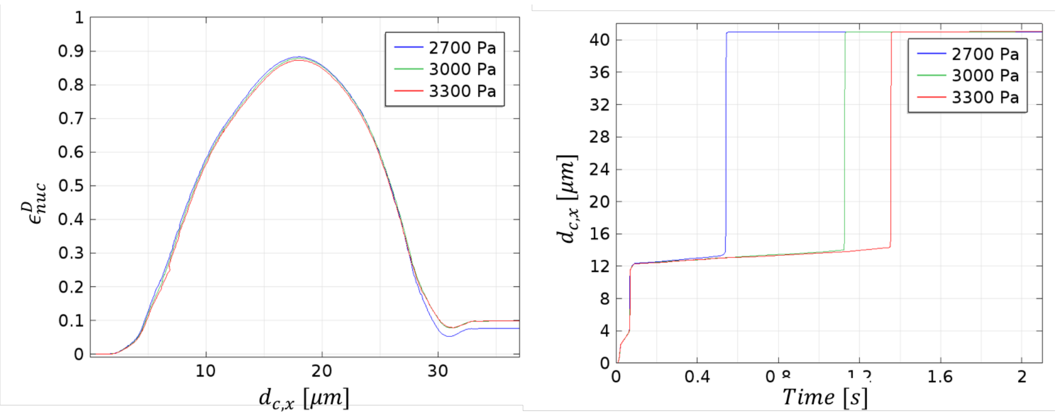

Figure I.E.2: Parametric study on $E_{l,0}$. Left: Evolution of the nuclear deviatoric strain $\boldsymbol{\epsilon}_n^D$ as function of the horizontal displacement of the cell center of inertia $d_{c,x}$ and Right: Horizontal displacement of the cell center of inertia as a function of time during the 1 μm-wide micro-channel perfusion simulation for the wild-type model.

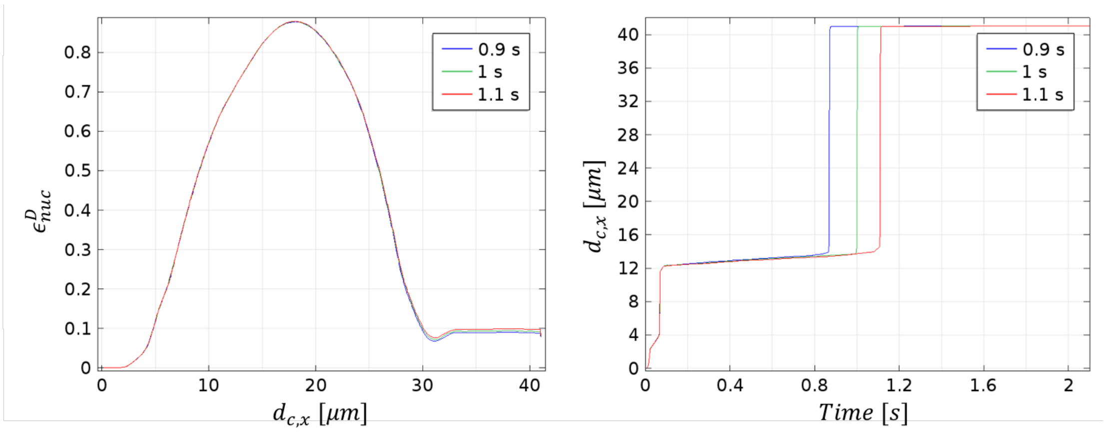

Figure I.E.3: Parametric study on τ_{cl}. Left: Evolution of the nuclear deviatoric strain $\boldsymbol{\epsilon}^D_n$ as function of the horizontal displacement of the cell center of inertia $d_{c,x}$ and Right: Horizontal displacement of the cell center of inertia as a function of time during the 1 μm-wide micro-channel perfusion simulation for the wild-type model.

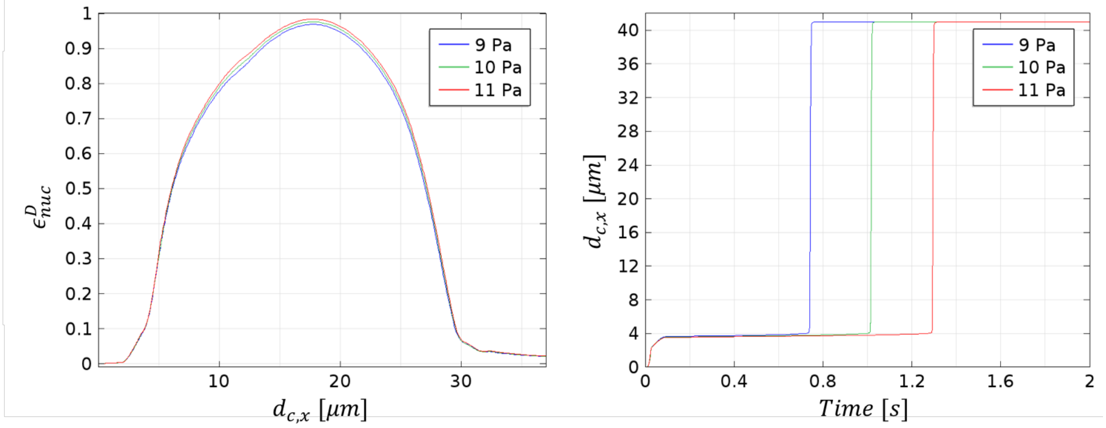

Figure I.E.4: Parametric study on $E_{cl,0}$. Left: Evolution of the nuclear deviatoric strain $\boldsymbol{\epsilon}^D_n$ as function of the horizontal displacement of the cell center of inertia $d_{c,x}$ and Right: Horizontal displacement of the cell center of inertia as a function of time during the 1 μm-wide micro-channel perfusion simulation for the lamin-deficient model.

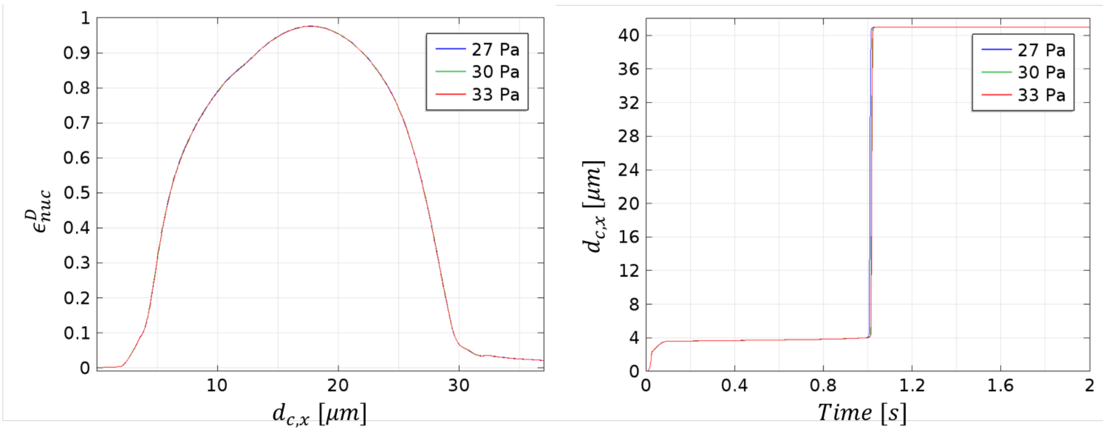

Figure I.E.5: Parametric study on $E_{l,0}$. Left: Evolution of the nuclear deviatoric strain $\boldsymbol{\epsilon}_n^D$ as function of the horizontal displacement of the cell center of inertia $d_{c,x}$ and Right: Horizontal displacement of the cell center of inertia as a function of time during the 1 μm-wide micro-channel perfusion simulation for the lamin-deficient model.

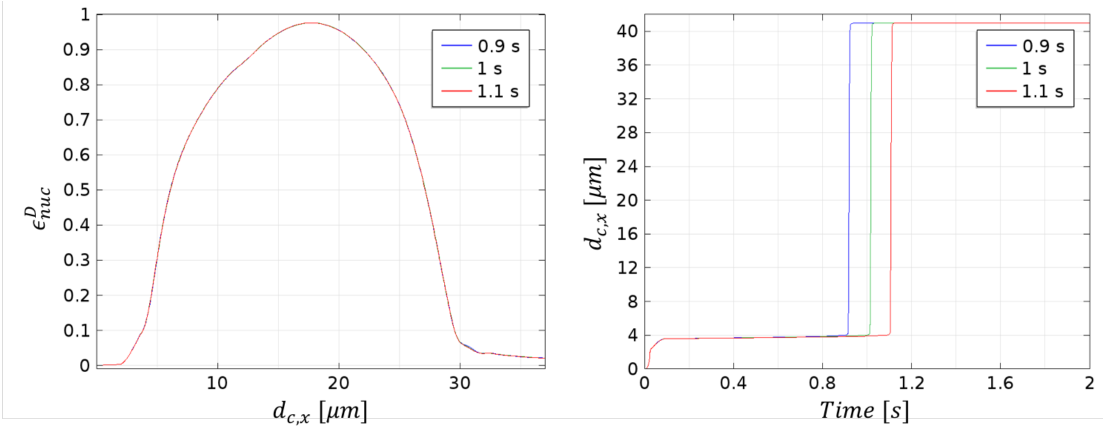

Figure I.E.6: Parametric study on τ_{cl}. Left: Evolution of the nuclear deviatoric strain $\boldsymbol{\epsilon}_n^D$ as function of the horizontal displacement of the cell center of inertia $d_{c,x}$ and Right: Horizontal displacement of the cell center of inertia as a function of time during the 1 μm-wide micro-channel perfusion simulation for the lamin-deficient model.

Bibliography

Allena, R. (2014). Mechanical modelling of confined cell migration across constricted-curved micro-channels. *Molecular & cellular biomechanics: MCB*, 11(3):185–208. 30, 32, 42

Allena, R. and Aubry, D. (2012). 'Run-and-tumble' or 'look-and-run'? A mechanical model to explore the behavior of a migrating amoeboid cell. *Journal of Theoretical Biology*, 306:15–31. 32

Aubry, D., Deveraux, S., and Allena, R. (2016). Cell nucleus membrane modeling through shell tangential differential calculus. In *Oral presentation at the 7th European Congress on Computational Methods in Applied Sciences and Engineering*. 40

Aubry, D., Thiam, H., Piel, M., and Allena, R. (2014). A computational mechanics approach to assess the link between cell morphology and forces during confined migration. *Biomechanics and Modeling in Mechanobiology*, 14(1):143–157. 22, 23, 27, 30, 32, 33, 42, 153

Ayala, Y. A., Pontes, B., Ether, D. S., Pires, L. B., Araujo, G. R., Frases, S., Romao, L. F., Farina, M., Moura-Neto, V., Viana, N. B., and Nussenzveig, H. M. (2016). Rheological properties of cells measured by optical tweezers. *BMC Biophysics*, 9:5. 42

Banigan, E. J., Stephens, A. D., and Marko, J. F. (2017). Mechanics and Buckling of Biopolymeric Shells and Cell Nuclei. *Biophysical Journal*, 113(8):1654–1663. 22

Bell, E. S. and Lammerding, J. (2016). Causes and consequences of nuclear envelope alterations in tumour progression. *European Journal of Cell Biology*, 95(11):449–464. 18

Belytschko, T., Liu, W. K., and Moran, B. (2000). *Nonlinear finite elements for continua and structures*. Wiley. 25

Bridger, J. M., Foeger, N., Kill, I. R., and Herrmann, H. (2007). The nuclear lamina. *FEBS Journal*, 274(6):1354–1361. 42

Bustamante, C., Bryant, Z., and Smith, S. B. (2003). Ten years of tension: single-molecule DNA mechanics. *Nature*, 421(6921):423–427. 19

Caille, N., Thoumine, O., Tardy, Y., and Meister, J.-J. (2002). Contribution of the nucleus to the mechanical properties of endothelial cells. *Journal of Biomechanics*, 35(2):177–187. 20, 21, 22, 23, 26, 27, 43

Cao, X., Moeendarbary, E., Isermann, P., Davidson, P. M., Wang, X., Chen, M. B., Burkart, A. K., Lammerding, J., Kamm, R. D., and Shenoy, V. B. (2016). A Chemomechanical Model for Nuclear Morphology and Stresses during Cell Transendothelial Migration. *Biophysical Journal*, 111(7):1541–1552. 22, 28, 30, 39, 40

Celedon, A., Hale, C. M., and Wirtz, D. (2011). Magnetic Manipulation of Nanorods in the Nucleus of Living Cells. *Biophysical Journal*, 101(8):1880–1886. 42

Christensen, R. M. (1979). *Mechanics of composite materials*. Wiley, New York. 25

Dahl, K. N., Engler, A. J., Pajerowski, J. D., and Discher, D. E. (2005). Power-law rheology of isolated nuclei with deformation mapping of nuclear substructures. *Biophysical Journal*, 89(4):2855–2864. 21, 22

Dahl, K. N. and Kalinowski, A. (2011). Nucleoskeleton mechanics at a glance. *J Cell Sci*, 124(5):675–678. 19

Davidson, P. and Lammerding, J. (2013). Broken nuclei - lamins, nuclear mechanics, and disease. *Trends in cell biology*. 18

de Vries, A. H. B., Krenn, B. E., van Driel, R., Subramaniam, V., and Kanger, J. S. (2007). Direct Observation of Nanomechanical Properties of Chromatin in Living Cells. *Nano Letters*, 7(5):1424–1427. 21, 42

Deguchi, S., Maeda, K., Ohashi, T., and Sato, M. (2005). Flow-induced hardening of endothelial nucleus as an intracellular stress-bearing organelle. *Journal of Biomechanics*, 38(9):1751–1759. 22

Denais, C. M., Gilbert, R. M., Isermann, P., McGregor, A. L., Lindert, M. t., Weigelin, B., Davidson, P. M., Friedl, P., Wolf, K., and Lammerding, J. (2016). Nuclear envelope rupture and repair during cancer cell migration. *Science*, page aad7297. 18

Deveraux, S., Allena, R., and Aubry, D. (2017). A numerical model suggests the interplay between nuclear plasticity and stiffness during a perfusion assay. *Journal of Theoretical Biology*, 435:62–77. 23

Dialynas, G., Shrestha, O. K., Ponce, J. M., Zwerger, M., Thiemann, D. A., Young, G. H., Moore, S. A., Yu, L., Lammerding, J., and Wallrath, L. L. (2015). Myopathic Lamin Mutations Cause Reductive Stress and Activate the Nrf2/Keap-1 Pathway. *PLOS Genet*, 11(5):e1005231. 18

Donea, J., Huerta, A., Ponthot, J.-P., and Rodriguez-Ferran, A. (2004). Arbitrary Lagrangian-Eulerian Methods. In *Encyclopedia of Computational Mechanics*. John Wiley & Sons, Ltd. 25

Erdel, F., Baum, M., and Rippe, K. (2015). The viscoelastic properties of chromatin and the nucleoplasm revealed by scale-dependent protein mobility. *Journal of Physics: Condensed Matter*, 27(6):064115. 21

Ermis, M., Akkaynak, D., Chen, P., Demirci, U., and Hasirci, V. (2016). A high throughput approach for analysis of cell nuclear deformability at single cell level. *Scientific Reports*, 6(1). 20

Friedl, P., Wolf, K., and Lammerding, J. (2011). Nuclear mechanics during cell migration. *Current Opinion in Cell Biology*, 23(1):55–64. 18

Giverso, C., Grillo, A., and Preziosi, L. (2014). Influence of nucleus deformability on cell entry into cylindrical structures. *Biomechanics and Modeling in Mechanobiology*, 13(3):481–502. 22, 40

Gruenbaum, Y., Goldman, R. D., Meyuhas, R., Mills, E., Margalit, A., Fridkin, A., Dayani, Y., Prokocimer, M., and Enosh, A. (2003). The Nuclear Lamina and Its Functions in the Nucleus. *International Review of Cytology*, 226:1–62. 21

Guilak, F., Tedrow, J. R., and Burgkart, R. (2000). Viscoelastic properties of the cell nucleus. *Biochemical and Biophysical Research Communications*, 269(3):781–786. 20, 21, 42

Guillou, L., Babataheri, A., Puech, P.-H., Barakat, A. I., and Husson, J. (2016). Dynamic monitoring of cell mechanical properties using profile microindentation. *Scientific Reports*, 6(1). 20

Guilluy, C., Osborne, L. D., Van Landeghem, L., Sharek, L., Superfine, R., Garcia-Mata, R., and Burridge, K. (2014). Isolated nuclei adapt to force and reveal a mechanotransduction pathway within the nucleus. *Nature cell biology*, 16(4):376–381. 18

Harada, T., Swift, J., Irianto, J., Shin, J.-W., Spinler, K. R., Athirasala, A., Diegmiller, R., Dingal, P. D. P., Ivanovska, I. L., and Discher, D. E. (2014). Nuclear lamin stiffness is a barrier to 3d migration, but softness can limit survival. *The Journal of Cell Biology*, 204(5):669–682. 28

Ho, C. Y., Jaalouk, D. E., and Lammerding, J. (2013). Novel insights into the disease etiology of laminopathies. *Rare Diseases*, 1(1):e27002. 18

Ho, C. Y. and Lammerding, J. (2012). Lamins at a glance. *J Cell Sci*, 125(9):2087–2093. 18

Hou, H. W., Li, Q. S., Lee, G. Y. H., Kumar, A. P., Ong, C. N., and Lim, C. T. (2009). Deformability study of breast cancer cells using microfluidics. *Biomedical Microdevices*, 11(3):557–564. 21, 31, 34

Isermann, P., Davidson, P. M., Sliz, J. D., and Lammerding, J. (2012). Assays to measure nuclear mechanics in interphase cells. *Current protocols in cell biology / editorial board, Juan S. Bonifacino ... [et al.]*, CHAPTER:Unit22.16. 20, 21, 23, 30, 34, 35

Jung, H.-J., Lee, J. M., Yang, S. H., Young, S. G., and Fong, L. G. (2013). Nuclear Lamins in the Brain - New Insights into Function and Regulation. *Molecular Neurobiology*, 47(1):290–301. 19

Kamgoue, A., Ohayon, J., and Tracqui, P. (2007). Estimation of Cell Young's Modulus of Adherent Cells Probed by Optical and Magnetic Tweezers: Influence of Cell Thickness and Bead Immersion. *Journal of Biomechanical Engineering*, 129(4):523. 42

Kaminski, A., Fedorchak, G. R., and Lammerding, J. (2014). The cellular mastermind - mechanotransduction and the nucleus. *Progress in molecular biology and translational science*, 126:157–203. 42

Keeling, M. C., Flores, L. R., Dodhy, A. H., Murray, E. R., and Gavara, N. (2017). Actomyosin and vimentin cytoskeletal networks regulate nuclear shape, mechanics and chromatin organization. *Scientific Reports*, 7(1):5219. 40

Lammerding, J. (2011). Mechanics of the Nucleus. In *Comprehensive Physiology*. John Wiley & Sons, Inc. 21

Leong, F. Y., Li, Q., Lim, C. T., and Chiam, K.-H. (2011). Modeling cell entry into a microchannel. *Biomechanics and Modeling in Mechanobiology*, 10(5):755–766. 23

Lim, C. T., Zhou, E. H., and Quek, S. T. (2006). Mechanical models for living cells–a review. *Journal of Biomechanics*, 39(2):195–216. 20

Liu, H., Wen, J., Xiao, Y., Liu, J., Hopyan, S., Radisic, M., Simmons, C. A., and Sun, Y. (2014). In Situ Mechanical Characterization of the Cell Nucleus by Atomic Force Microscopy. *ACS Nano*, 8(4):3821–3828. 21

Lombardi, M. L., Zwerger, M., and Lammerding, J. (2011). Biophysical Assays to Probe the Mechanical Properties of the Interphase Cell Nucleus: Substrate Strain Application and Microneedle Manipulation. *Journal of Visualized Experiments : JoVE*, (55). 20

Luo, Y., Chen, D., Zhao, Y., Wei, C., Zhao, X., Yue, W., Long, R., Wang, J., and Chen, J. (2014). A constriction channel based microfluidic system enabling continuous characterization of cellular instantaneous Young's modulus. *Sensors and Actuators B: Chemical*, 202:1183–1189. 21, 31, 34

Marko, J. F. and Siggia, E. D. (1995). Stretching DNA. *Macromolecules*, 28(26):8759–8770. 19

Mattana, S., Mattarelli, M., Urbanelli, L., Sagini, K., Emiliani, C., Serra, M. D., Fioretto, D., and Caponi, S. (2018). Non-contact mechanical and chemical analysis of single living cells by microspectroscopic techniques. *Light: Science & Applications*, 7(2):17139. 20

McGregor, A. L., Hsia, C.-R., and Lammerding, J. (2016). Squish and squeeze the nucleus as a physical barrier during migration in confined environments. *Current Opinion in Cell Biology*, 40:32–40. 19, 28, 153

Milner, J. S., Grol, M. W., Beaucage, K. L., Dixon, S. J., and Holdsworth, D. W. (2012). Finite-Element Modeling of Viscoelastic Cells During High-Frequency Cyclic Strain. *Journal of Functional Biomaterials*, 3(1):209–224. 42

Milo, R. and Phillips, R. (2015). *Cell Biology by the Numbers*. Garland Science. 43

Mitchell, M., Denais, C., Chan, M., Wang, Z., Lammerding, J., and King, M. (2015). Lamin A/C Deficiency Reduces Circulating Tumor Cell Resistance to Fluid Shear Stress. *American Journal of Physiology - Cell Physiology*, page ajpcell.00050.2015. 18

Monticelli, M., Conca, D. V., Albisetti, E., Torti, A., Sharma, P. P., Kidiyoor, G., Barozzi, S., Parazzoli, D., Ciarletta, P., Lupi, M., Petti, D., and Bertacco, R. (2016). Magnetic domain wall tweezers: a new tool for mechanobiology studies on individual target cells. *Lab Chip*, 16(15):2882–2890. 20

Naetar, N., Ferraioli, S., and Foisner, R. (2017). Lamins in the nuclear interior – life outside the lamina. *Journal of Cell Science*, 130(13):2087–2096. 19

Nava, M. M., Raimondi, M. T., and Pietrabissa, R. (2014). Bio-chemo-mechanical models for nuclear deformation in adherent eukaryotic cells. *Biomechanics and Modeling in Mechanobiology*, 13(5):929–943. 20, 22

Pajerowski, J. D., Dahl, K. N., Zhong, F. L., Sammak, P. J., and Discher, D. E. (2007). Physical plasticity of the nucleus in stem cell differentiation. *Proceedings of the National Academy of Sciences of the United States of America*, 104(40):15619–15624. 22, 40

Philipp Isermann, J. L. (2013). Nuclear mechanics and mechanotransduction in health and disease. *Current biology : CB*, 23(24):R1113–21. 31, 34

Rowat, A., Foster, L., Nielsen, M., Weiss, M., and Ipsen, J. (2005). Characterization of the elastic properties of the nuclear envelope. *Journal of the Royal Society Interface*, 2(2):63–69. 21

Rowat, A. C., Lammerding, J., and Ipsen, J. H. (2006). Mechanical Properties of the Cell Nucleus and the Effect of Emerin Deficiency. *Biophysical Journal*, 91(12):4649–4664. 19

Schwartz, C., Fischer, M., Mamchaoui, K., Bigot, A., Lok, T., Verdier, C., Duperray, A., Michel, R., Holt, I., Voit, T., Quijano-Roy, S., Bonne, G., and Coirault, C. (2017). Lamins and nesprin-1 mediate inside-out mechanical coupling in muscle cell precursors through FHOD1. *Scientific Reports*, 7(1):1253. 18

Schäpe, J., Prausse, S., Radmacher, M., and Stick, R. (2009). Influence of Lamin A on the Mechanical Properties of Amphibian Oocyte Nuclei Measured by Atomic Force Microscopy. *Biophysical Journal*, 96(10):4319–4325. 18

Skau, C. T., Fischer, R. S., Gurel, P., Thiam, H. R., Tubbs, A., Baird, M. A., Davidson, M. W., Piel, M., Alushin, G. M., Nussenzweig, A., Steeg, P. S., and Waterman, C. M. (2016). FMN2 Makes Perinuclear Actin to Protect Nuclei during Confined Migration and Promote Metastasis. *Cell*, 167(6):1571–1585.e18. 18

Smith, S. B., Finzi, L., and Bustamante, C. (1992). Direct mechanical measurements of the elasticity of single DNA molecules by using magnetic beads. *Science*, 258(5085):1122–1126. 19

Stephens, A. D., Banigan, E. J., Adam, S. A., Goldman, R. D., and Marko, J. F. (2017). Chromatin and lamin A determine two different mechanical response regimes of the cell nucleus. *Molecular Biology of the Cell*, pages mbc.E16–09–0653. 22, 28, 40

Swift, J. and Discher, D. E. (2014). The nuclear lamina is mechano-responsive to ECM elasticity in mature tissue. *Journal of Cell Science*, page jcs.149203. 21

Swift, J., Ivanovska, I. L., Buxboim, A., Harada, T., Dingal, P. C. D. P., Pinter, J., Pajerowski, J. D., Spinler, K. R., Shin, J.-W., Tewari, M., Rehfeldt, F., Speicher, D. W., and Discher, D. E. (2013). Nuclear Lamin-A Scales with Tissue Stiffness and Enhances Matrix-Directed Differentiation. *Science*, 341(6149):1240104. 21

Tomankova, K., Kolar, P., Malohlava, J., and Kolarova, H. (2012). Mechanical characterisation of HeLa cells using atomic force microscopy. *Current Microscopy Contributions to Advances in Science and Technology. Badajoz: Formatex Research Center*, pages 549–554. 21

Ujihara, Y., Nakamura, M., and Wada, S. (2011). *A Mechanical Cell Model and Its Application to Cellular Biomechanics*. INTECH Open Access Publisher. 22

Vaziri, A., Gopinath, A., and Deshpande, V. S. (2007). Continuum-based computational models for cell and nuclear mechanics. *Journal of the Mechanics of Materials and Structures*, 2(doi:):1169–1192. 22

Vaziri, A., Lee, H., and Mofrad, M. K. (2006). Deformation of the cell nucleus under indentation: Mechanics and mechanisms. *Journal of Materials Research*, 21(08):2126–2135. 22, 26, 33, 42

Vaziri, A. and Mofrad, M. R. K. (2007). Mechanics and deformation of the nucleus in micropipette aspiration experiment. *Journal of Biomechanics*, 40(9):2053–2062. 22, 42

Wolf, K. and Friedl, P. (2006). Molecular mechanisms of cancer cell invasion and plasticity. *The British Journal of Dermatology*, 154 Suppl 1:11–15. 18

Wolf, K., Lindert, M. t., Krause, M., Alexander, S., Riet, J. t., Willis, A. L., Hoffman, R. M., Figdor, C. G., Weiss, S. J., and Friedl, P. (2013). Physical limits of cell migration: Control by ECM space and nuclear deformation and tuning by proteolysis and traction force. *The Journal of Cell Biology*, 201(7):1069–1084. 18, 34

Zwerger, M., Ho, C. Y., and Lammerding, J. (2011). Nuclear Mechanics in Disease. *Annual Review of Biomedical Engineering*, 13(1):397–428. 18

Zwerger, M., Jaalouk, D. E., Lombardi, M. L., Isermann, P., Mauermann, M., Dialynas, G., Herrmann, H., Wallrath, L. L., and Lammerding, J. (2013). Myopathic lamin mutations impair nuclear stability in cells and tissue and disrupt nucleo-cytoskeletal coupling. *Human Molecular Genetics*, page ddt079. 18

Zwerger, M., Roschitzki-Voser, H., Zbinden, R., Denais, C., Herrmann, H., Lammerding, J., Grütter, M. G., and Medalia, O. (2015). Altering lamina assembly identifies lamina-dependent and -independent functions for A-type lamins. *J Cell Sci*, page jcs.171843. 18

Chapter II

The mechanical foundation of cell chimneying

Contents

II.1 Introduction

After studying the mechanical behaviour of the nucleus in compression and perfusion, both being passive mechanisms, we want to focus on the active mechanism behind cell migration. Different modes of motility exist, such as flagellar motility [Silflow and Lefebvre, 2001], gliding [Kappe et al., 2004], swarming [Henrichsen, 1972], mesenchymal [Chhabra and Higgs, 2007; Van Haastert, 2011] or amoeboid motility [Charras and Paluch, 2008]. Some cells are able to switch from mesenchymal (slow F-actin driven pseudopods) to amoeboid (fast myosin-driven blebs) migration as a reaction to environmental cues, such as an increased confinement [Ibo et al., 2016]. Adhesion-based motility rests on a tight synchronization between the protrusion-contraction movement of the cell and the adhesion forces exerted by the cell on the substrate and necessary to anchor and move forward. In 3D confined environments and in the absence of adhesion/traction forces, some cells, such as cancer cells, are able to adopt an amoeboid mode of invasion forming bleb-like constriction rings (i.e. membrane protrusions without cytoskeletal elements such as actin filaments) [Wolf et al., 2003; Liu et al., 2015] and bypassing the requirement for Extra Cellular Matrix (ECM) degradation [Sahai and Marshall, 2003; Friedl, 2004] as occurs during mesenchymal migration. In this specific case, the cell migrates through a traction-independent mechanism named "chimneying" because of its resemblance with a technique used by alpinists to climb up rock clefts [Paluch and Raz, 2013] (see Fig. II.1).

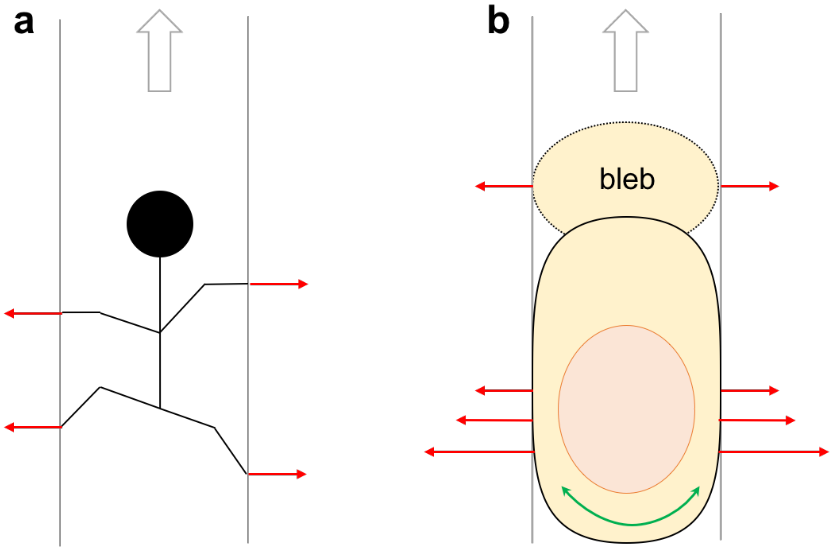

Figure II.1: Illustration of the chimneying mechanism as a rock climbing method (a) and as a bleb-based migration mode (b). The red arrows indicate the pushing force at the root of such mechanism. The green arrow indicates an active contraction of the cell rear that leads to the formation of a frontal bleb.

In fact, the cell generates pushing forces perpendicular to its membrane [Malawista et al., 2000; Lämmermann et al., 2008] and the resulting friction is sufficient to ensure the forward movement. When migrating through the gaps and pores within the ECM, the friction is enhanced by the numerous surrounding fibers on which the cell can push. This chapter then aims at shedding light on this intricate and subtle migration mode

II.1.1 The importance of interstitial fluid flow in cells

The specificity of bleb-based chimneying migration lies in the ability of the cell to move without the formation of adhesions between the cell and its surrounding and in the absence of actin polymerization. Without two key features of classical mesenchymal migration, one may wonder: what is the motor of such migration mechanism ? Some migration modes have been found to be driven by intra-cellular pressure instabilities [Petrie et al., 2014], or fluid exchanges between the cell and its environment [Stroka et al., 2014], thus pointing out the importance to take intra-cellular fluid flow into account when dealing with cell mechanics [Mogilner and Manhart, 2018]. In fact, the pressure instabilities and the resulting interstitial fluid flow are what drives the formation of a bleb [Maugis et al., 2010]. In the absence of actin polymerization, these pressure instabilities can arise from passive deformation of the cell or the active local contractility of the acto-myosin network.

II.1.2 Contractility of the acto-myosin network

The cytoskeleton is the backbone of the cell. Its main components are the microtubules, the intermediate filaments and the actin filaments. The last ones, associated with a motor protein called myosin, regulate cell motility. Indeed, the polymerization of actin fibers at the cell's membrane propels protrusions like pseudopods forward, while the contractility of the actomyosin stress fibers put the cell under tension and can retract or contract cell areas. Let us now take a closer look at those contractile fibers. Coupled with myosin II thick filaments, the thin actin filaments form this large bundle of 10 to 300 filaments [Cramer et al., 1997] (see Fig. II.2). In order to generate a sliding of the actin filaments, the myosin II motor proteins follow a cyclic process called the "powerstroke cycle" [Vale and Milligan, 2000]. Through binding and hydrolysis of ATP (Adenosine triphosphate, the energy carrier of the cell), myosin undergoes conformational changes that induces a translation of the actin filament attached to it.

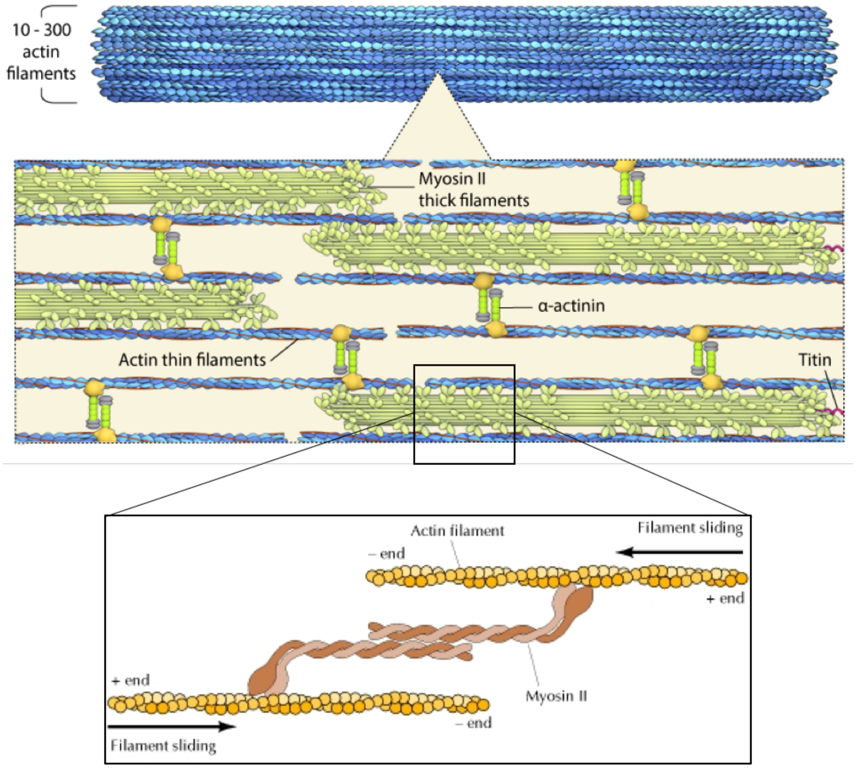

Figure II.2: Illustration of the basic structure of a contractile fiber (which consists of myosin containing contractile “thick” filaments and actin “thin” filaments) and myosin’s powerstroke enabling the sliding of actin fibers Modified from MBInfo and Cooper [2000]

II.1.3 Bleb-based chimneying migration

Bleb-based migration takes its source in the poroelastic properties of the cytoplasm [Zhou et al., 2013; Arroyo and Trepat, 2017] and the contractility of the uropod (the cell’s rear) [Lorentzen et al., 2011]. The life cycle of a bleb can fall into three steps: initiation, growth and retraction [Charras and Paluch, 2008] (see Fig. II.3).

An increase in the intra-cellular hydrostatic pressure, coupled with a local weakening of the actin cortex underlying the membrane, can lead to the initiation and the growth of a bleb, while the repairing of the actin cortex forces the bleb to retract. Chimneying is much less studied and described in the literature than adhesion-based migration. Hence, many hypotheses are made but not yet confirmed on the translocation process. In this type of migration strategy, some experimental works have shown a sharp decrease, or a complete lack, of integrin-mediated adhesions [Lämmermann et al., 2008]. If the cell does not adhere to the substrate, it should oscillate around a stable position, unless another force enables it to move forward. One strong hypothesis is that the cell "pushes" against the confining surface, which generates sufficient friction

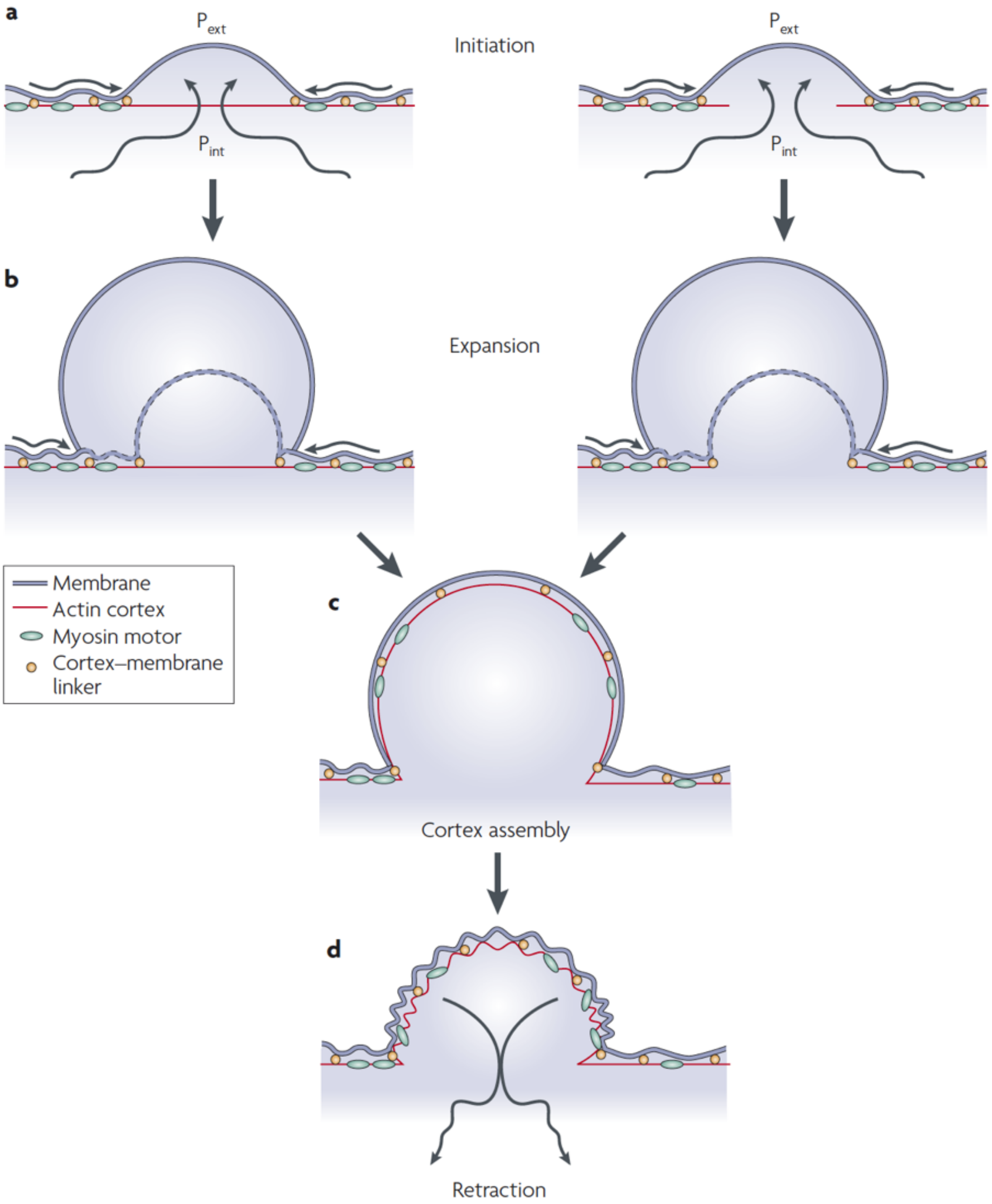

Figure II.3: The life cycle of a bleb can fall into three phases: bleb nucleation, expansion and retraction. a) Bleb initiation can result from a local detachment of the cortex from the membrane (left model) or from a local rupture of the cortex (right model). b) Hydrostatic pressure in the cytoplasm (P_{int}) then drives membrane expansion by propelling cytoplasmic fluid through the remaining cortex (left model) or through the cortex hole (right model). c) As bleb expansion slows down, a new actin cortex reforms under the bleb membrane. d) Recruitment of myosin to the new cortex is followed by bleb retraction. (P_{ext}) is the extra-cellular hydrostatic pressure [Charras and Paluch, 2008] for it to "stick" to the wall [Hawkins et al., 2009]. Then, a fine synchronization between the "stick-slip" phases and the life cycle of the bleb is necessary for the cell to have a net forward motion.

II.1.4 Poroelasticity in biology

Now that the mechanisms behind cell chimneying are clearer, we must concentrate on the material model that we choose for the cell. Since interstitial fluid flow is of such paramount importance in the formation of blebs, and thus in the regulation of chimneying migration, it needs to be carefully addressed in our model. Because of many illustrations found in biology textbooks, the cell is often seen as a fluid droplet in which the organelles bathe. The reality is quite different from the artistic views. Indeed, the cell cytoplasm appears to be very crowded, and very little room is left for the interstitial fluid to move (see Figure II.4).

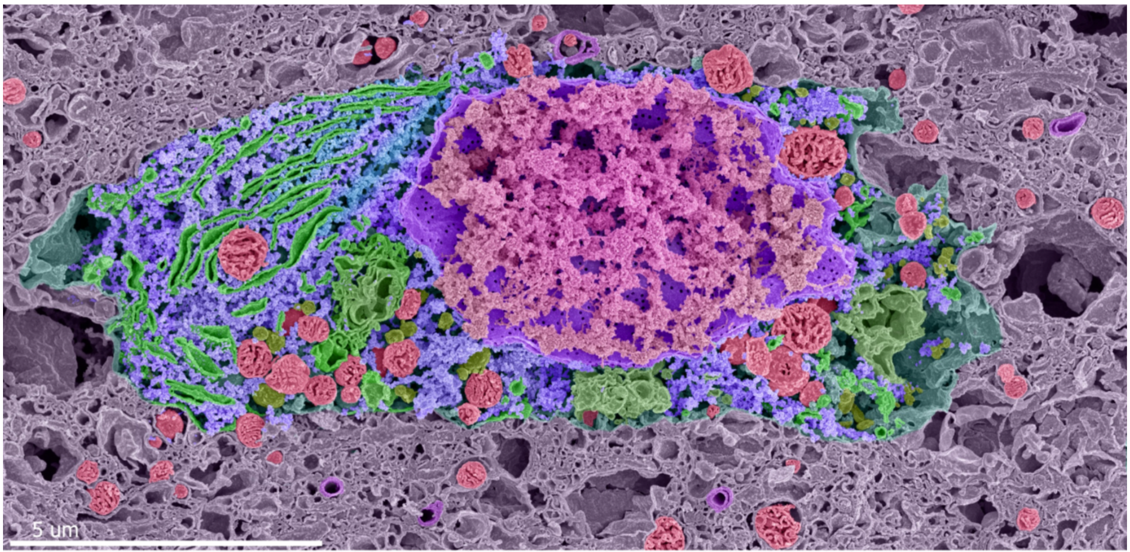

Sample Preparation: Dr. Patrick Nahirney, University of Victoria Medical Sciences uvic.ca/medsci/ Image credit and copyright: James Tyrwhitt-Drake, University of Victoria Advanced Microscopy Facility stehm.uvic.ca

Figure II.4: Colorized Scanning Electron Microscope image a neuron.

The structure resembles the one of sponges and porous rocks. Such media are typically described through poroelasticity theory to account for the transport of the interstitial fluid as well as the deformation of the solid structure. Cell modeling is not the first field of biomechanics getting into poroelasticity. Such models have been used to describe soft tissues [Pena et al., 1998], bones [Cowin, 1999], blood vessels [Thiriet, 2007] and the ECM [Vuong et al., 2017]. It has also been used for the cell nucleus [Cao et al., 2016] and cytoplasm [Taber et al., 2011; Strychalski et al., 2015; Ghosh et al., 2016]. The latter is however most often modeled as a visco-elastic medium [Karcher et al., 2003; Deveraux et al., 2017], but the relevance of interstitial fluid flow makes us question this assumption and a poroelastic representation seems more suited for bleb-based chimneying. Indeed, cell rheology is often explained through viscosity while the poroelasticity theory appears to be more fitted [Moeendarbary et al., 2013; Wei et al., 2016; Garcia et al., 2017; Hu et al., 2017; Mollaeian et al., 2018; Wang et al., 2018]. Among the previously cited poroelastic cell models, Strychalski et al. [2015] tackled the issue of cell blebbing and cell crawling and Taber et al. [2011] presented a very interesting model of confined actin-polymerization-based migration. Some models for cell blebbing exist without considering poroelasticity [Lim et al., 2013; Woolley et al., 2017], but no model of bleb-based chimneying including poroelasticity has been proposed yet. The results presented in the following section have been accepted for publication in *Molecular Cell Biology*.

II.1.5 The proposed model

The challenge in chimneying is to capture the very fine synchronization between the friction force with the confining surface and the bleb cycle. In this respect, we present in this chapter our FE model of a poroelastic cell. For reasons of numerical convergence, we develop it in 1D, since it is sufficient to capture the governing mechanism. The model revolves around three main ingredients: the constitutive relationship of the material, the active strain – as developed in previous models [Deveraux et al., 2017; Aubry et al., 2014; Allena and Aubry, 2012b; Allena, 2013; Allena and Aubry, 2012a; Allena, 2014; Allena et al., 2013] – solely at the rear of the cell and the Coulomb's friction force between the cell and the confining surface. Our goal is to explore a rarely studied motility mode and to show that, in terms of cell-environment interaction, the laws of mechanics alone are surprisingly sufficient to enable a net forward motion in a non-adhesive migration.

II.2 The poroelastic model

We first write all the equations of the model in 2D in order to stay close to our previously developed models, and will proceed to the 1D reduction on the final equations only.

II.2.1 Global equations of the model

The cell cytoplasm can be considered as a porous material – made of the cytoskeleton and the organelles – infiltrated with interstitial fluid. In such a configuration, two sorts of fluid-solid interactions may occur. First, a fluid-to-solid interaction takes place when a fluid displacement or an evolution of the intra-cellular pressure induces a variation of the cytoplasm volume. Second, a solid-to-fluid interaction may occur when the mechanical stresses applied to the cell provoke an evolution of the intra-cellular pressure and a displacement of the fluid. Our poroelastic approach is based on the theory developed by Terzaghi [1936] for geomechanics, and taken one step further for numerical purposes by Zienkiewicz [1999]. We consider that the total stress in the material is the superposition of the effective stress and the stress due to the fluid pressure. The effective stress is the Cauchy stress in the dry solid, which then follows the typical stress-strain relationship. As for the pressure, if we freeze the system at a certain time and measure the pressure inside the fluid, the difference between the total stress and the effective stress is the stress exerted by the fluid pressure on the system. In this framework, the total Cauchy stress $\boldsymbol{\sigma}$ is defined as:

$$\boldsymbol{\sigma} = \boldsymbol{\sigma}' - p_f \mathbf{I} \tag{II.1}$$

where $\boldsymbol{\sigma}'$ is the effective stress in the solid part, p_f is the hydrostatic fluid pressure, and $\mathbf{I}$ is the identity matrix. Biot models usually found in the literature offer refined considerations [Taber et al., 2011; Strychalski et al., 2015], but the approach in Eq.II.1 is accurate enough for our purpose.

The motor of cell blebbing lies in the high contractility of the cell rear, the uropod [Lorentzen et al., 2011]. As in previous works [Aubry et al., 2014], we model this contractility as an active strain through the decomposition of the deformation gradient tensor $\mathbf{F}$ as follows:

$$\mathbf{F} = \mathbf{F}_e \mathbf{F}_a \tag{II.2}$$

with $\mathbf{F}_e$ and $\mathbf{F}_a$ the elastic and active deformation gradient tensors, respectively. The deformation gradient is defined as $\mathbf{F} = \mathbf{I} + \mathbf{D_p u}$, where $\mathbf{D_p u}$ is the gradient of the displacement $\mathbf{u}$ with respect to the initial configuration $\mathbf{p}$. From here on, as in the previous chapter, we put ourselves in the small deformation hypothesis. Indeed, although the overall strain of the cell is not small, it may be considered as the combination of successive small deformations, thus making such a hypothesis acceptable. We can assume that $\mathbf{F}_a$ is close to the identity and thus approximate it by $\mathbf{F}_a = \mathbf{I} + \boldsymbol{\omega}_a + \boldsymbol{\epsilon}_a$ where $\boldsymbol{\omega}_a$ is the anti-symmetric part of $\mathbf{F}_a$ that defines the rotation and $\boldsymbol{\epsilon}_a$ is the symmetric part of $\mathbf{F}_a$ that defines the strain.

From Eq. II.2, we can then write:

$$\mathbf{F}_e = \mathbf{F}.\mathbf{F}_a^{-1} = (\mathbf{I} + \mathbf{D_x u})(\mathbf{I} - \boldsymbol{\omega}_a - \boldsymbol{\epsilon}_a) \tag{II.3}$$

Thus, the Green-Lagrange tensor $\mathbf{E}_e$ defined as $\mathbf{E} = \frac{1}{2}(\mathbf{F}^T.\mathbf{F} - \mathbf{I})$ reads:

$$\begin{aligned}\mathbf{E}_e &= \frac{1}{2}[(\mathbf{I}-\boldsymbol{\omega}_a-\boldsymbol{\epsilon}_a)^T(\mathbf{I}+\mathbf{D_x u})^T(\mathbf{I}+\mathbf{D_x u})(\mathbf{I}-\boldsymbol{\omega}_a-\boldsymbol{\epsilon}_a)-\mathbf{I}] \\ &= \frac{1}{2}(\mathbf{D_x u}+\mathbf{D_x u}^T-(\boldsymbol{\omega}_a+\boldsymbol{\omega}_a^T-2\boldsymbol{\epsilon}_a)\end{aligned} \tag{II.4}$$

The cell's strain is defined as $\boldsymbol{\epsilon} = \frac{1}{2}(\mathbf{D_x u}+\mathbf{D_x u}^T)$ and, in the hypothesis of small deformations, we eventually come up with:

$$\boldsymbol{\epsilon}_e = \boldsymbol{\epsilon} - \boldsymbol{\epsilon}_a \tag{II.5}$$

with $\boldsymbol{\epsilon}_e$ and $\boldsymbol{\epsilon}_a$ the elastic and the active cell strains, respectively.

Then, the constitutive mechanical law reads:

$$\boldsymbol{\sigma}' = \lambda Tr(\boldsymbol{\epsilon}-\boldsymbol{\epsilon}_a)\mathbf{I} + 2\mu(\boldsymbol{\epsilon}-\boldsymbol{\epsilon}_a) \tag{II.6}$$

with λ and μ the Lamé coefficients of the solid part, defined as $\lambda = \frac{E\nu}{(1+\nu)(1-2\nu)}$ and $\mu = \frac{E}{2(1+\nu)}$, where E and ν are the Young modulus and the Poisson's ratio of the solid phase, respectively and Tr the trace operator.

If the cell is confined in a horizontal micro-channel, we can assume that the role of the gravity will be minimal. Experimental work moreover proved that gravity does not influence the active mechanism of cell spreading in a micro-pillars assay [Pan et al., 2012] and we can then reasonably extend this hypothesis to our case. Since no volume forces are applied to the system, the cell fluid equilibrium equation then reads

$$\mathbf{Div}(\boldsymbol{\sigma}' - p_f\mathbf{I}) = \rho\mathbf{a} \tag{II.7}$$

where **Div** is the divergence and **a** is the acceleration, which is low but nonetheless relevant, at least from a numerical point of view. ρ is the weighted density defined as $\rho = \phi\rho_f + (1-\phi)\rho_s$, with ϕ the porosity of the cytoplasm, ρ_f the density of the interstitial fluid and ρ_s the density of the solid phase.

In order to model the fluid-solid interaction, we write down the mass conservation for each phase of the material locally. At such scale, the local quantities are marked with an asterisk and from the mass conservation of each phase, we can write [Bear and Bachmat, 1990; Coussy, 1995]:

$$\begin{aligned} c_{p,s}\frac{dp_s^*}{dt} + div(\mathbf{v}_s^*) = 0 \\ c_{p,f}\frac{dp_f^*}{dt} + div(\mathbf{v}_f^*) = 0 \end{aligned} \tag{II.8}$$

with $c_{p,s}$ and $c_{p,f}$ the compressibility of the solid and the fluid phase respectively. p_s^* and p_f^* are the local pressures $\mathbf{v}_s^*$ and $\mathbf{v}_f^*$ are the local velocities. The subscripts s and f stand for solid and fluid, respectively.

We perform a volume integration on a representative volume element (RVE) Ω of total volume V_t, composed of a solid phase Ω_s of volume V_s and a fluid phase Ω_f of volume V_f (see Figure II.5), to get a homogenized problem.

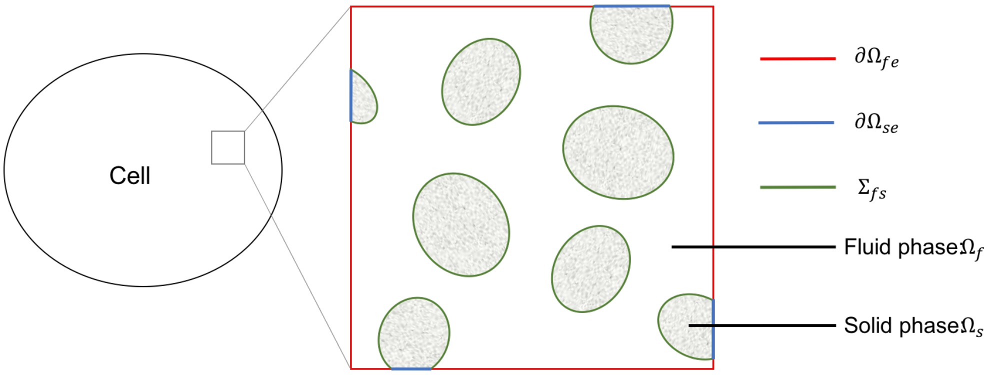

Figure II.5: Illustration of the poroelastic system.

$\partial\Omega_{se}$ and $\partial\Omega_{fe}$ are the exterior solid and fluid boundaries of the RVE, so that the total boundary $\partial\Omega_e = \partial\Omega_{se} \cup \partial\Omega_{fe}$. $\mathbf{n}_s$ and $\mathbf{n}_f$ are the outward normal vectors to each phase. The homogenized quantities are noted without the asterisk and we have:

$$\int_{\Omega_s} (c_{p,s}\frac{dp_s^*}{dt} + div(\mathbf{v}_s^*))\mathrm{d}V + \int_{\Omega_f} (c_{p,f}\frac{dp_f^*}{dt} + div(\mathbf{v}_f^*))\mathrm{d}V = 0 \tag{II.9}$$

which gives

$$c_{p,s}\frac{dp_s}{dt}V_s + c_{p,f}\frac{dp_f}{dt}V_f + \int_{\Omega_s} div(\mathbf{v}_s^*)\mathrm{d}V + \int_{\Omega_f} div(\mathbf{v}_f^*)\mathrm{d}V = 0 \tag{II.10}$$

The Stokes theorem allows us to write:

$$\begin{aligned} c_{p,s}\frac{dp_s}{dt}V_s + c_{p,f}\frac{dp_f}{dt}V_f + \int_{\partial\Omega_{se}} (\mathbf{v}_s^*, \mathbf{n}_s)\mathrm{d}S + \int_{\Sigma_{fs}} (\mathbf{v}_f^*, \mathbf{n}_f)\mathrm{d}S \\ + \int_{\partial\Omega_{fe}} (\mathbf{v}_f^*, \mathbf{n}_f)\mathrm{d}S + \int_{\Sigma_{fs}} (\mathbf{v}_s^*, \mathbf{n}_s)\mathrm{d}S = 0 \end{aligned} \tag{II.11}$$

where $(\mathbf{a}, \mathbf{b})$ indicates the scalar product of two vectors $\mathbf{a}$ and $\mathbf{b}$.

On Σ_{fs}, $\mathbf{n}_s = -\mathbf{n}_f$ and $\mathbf{v}_s = \mathbf{v}_f$, so $\int_{\Sigma_{fs}} (\mathbf{v}_f^*, \mathbf{n}_f)\mathrm{d}S + \int_{\Sigma_{fs}} (\mathbf{v}_s^*, \mathbf{n}_s)\mathrm{d}S = 0$. The previous equation then becomes

$$c_{p,s}\frac{dp_s}{dt}V_s + c_{p,f}\frac{dp_f}{dt}V_f + \int_{\partial\Omega_e} (\mathbf{v}_s^*, \mathbf{n}_s)\mathrm{d}S + \int_{\partial\Omega_{fe}} (\mathbf{v}_f^* - \mathbf{v}_s^*, \mathbf{n}_f)\mathrm{d}S = 0 \tag{II.12}$$

By applying the Stokes theorem the other way around and dividing everything by V_t, we introduce the porosity of the cytoplasm $\phi = \frac{V_f}{V_t}$ and we can write

$$\begin{aligned} c_{p,s}(1-\phi)\frac{dp_s}{dt} + c_{p,f}\phi\frac{dp_f}{dt}V_f + \frac{1}{V_t}\int_{\Omega} div(\mathbf{v}_s^*)\mathrm{d}V \\ + \frac{1}{V_t}\int_{\partial\Omega_{fe}}(\mathbf{v}_f^* - \mathbf{v}_s^*, \mathbf{n}_f)\mathrm{d}S = 0 \end{aligned} \tag{II.13}$$

$\frac{1}{V_t}\int_{\Omega} div(\mathbf{v}_s^*)\mathrm{d}V$ is the solid matrix deformation so $\frac{1}{V_t}\int_{\Omega} div(\mathbf{v}_s^*)\mathrm{d}V = Tr(\dot{\epsilon})$. The application of the Stokes theorem allows to rewrite the equation as:

$$c_{p,s}(1-\phi)\frac{dp_s}{dt} + c_{p,f}\phi\frac{dp_f}{dt} + Tr(\dot{\epsilon}) + div(\mathbf{v}_f - \mathbf{v}_s) = 0 \tag{II.14}$$

Additionally, the Darcy equation of fluid flow in porous media reads:

$$\mathbf{v}_f - \mathbf{v}_s = -\frac{1}{\eta_f}\mathbf{K}_f(\nabla p_f) \tag{II.15}$$

where η_f is the fluid viscosity, $\mathbf{K}_f$ is the fluid intrinsic permeability matrix and ∇ is the gradient operator.

By combining Eq. II.14 and II.15, we get the global poroelastic equation of our model:

$$c_{p,s}(1-\phi)\frac{dp_s}{dt} + c_{p,f}\phi\frac{dp_f}{dt} + Tr(\dot{\epsilon}) + div(-\frac{1}{\eta_f}\mathbf{K}_f(\nabla p_f)) = 0 \tag{II.16}$$

II.2.2 Reduction to a 1D problem

As previously explained, we choose to represent the cell as 1D element in the x direction. To do so, we average a 2D model in the other direction:

$$\bar{f} = \frac{1}{H}\int_{-H/2}^{H/2} f(z)\mathrm{d}z \tag{II.17}$$

where $\bar{f}$ defines the average of a function f and H is the height of the cell in the z direction.

Eq. II.1 then becomes:

$$\bar{\sigma}_{xx} = (\lambda + 2\mu)(\bar{\epsilon}_{xx} - \bar{\epsilon}_a) - \bar{p}_f = (\lambda + 2\mu)(\frac{\partial\bar{u}}{\partial x} - \bar{\epsilon}_a) - \bar{p}_f \tag{II.18}$$

where u is the displacement along the x-axis.

The integration of Eq. II.7 along the z-axis gives:

$$\rho\frac{\partial^2\bar{u}}{\partial t^2} = \frac{\partial\bar{\sigma}_{xx}}{\partial x} + \sigma_{xz}(\frac{H}{2}) - \sigma_{xz}(-\frac{H}{2}) \tag{II.19}$$

By combining these last two equations, we find:

$$\rho \frac{\partial^2 \bar{u}}{\partial t^2} - (\lambda + 2\mu)(\frac{\partial^2 \bar{u}}{\partial x^2} - \frac{\partial \bar{\epsilon}_a}{\partial x}) = -\frac{\partial \bar{p}}{\partial x} + \bar{\tau} \tag{II.20}$$

with $\bar{\tau} = \frac{1}{H}(\sigma_{xz}(\frac{H}{2}) - \sigma_{xz}(-\frac{H}{2}))$ the weighted shear stress.

In the global poroelastic equation II.16, we assume that we can neglect the solid phase compressibility so that the final equation then reads:

$$c_{p,f}\phi \frac{\partial \bar{p}_f}{\partial t} + \frac{\partial}{\partial t}\frac{\partial \bar{u}}{\partial x} = k \frac{\partial^2 \bar{p}_f}{\partial x^2} \tag{II.21}$$

where $k = \frac{K_f}{\eta_f}$ is the effective permeability, K_f being the scalar version of $\mathbf{K}_f$ due to the 1D reduction.

Boundary conditions

Here, the cell membrane is not permeable to outside fluid. We choose this hypothesis as a first approximation, even though we are aware of the importance of water permeation in cells [Murata et al., 2000], in order to build a first model that shall later be improved. Then, the boundary conditions on the fluid at both ends of the cell read $K_f \nabla \bar{p}_f = 0$. From a mechanical point of view, the outside fluid pressure is negligible so that $\sigma_{xx} = 0$ at both ends. Besides, we consider the cell to be at rest at the initial time $t = 0$.

II.2.3 The Coulomb's friction law

The ability of the cell to progress in confinement is linked to the friction generated when it comes in contact with the confining surface. Assuming that the contact is established between the cell and the confining surface, the Coulomb's friction-sliding law reads [Coulomb, 1821; Pfeiffer, 2008]:

$$\frac{\partial \bar{u}}{\partial t} = \begin{cases} 0 & \text{if } |\bar{\tau}| < \mu_f |\bar{\sigma}_{zz}| - \text{stick phase} \\ -\lambda_c \bar{\tau} & \text{if } |\bar{\tau}| = \mu_f |\bar{\sigma}_{zz}| - \text{slip phase} \end{cases} \tag{II.22}$$

with λ_c a scalar and μ_f the friction coefficient.

Then, in the slipping phase, we can write

$$\lambda_c = \frac{|\frac{\partial \bar{u}}{\partial t}|}{|\bar{\tau}|}$$

As a result,

$$\bar{\tau} = -|\bar{\tau}| \frac{\frac{\partial \bar{u}}{\partial t}}{|\frac{\partial \bar{u}}{\partial t}|}$$

Eventually,

$$\bar{\tau} = -\mu_f|\bar{\sigma}_{zz}|\frac{\frac{\partial\bar{u}}{\partial t}}{|\frac{\partial\bar{u}}{\partial t}|}$$

Besides, if we assume that the strain in the z-direction is negligible, we can write $\sigma_{zz} = -p_f$

All in all, we obtain

$$\bar{\tau} = -\mu_f|\bar{p}_f|\frac{\frac{\partial\bar{u}}{\partial t}}{|\frac{\partial\bar{u}}{\partial t}|} = -\mu_f|\bar{p}_f|sign(\frac{\partial\bar{u}}{\partial t}) \tag{II.23}$$

with $sign(\cdot)$ the sign function.

This force can be described in Figure II.6.

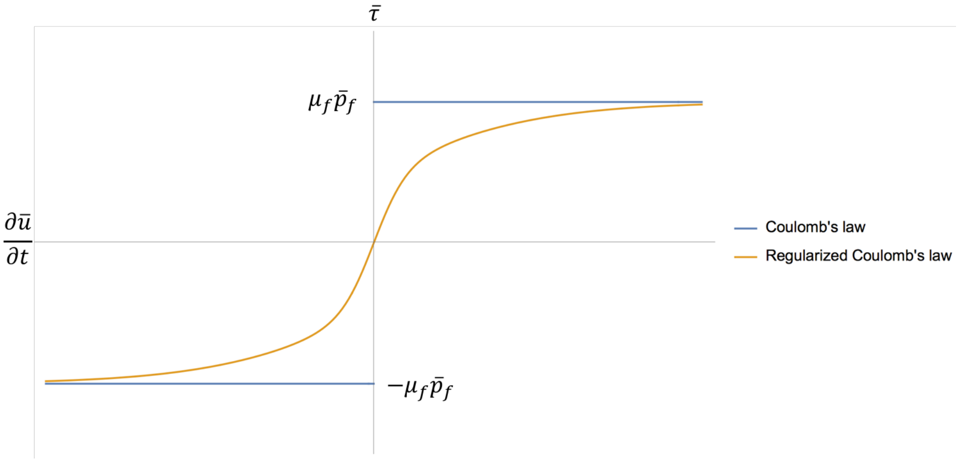

Figure II.6: Diagram of the Coulomb's friction force and its regularized form.

As we can see, the classical difficulty with Coulomb's law is that it is not a continuous function. For a zero velocity, there are infinite values for $\bar{\tau}$ and if $\bar{\tau}$ reaches its threshold, there is no way to determine the velocity. In order to solve this issue, we use a regularized sign function .

The regularized Coulomb's law reads [Aström and Canudas de Wit, 2008]:

$$\bar{\tau} = -\mu_f|\bar{p}_f|smsign(\frac{\partial\bar{u}}{\partial t}) \tag{II.24}$$

where $|\bar{\sigma}_{zz}| = |\bar{p}_f|$ if we consider that the strain occurs solely in the x direction. $smsign(\cdot)$ is the regularized form of the sign function.In this respect the shear stress is always smaller than $\mu_f|\bar{p}_f|$ with a vanishing velocity and very close to $\mu_f|\bar{p}_f|$ when the sliding velocity is larger. This smoothed sliding friction has often been used in non linear dynamical or mechanical systems. It requires only one parameter and it generates stable, efficient and fast computations.

II.2.4 Active strain

Cells that use bleb-based migration present a very particular type of active deformation. Indeed, this migration mode does not require actin polymerization, but solely relies on cyclic myosin-driven contractility in the uropod, the cell's rear. In our model, the active strain $\bar{\epsilon}_a(x,t)$ is written as a time periodic function (see Figure II.7) of period T_0, spatially localized $\forall x \in [x_0 - \frac{dx_0}{2}; x_0 + \frac{dx_0}{2}]$, as follows, with x_0 and dx_0 geometrical parameters defining the active strain zone in the cell:

$$\bar{\epsilon}_a(x,t) = -e_{a,0}(h(t-t_{0,up},s) - h(t-t_{0,down},s))\ \forall x \in [x_0 - \frac{dx_0}{2}; x_0 + \frac{dx_0}{2}] \tag{II.25}$$

where $e_{a,0}$ is the amplitude, $t_{0,cont}$ and $t_{0,decont}$ describe the time at which the contraction/decontraction occurs and s_a regulates the slope of the active strain.

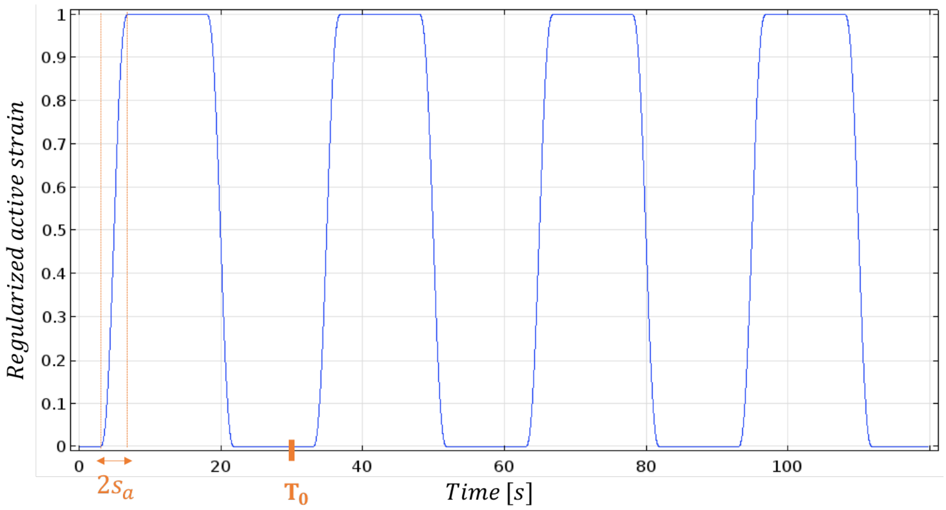

Figure II.7: Graphical representation of the regularized active strain during four cycles of 30 s each.

The relatively fast contraction and decontraction, over a time of 4 s, was chosen so that the resulting pressure would be high enough for the creation of a bleb. The value of $T_0 = 30s$ was chosen to fit the blebbing time scale found in the literature [Charras and Paluch, 2008].

II.2.5 Blebbing and Young's modulus

Bleb initiation starts from the weakening of bonds between the actin cortex and the cell membrane. The bleb then grows until such bonds are reformed, thus stabilizing the bleb. In order to model this local weakening, we chose a quite raw approximation to begin with: the cell's Young's modulus E_{cell} is locally weakened at the cell front, which enables easier blebbing, such that

$$E_{cell} = \begin{cases} E_{cell,0} & \text{if } x < \frac{3}{4}L_{cell} \\ (1-D)E_{cell,0} & \text{if } x \geq \frac{3}{4}L_{cell} \end{cases} \tag{II.26}$$

where $E_{cell,0}$ is the un-damaged cell's Young's modulus, L_{cell} is the cell's dimension and D is the damage coefficient.

To sum up, our poroelastic model rests on three main features: the active strain, as described in Eq. II.25, the poroelastic laws of the model, that is recapitulated in Eq. II.20 and II.21, and the self-synchronized friction law, described in its final form in Eq. II.26.

II.3 Results

In this section, we present the results of our 1D model, implemented in COMSOL Multiphysics©. The contractile zone at the rear of the cell and the blebbing front zone are both 5 μm long. The description and value of each parameter are listed in Table II.1. We use quadratic finite elements for the displacement variable and linear elements for the intra-cellular pressure to prevent mesh locking phenomena. The mesh is a 1D uniform one with a discretization length of 0.5 μm. In the solver parameters, a fifth degree Backwards Euler integration is employed and at each time step, a Newton method is used with a relative tolerance of 0.01 with regards to both fields. A computational run for 120 s physical time takes about 3 minutes CPU time.

Table II.1: Values and description of the model's parameters

Parameter	Description	Value (unit)	References
L_{cell}	Cell dimension	20 μm	
$E_{cell,0}$	Cell Young's modulus	1 kPa	[Kuznetsova et al., 2007]
D	Damage coefficient	0.9	
ρ	Weighted cell density	1000 kg/m^3	
k	Effective permeability	10^{-14} $m^4/N.s$	[Guilak et al., 2006]
$c_{p,f}$	Compressibility of the cell's fluid phase	5×10^{-4} Pa^{-1}	

ϕ	Cytoplasm porosity	0.5	[Taber et al., 2011]
μ_f	Friction coefficient	0.3	
$e_{a,0}$	Amplitude of the active strain	0.8	
x_0	Geometrical parameter of the active strain	2.5 μm	
dx_0	Geometrical parameter of the active strain	5 μm	
T_0	Period of the active strain	30 s	[Charras and Paluch, 2008]
$t_{0,up}$	Temporal parameter of the active strain	5 s	
$t_{0,down}$	Temporal parameter of the active strain	20 s	
s_a	Temporal parameter of the active strain	2 s	

We first show that the friction force leads to a self synchronization which enables a net cell motion forward. Then, we proceed to a sensibility analysis to identify the key parameters that determine the ability of the cell to successfully migrate, and to study the influence of the secondary parameters on the migration speed.

II.3.1 A successful synchronization and the cell migrates

A new point tackled by this model is that no adhesion is required for the cell to move forward. Moreover, what gets really interesting is that the synchronization between the Coulomb's friction force and the cell motion is self-determined. In fact, there is no need for a synchronization function, as it was the case in our previous works [Deveraux et al., 2017; Aubry et al., 2014; Allena, 2014], and mechanics alone regulates this interaction.

We perform an analysis of our model on 4 periods of active strain (i.e. 120 s). The first contraction cycle shows a different behaviour from the following ones and can be seen as a necessary step to reach a new dynamic equilibrium. Then, the further analyses will be made excluding this initial cycle. Obviously, in the absence of friction ($\mu_f = 0$), the cell pulsates on place but does not move forward (see Figure II.8 a). This configuration is interesting to study the poroelastic part of the model. Indeed, we observe a lag time between the displacement of the cell rear, due to the active contraction, and the one of the cell front, that is a direct consequence of poroelasticity. Plotting the displacement of the cell front and rear rather than their position, which would simply induce an offset of the front, allows to spot more easily if the cell is overall contracted or extended. Besides, the intra-cellular pressure p_f is transported towards the front of the cell over one period of active strain (see Figure II.8 b), which enables the development of a frontal bleb. Due to blebbing, the pressure does not have time to build up at the front, which explains the low values compared to the pressure at the rear (30 Pa at the front vs 400 Pa at the rear).

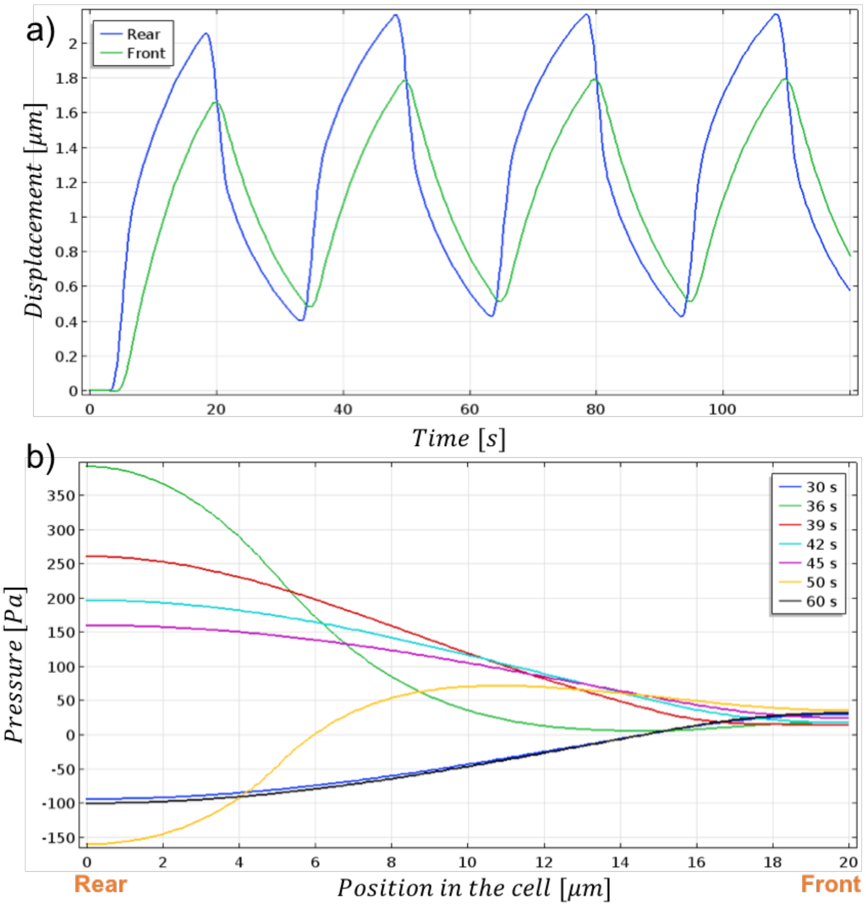

Figure II.8: Results of the poroelastic migration simulation in the absence of friction. Graphical representation of a) the displacement of the rear (blue) and front (green) extremities of the cell over four periods of active strain and b)the intra-cellular pressure along the cell length over one period of active strain

a Poroelasticity enables cell blebbing

After pointing out the influence of poroelasticity, the full model is studied, now including the friction force with $\mu_f = 0.3$. First, the pressure evolution inside the cell does not change from the previous case, which is not surprising since poroelasticity occurs in the same way. However, the displacement of the cell is strongly impacted (see Figure

II.9). The lag between the displacement of the rear and front of the cell is very similar to the previous case, but a net forward motion of the cell of 2 μm for the first cycle, and then 4 μm per cycle occurs. The cell migrates at an average speed of 8 $\mu m/min$, which is in the range of the values experimentally found for blebbing cells in confinement [Ibo et al., 2016; Liu et al., 2015; Yip et al., 2015].

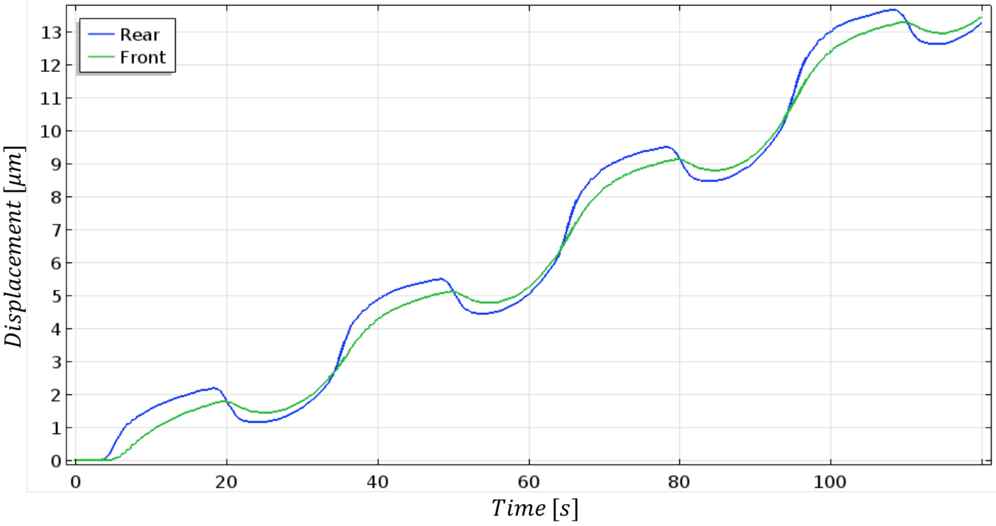

Figure II.9: Results of the poroelastic migration simulation with friction ($\mu_f = 0.3$). Graphical representation of the displacement of the rear (blue) and front (green) extremities of the cell over three periods of active strain

b The fine action of the friction force

Once made sure that our poroelastic model does enable bleb formation, we need to take it to the next step and find the parameters that will generate a net forward motion, which is the goal of the Coulomb's friction force. To do so, we first integrate the friction force over the whole cell to study the total force F_{tot} applied to the cell. When F_{tot} is negative, it generally prevents a forward motion and, when negative, it prevents a backward motion. During cycle 2 (and the following ones), two events need to be addressed: first a negative peak of -1.45 nPa at 35.5 seconds and second, a positive rise up to 0.7 nPa from 55 seconds to the end of the cycle (see Figure II.10). However, this global view conceals the local phenomena, which are of great interest here in order to pinpoint where the friction is the strongest.

To do so, we study the first peak at $t = 35.5$ s corresponding to the contraction and the time period from 55 to 60 s – right after decontraction – and plot the friction force $\bar{\tau}$ along the cell length every second from 55 to 60 s. During contraction, there is a strong friction at the uropod which is the direct consequence of the rear shrinkage. Indeed,

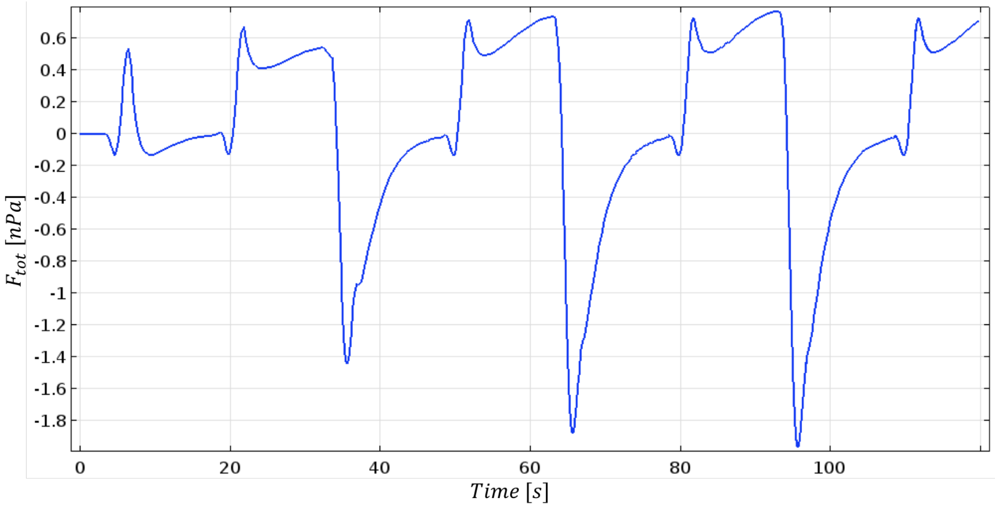

Figure II.10: Graphical representation of the total force applied to the cell.

the friction is negative from 0 to 4 μm and positive from 4 to 7 μm (see Figure II.11 a). The cell is then mostly blocked from moving forward because the negative part of $\bar{\tau}$ is much stronger than the positive one. If we focus on what occurs after the decontraction however, the picture is quite different. As time progresses, $\bar{\tau}$ increases in the positives at the rear and slightly decreases in the negatives at the front (see Figure II.11 b). This means that the friction necessary for the cell to move forward is mostly located in the rear part of the cell and not at the bleb, as it has been suggested in exploratory works on blebbing migration [Charras and Paluch, 2008].

These results are very interesting since they offer a completely mechanics-based insight of chimneying. In fact, although often observed, this phenomenon is quite unclear from the mechanical point of view. Hypotheses were made that the cell pushed against the confining walls, but no further mechanical inquiries were undertaken. Our model, although still preliminary, already unveils interesting mechanisms. First, it proves that a simple mechanical friction force is sufficient for the cell to move forward at a reasonable rate. Second, it reveals that the friction required for chimneying is located at the rear of the cell during the uropod decontraction.

II.3.2 Sensibility study

Now, we study the influence of the parameters on the cell behaviour. Some parameters are crucial to the migration, while others simply regulate its amplitude.

Then, the model's parameters can be divided into three categories :

Discriminating: they determine whether the cell migrates or not : μ_f, $c_{p,f}$, E_{cell}

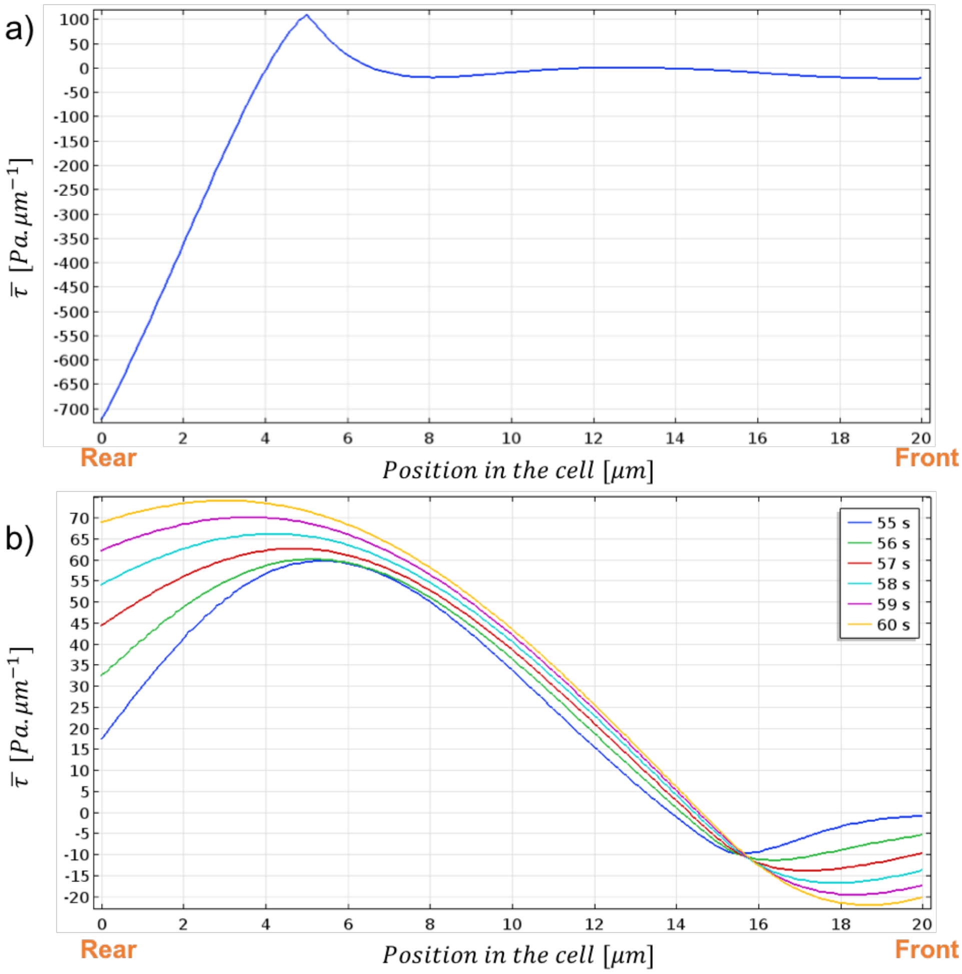

Figure II.11: Graphical representation of a) friction force per unit length along the cell profile at t=35.5 s, b) friction force per unit length along the cell profile between 55 and 60 s with a line every 3 second

Non-discriminating: they determine how fast the cell migrates : k, s_a

Technical: they purely define the problem : L_{cell}, ρ, ϕ, $e_{a,0}$, x_0, dx_0, T_0, $t_{0,up}$, $t_{0,down}$

a The conditions for a successful synchronization

As seen in the Section 3.1, the friction is the corner stone of our model: without it, no migration is possible. Intermediate values of the friction coefficient μ_f lead to intermediate migration speed, as could be expected (see Figure II.12 a). The Young's modulus was chosen at 1 kPa. Each cell type has a different range of Young's modulus, making it interesting to study its influence on cell motility in the prospect of looking at specific cell types. There appears to be an optimum in cell displacement for E_{cell} = 1000 Pa. For higher values, the migration speed decreases and at 5 kPa, the cell may even go in the opposite direction (see Figure II.12 b). The decrease of the cell compressibility $c_{p,f}$ induces a faster migration but, more importantly, a too high compressibility leads to no migration or even a backward one (see Figure II.12 c). In each case, this is due to an insufficient level of intra-cellular pressure mobilization with respect to the friction force.

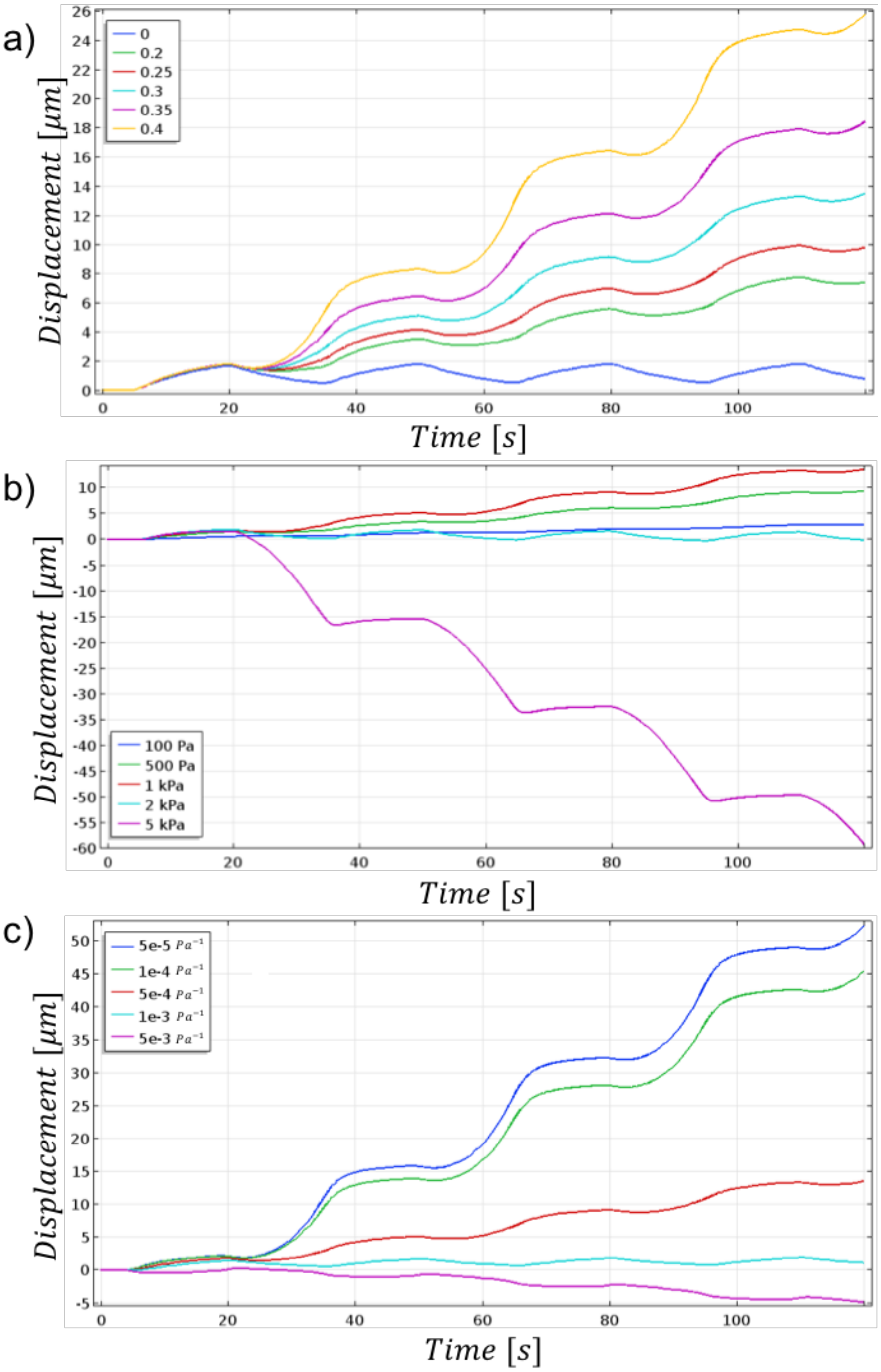

Figure II.12: Cell front displacement - Parametric study on a) μ_f b) E_{cell} c) $c_{p,f}$.

b Sensitivity of the other parameters

The others parameters simply define how fast the cell migrates, but they do not influence the capacity of the cell to migrate. The rate of active strain, directly linked to s_a, influences chimneying velocity: the faster it is (the lower s_a is), the faster the cell migrates (see Figure II.13 a). Concerning the effective permeability k, we observe the same trend as for the Young's modulus, but we do not reach a backwards migration.

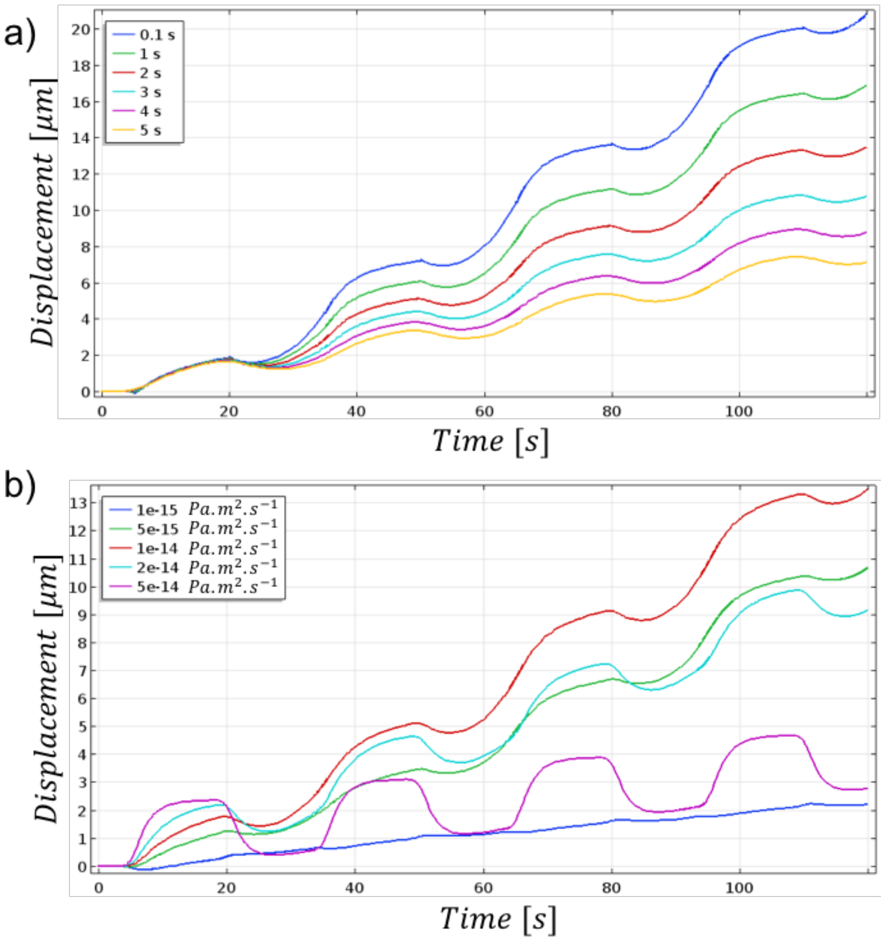

Figure II.13: Cell front displacement - Sensibility study on a) s_a b) k.

In order to get a new insight on our results, we introduce the so-called half-reduced time $t_{1/2} = \frac{L_{cell}^2}{2kE_{cell}}$. It gives an order of time needed to observe the poroelastic phenomenon. The values of $t_{1/2}$ for the values of the parameters tested in the parametric study are listed in Table II.2.

From this table, we can see that the optimal migration speed occurs when $t_{1/2}$ is ten folds grater than s_a (i.e. $t_{1/2} = 20s$). Indeed, for greater values of $t_{1/2}$, there is no time for intra-cellular fluid flow to occur, and for the lowest values, the pressure does not

Table II.2: Half-reduced time values for different parameters couples

$t_{1/2}$ (s)	$E_{cell}(Pa)$	k $(m^4/N.s)$
200	1000	10^{-15}
	100	10^{-14}
40	1000	5.10^{-15}
	500	10^{-14}
20	1000	10^{-14}
10	1000	2.10^{-14}
	2000	10^{-14}
4	1000	5.10^{-14}
	5000	10^{-14}

have time to build up before the fluid leaves the cell rear. Since we saw that the friction force occurs at the rear of the cell, we understand that if there is no pressure increase, then the friction remains too low to enable migration. In the case of $E_{cell} = 5000$ Pa, the friction force is too negative, and the cell goes the wrong way.

II.4 Discussion and Conclusion

Our preliminary model presents very interesting insights on the combined role of poroelasticity and passive friction force during the migration mode known as chimneying. We focus on the sharp synchronization between poroelastic-based blebbing and passive friction force. In this respect, we chose to implement a 1D model of a generic cell which could be adapted to fit a more specific cell type. This 1D reduction is of course a rough simplification that induces a loss of information, but it simplifies the problem and allows to pinpoint the exact mechanisms that govern chimneying. Finding out the values of the model's parameters was complex due to the lack of experimental data, or the wide range of the data that could be found. Thus, after starting with first-approximation values of the parameters from the literature, we iterated until getting an acceptable set of parameters for the model to run (see Table II.1). The model's sensibility on cell stiffness highlights the various behaviour that could be expected from various cell types and it raises the question of the possibility of such migration mode in stiffer cells.

Despite the simplifications, there is still a lot to learn from this model. First, it shows the need for poroelasticity intra-cellular fluid flows in the process of blebbing. Indeed, the active contraction on the cell's uropod causes an increase of intra-cellular pressure at the rear that propagates through the cell. When the pressure wave reaches the mechanically weakened front of the cell, it induces a bleb growth. The last pillar is the self-synchronized friction force between the cell and the confining surface. Indeed, contrarily to our previous works [Deveraux et al., 2017; Aubry et al., 2014], the synchronization between the active strain and the force from the cell-environment interaction is completely self-determined, which is a major step towards a more autonomous model. Eventually, our model sheds light on the question of the location of the friction force needed for the cell to move forward: the force enabling migration is the strongest at the cell rear. These findings allow further research to focus more specifically on the cell's uropod and experimentally investigate the molecular processes at stake there.

In order take this further, we could consider more cellular components, which can be described with specific constitutive properties by using spatial characteristic functions as in Chapter I. The presence of the nucleus for instance could trigger interesting phenomena, such as a piston effect [Petrie et al., 2014]. Besides, we control the cell's contractility by a purely time-dependent determined function, that is disconnected from the reality of the acto-myosin network behaviour. In this respect, it would be interesting to "biologize" the deformation by letting molecular dynamics equations govern it, as was done in some very elegant works [Deshpande et al., 2008; Cao et al., 2016; Moure and Gomez, 2017]. This exploratory model is only a proof of concept of future more complex versions that could be developed to study the influence of specific cell features in unhealthy cells. Indeed, blebbing is involved in various diseases such as cancer metastasis [Friedl, 2004; Sahai and Marshall, 2003] or angiogenesis [Gebala et al., 2016] and our model could be adapted to these various cases to deepen our understanding of the mechanics of such phenomena.

Bibliography

Allena, R. (2013). Cell Migration with Multiple Pseudopodia: Temporal and Spatial Sensing Models. *Bulletin of Mathematical Biology*, 75(2):288–316. 66

Allena, R. (2014). Mechanical modelling of confined cell migration across constricted-curved micro-channels. *Molecular and Cellular Biomechanics: MCB*, 11(3):185–208. 66, 75

Allena, R. and Aubry, D. (2012a). A purely mechanical model to explore amoeboid cell migration. *Computer Methods in Biomechanics and Biomedical Engineering*, 15(sup1):14–16. 66

Allena, R. and Aubry, D. (2012b). 'Run-and-tumble' or 'look-and-run'? A mechanical model to explore the behavior of a migrating amoeboid cell. *Journal of Theoretical Biology*, 306:15–31. 66

Allena, R., Aubry, D., and Sharpe, J. (2013). On the Mechanical Interplay Between Intraand Inter-Synchronization During Collective Cell Migration: A Numerical Investigation. *Bulletin of Mathematical Biology*, 75(12):2575–2599. 66

Arroyo, M. and Trepat, X. (2017). Hydraulic fracturing in cells and tissues: fracking meets cell biology. *Current Opinion in Cell Biology*, 44(Supplement C):1–6. 63

Aström, K. J. and Canudas de Wit, C. (2008). Revisiting the LuGre friction model. *IEEE Control Systems Magazine*, 28(6):101–114. 72

Aubry, D., Thiam, H., Piel, M., and Allena, R. (2014). A computational mechanics approach to assess the link between cell morphology and forces during confined migration. *Biomechanics and Modeling in Mechanobiology*, 14(1):143–157. 66, 67, 75, 83

Bear, J. and Bachmat, Y. (1990). *Introduction to Modeling of Transport Phenomena in Porous Media*. Springer Netherlands, Dordrecht. DOI: 10.1007/978-94-009-1926-6. 68

Cao, X., Moeendarbary, E., Isermann, P., Davidson, P. M., Wang, X., Chen, M. B., Burkart, A. K., Lammerding, J., Kamm, R. D., and Shenoy, V. B. (2016). A Chemomechanical Model for Nuclear Morphology and Stresses during Cell Transendothelial Migration. *Biophysical Journal*, 111(7):1541–1552. 65, 83

Charras, G. and Paluch, E. (2008). Blebs lead the way: how to migrate without lamellipodia. *Nature reviews Molecular cell biology*, 9(9):730–736. 61, 63, 64, 73, 75, 78, 154

Chhabra, E. S. and Higgs, H. N. (2007). The many faces of actin: matching assembly factors with cellular structures. *Nature Cell Biology*, 9(10):1110–1121. 61

Cooper, G. M. (2000). *The Cell*. Sinauer Associates, 2nd edition. 63

Coulomb, C. A. (1821). *Théorie des machines simples (Nouv. Éd.)*. Bachelier, Paris. 71

Coussy, O. (1995). *Mechanics of porous continua*. Wiley, Chichester; New York. OCLC: 32390496. 68

Cowin, S. C. (1999). Bone poroelasticity. *Journal of Biomechanics*, 32(3):217–238. 65

Cramer, Siebert, M., and Mitchison, T. J. (1997). Identification of novel graded polarity actin filament bundles in locomoting heart fibroblasts: implications for the generation of motile force. *J Cell Biol*, 136(6). 62

Deshpande, V. S., Mrksich, M., McMeeking, R. M., and Evans, A. G. (2008). A biomechanical model for coupling cell contractility with focal adhesion formation. *Journal of the Mechanics and Physics of Solids*, 56(4):1484–1510. 83

Deveraux, S., Allena, R., and Aubry, D. (2017). A numerical model suggests the interplay between nuclear plasticity and stiffness during a perfusion assay. *Journal of Theoretical Biology*, 435:62–77. 65, 66, 75, 83

Friedl, P. (2004). Prespecification and plasticity: shifting mechanisms of cell migration. *Current Opinion in Cell Biology*, 16(1):14–23. 61, 83

Garcia, P. D., Guerrero, C. R., and Garcia, R. (2017). Time-resolved nanomechanics of a single cell under the depolymerization of the cytoskeleton. *Nanoscale*, 9(33):12051–12059. 66

Gebala, V., Collins, R., Geudens, I., Phng, L.-K., and Gerhardt, H. (2016). Blood flow drives lumen formation by inverse membrane blebbing during angiogenesis in vivo. *Nature Cell Biology*, 18(4):443–450. 83

Ghosh, S., Ozcelikkale, A., Dutton, J. C., and Han, B. (2016). Role of intracellular poroelasticity on freezing-induced deformation of cells in engineered tissues. *Journal of The Royal Society Interface*, 13(123):20160480. 65

Guilak, F., Haider, M. A., Setton, L. A., Laursen, T. A., and Baaijens, F. P. T. (2006). Multiphasic models of cell mechanics. In Mofrad, M. R. K. and Kamm, R. D., editors, *Cytoskeletal Mechanics*, pages 84–102. Cambridge University Press, Cambridge. DOI: 10.1017/CBO9780511607318.006. 74

Hawkins, R. J., Piel, M., Faure-Andre, G., Lennon-Dumenil, A. M., Joanny, J. F., Prost, J., and Voituriez, R. (2009). Pushing off the Walls: A Mechanism of Cell Motility in Confinement. *Physical Review Letters*, 102(5):058103. 65

Henrichsen, J. (1972). Bacterial surface translocation: a survey and a classification. *Bacteriological Reviews*, 36(4):478–503. 61

Hu, J., Jafari, S., Han, Y., Grodzinsky, A. J., Cai, S., and Guo, M. (2017). Size- and speed-dependent mechanical behavior in living mammalian cytoplasm. *Proceedings of the National Academy of Sciences*, 114(36):9529–9534. 66

Ibo, M., Srivastava, V., Robinson, D. N., and Gagnon, Z. R. (2016). Cell Blebbing in Confined Microfluidic Environments. *PloS One*, 11(10):e0163866. 61, 77

Kappe, S. H. I., Buscaglia, C. A., Bergman, L. W., Coppens, I., and Nussenzweig, V. (2004). Apicomplexan gliding motility and host cell invasion: overhauling the motor model. *Trends in Parasitology*, 20(1):13–16. 61

Karcher, H., Lammerding, J., Huang, H., Lee, R. T., Kamm, R. D., and Kaazempur-Mofrad, M. R. (2003). A Three-Dimensional Viscoelastic Model for Cell Deformation with Experimental Verification. *Biophysical Journal*, 85(5):3336–3349. 65

Kuznetsova, T. G., Starodubtseva, M. N., Yegorenkov, N. I., Chizhik, S. A., and Zhdanov, R. I. (2007). Atomic force microscopy probing of cell elasticity. *Micron*, 38(8):824–833. 74

Lim, F. Y., Koon, Y. L., and Chiam, K.-H. (2013). A computational model of amoeboid cell migration. *Computer Methods in Biomechanics and Biomedical Engineering*, 16(10):1085–1095. 66

Liu, Y.-J., Le Berre, M., Lautenschlaeger, F., Maiuri, P., Callan-Jones, A., Heuzé, M., Takaki, T., Voituriez, R., and Piel, M. (2015). Confinement and Low Adhesion Induce Fast Amoeboid Migration of Slow Mesenchymal Cells. *Cell*, 160(4):659–672. 61, 77

Lorentzen, A., Bamber, J., Sadok, A., Elson-Schwab, I., and Marshall, C. J. (2011). An ezrin-rich, rigid uropod-like structure directs movement of amoeboid blebbing cells. *Journal of Cell Science*, 124(8):1256–1267. 63, 67

Lämmermann, T., Bader, B. L., Monkley, S. J., Worbs, T., Wedlich-Säldner, R., Hirsch, K., Keller, M., Färster, R., Critchley, D. R., Fässler, R., and Sixt, M. (2008). Rapid leukocyte migration by integrin-independent flowing and squeezing. *Nature*, 453(7191):51–55. 62, 63

Malawista, S. E., de Boisfleury Chevance, A., and Boxer, L. A. (2000). Random locomotion and chemotaxis of human blood polymorphonuclear leukocytes from a patient with Leukocyte Adhesion Deficiency-1: Normal displacement in close quarters via chimneying. *Cell Motility and the Cytoskeleton*, 46(3):183–189. 62

Maugis, B., Brugués, J., Nassoy, P., Guillen, N., Sens, P., and Amblard, F. (2010). Dynamic instability of the intracellular pressure drives bleb-based motility. *J Cell Sci*, 123(22):3884–3892. 62

Moeendarbary, E., Valon, L., Fritzsche, M., Harris, A. R., Moulding, D. A., Thrasher, A. J., Stride, E., Mahadevan, L., and Charras, G. T. (2013). The cytoplasm of living cells behaves as a poroelastic material. *Nature Materials*, 12(3):253–261. 66

Mogilner, A. and Manhart, A. (2018). Intracellular Fluid Mechanics: Coupling Cytoplasmic Flow with Active Cytoskeletal Gel. *Annual Review of Fluid Mechanics*, 50(1):347–370. 62

Mollaeian, K., Liu, Y., Bi, S., and Ren, J. (2018). Atomic force microscopy study revealed velocity-dependence and nonlinearity of nanoscale poroelasticity of eukaryotic cells. *Journal of the Mechanical Behavior of Biomedical Materials*, 78:65–73. 66

Moure, A. and Gomez, H. (2017). Phase-field model of cellular migration: Three-dimensional simulations in fibrous networks. *Computer Methods in Applied Mechanics and Engineering*, 320:162–197. 83

Murata, K., Mitsuoka, K., Hirai, T., Walz, T., Agre, P., Heymann, J. B., Engel, A., and Fujiyoshi, Y. (2000). Structural determinants of water permeation through aquaporin-1. *Nature*, 407(6804):599–605. 71

Paluch, E. K. and Raz, E. (2013). The role and regulation of blebs in cell migration. *Current Opinion in Cell Biology*, 25(5):582–590. 61

Pan, Z., Yan, C., Peng, R., Zhao, Y., He, Y., and Ding, J. (2012). Control of cell nucleus shapes via micropillar patterns. *Biomaterials*, 33(6):1730–1735. 68

Pena, A., Bolton, M. D., and Pickard, J. D. (1998). Cellular poroelasticity: A theoretical model for soft tissue mechanics. In *Proceedings of the Biot Conference on Poromechanics*, pages 475–480, Netherlands. A.A. Balkema. 65

Petrie, R. J., Koo, H., and Yamada, K. M. (2014). Generation of compartmentalized pressure by a nuclear piston governs cell motility in a 3d matrix. *Science*, 345(6200):1062–1065. 62, 83

Pfeiffer, F. (2008). *Mechanical system dynamics*. Berlin Springer. 71

Sahai, E. and Marshall, C. J. (2003). Differing modes of tumour cell invasion have distinct requirements for Rho/ROCK signalling and extracellular proteolysis. *Nature Cell Biology*, 5(8):711–719. 61, 83

Silflow, C. D. and Lefebvre, P. A. (2001). Assembly and Motility of Eukaryotic Cilia and Flagella. Lessons from Chlamydomonas reinhardtii. *Plant Physiology*, 127(4):1500–1507. 61

Stroka, K. M., Jiang, H., Chen, S.-H., Tong, Z., Wirtz, D., Sun, S. X., and Konstantopoulos, K. (2014). Water Permeation Drives Tumor Cell Migration in Confined Microenvironments. *Cell*, 157(3):611–623. 62

Strychalski, W., Copos, C. A., Lewis, O. L., and Guy, R. D. (2015). A poroelastic immersed boundary method with applications to cell biology. *Journal of Computational Physics*, 282(Supplement C):77–97. 65, 66, 67

Taber, L., Shi, Y., Yang, L., and Bayly, P. (2011). A poroelastic model for cell crawling including mechanical coupling between cytoskeletal contraction and actin polymerization. *Journal of mechanics of materials and structures*, 6(1-4):569–589. 65, 66, 67, 75

Terzaghi, K. (1936). A fundamental fallacy in Earth pressure computations. *Boston Society Civil Engineers Journal*. 67

Thiriet, M. (2007). *Biology and Mechanics of Blood Flows: Part II: Mechanics and Medical Aspects*. Springer Science and Business Media. 65

Vale, R. D. and Milligan, R. A. (2000). The Way Things Move: Looking Under the Hood of Molecular Motor Proteins. *Science*, 288(5463):88–95. 62

Van Haastert, P. J. M. (2011). Amoeboid Cells Use Protrusions for Walking, Gliding and Swimming. *PLoS ONE*, 6(11):e27532. 61

Vuong, A.-T., Rauch, A. D., and Wall, W. A. (2017). A biochemo-mechano coupled, computational model combining membrane transport and pericellular proteolysis in tissue mechanics. *Proceedings of the Royal Society A: Mathematical, Physical and Engineering Science*, 473(2199):20160812. 65

Wang, L., Dong, J., and Xian, C. J. (2018). Computational Investigation on the Biomechanical Responses of the Osteocytes to the Compressive Stimulus: A Poroelastic Model. *BioMed Research International*. 66

Wei, F., Lan, F., Liu, B., Liu, L., and Li, G. (2016). Poroelasticity of cell nuclei revealed through atomic force microscopy characterization. *Applied Physics Letters*, 109(21):213701. 66

Wolf, K., Mazo, I., Leung, H., Engelke, K., von Andrian, U. H., Deryugina, E. I., Strongin, A. Y., Bröcker, E.-B., and Friedl, P. (2003). Compensation mechanism in tumor cell migration. *The Journal of Cell Biology*, 160(2):267–277. 61

Woolley, T. E., Gaffney, E. A., and Goriely, A. (2017). Random blebbing motion: A simple model linking cell structural properties to migration characteristics. *Physical Review E*, 96(1). 66

Yip, A. K., Chiam, K.-H., and Matsudaira, P. (2015). Traction stress analysis and modeling reveal that amoeboid migration in confined spaces is accompanied by expansive forces and requires the structural integrity of the membrane-cortex interactions. *Integrative Biology: Quantitative Biosciences from Nano to Macro*. 77

Zhou, E. H., Martinez, F. D., and Fredberg, J. J. (2013). Cell Rheology. *Nature materials*, 12(3). 63

Zienkiewicz, O. C. (1999). *Computational geomechanics with special reference to earthquake engineering*. Wiley, Chichester; New York. OCLC: 39313440. 67

Chapter III

Cell spreading on a micro-pillared substrate

Contents

III.1 Introduction

Throughout their lifetime, cells are in perpetual interaction with their environment. In order to survive, they constantly need to adapt to the various stimuli they encounter. Among these, cells are sensitive to mechanical cues to which they can react by altering their morphology and physiology [Benjamin and Hillen, 2003; Mammoto and Ingber, 2010; Versaevel et al., 2012; Swift et al., 2013]. As seen in Chapter I, cancerous cells can alter the mechanical properties of the nucleus to pass through tight gaps and create metastasis at a distant location from the primary tumour. As such, the evolution of nuclear morphology can be used as a biomarker in the diagnosis and prognosis of cancer patients [Schirmer and Heras, 2014; Ermis et al., 2016]. In order to characterize these cells and examine their behaviour in confined environments, the last decades have seen the fast development of patterned micro-fluidic devices [Lu et al., 2004; Rosenbluth et al., 2008; Hou et al., 2009; Davidson et al., 2009; Polacheck et al., 2011; Gossett et al., 2012; Isermann et al., 2012; Davidson et al., 2015]. Indeed, contrarily to intrusive devices like in AFM, micro-patterning allows to design a system in which we can observe the evolution of the cell morphology in a mechanically challenging environment without external disturbance. Among the vast possibilities offered by micro-fabrication, we focus here on topology-oriented devices, and more specifically on micro-pillared substrates.

III.1.1 Micro-pillared substrates and cell nucleus mechanics

Micro-pillars are most commonly used as an array of thin beams in traction force microscopy to access the interaction forces between a cell and its substrate [Style et al., 2014; Ghibaudo et al., 2011]. However, by controlling the material used, the size of the pillars, and the gap size between pillars, they can serve to control the shape of the nucleus [Pan et al., 2012; Hanson et al., 2015] and investigate the processes of nuclear self-deformation [Davidson et al., 2010; Badique et al., 2013; Eichhorn et al., 2015; Ermis et al., 2016] (see Fig. III.1). These recent experiments offer a new insight on nuclear deformation and raise further questions: Is gravity driving this movement [Pan et al., 2012] ? Is the nucleus being pulled or pushed [Davidson et al., 2010; Badique et al., 2013; Hanson et al., 2015] ? During these essays, suspended cells are seeded on the substrate on which they later deform. The first step to any migratory event in cells is its spreading and adhesion on the underlying substrate. It is then necessary to have a closer look at the mechanisms behind the process of cell spreading before going any further.

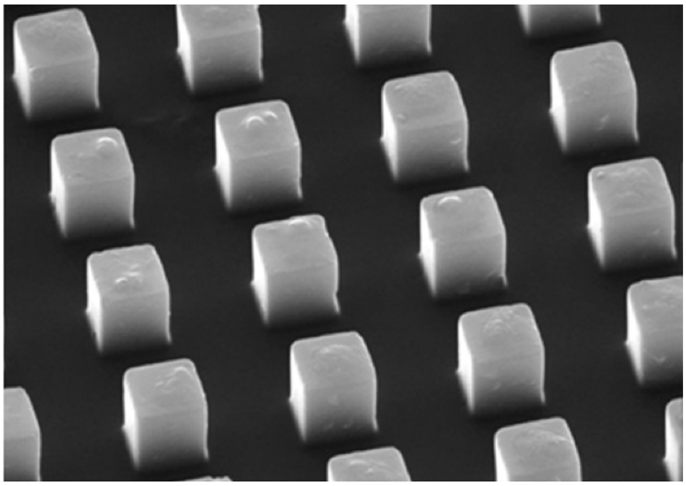

Figure III.1: Example of micro-fabricated PDMS micro-pillars array [Badique et al., 2013].

III.1.2 Cell spreading on a flat substrate

From a suspended to a crawling state, the cell first comes into contact with the substrate, then spreads on it and eventually polarizes – i.e. looses its symmetry – to start crawling [McGrath, 2007] (see Fig. III.2). The process of cell spreading can be divided in two different phases: an early and a late one [Cuvelier et al., 2007; Döbereiner et al., 2004].

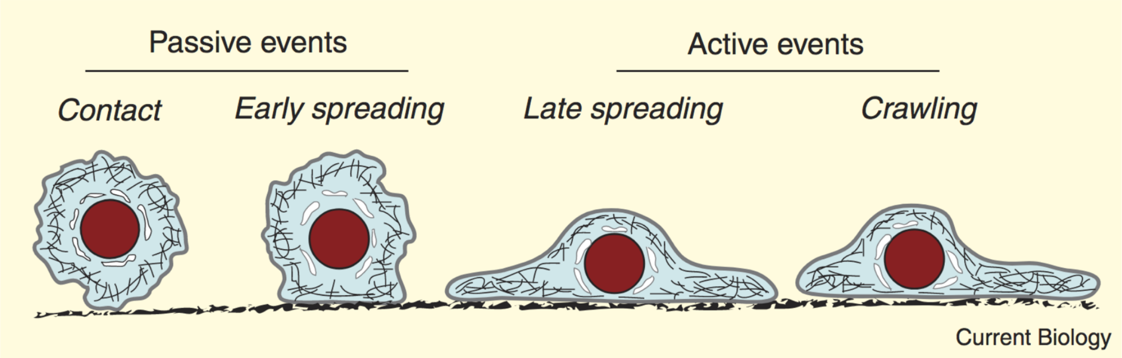

Figure III.2: Steps from a suspended to a crawling cell [McGrath, 2007].

The early phase is completely passive: under the action of gravity only, the cell settles on the substrate and deforms depending on its rigidity. On the opposite, the late spreading phase is an active one. There is a cyclic occurrence of micron-sized lamellipodia formation through actin polymerization, and cytoskeleton contraction through acto-myosin based stress fibers linked to focal adhesions. It is the combination on both actin polymerization and myosin contraction that govern this late phase [Cai et al., 2006; Wakatsuki, 2003]. The late spreading phase can itself be decomposed in two steps [Keren, 2011; Gauthier et al., 2011]: a fast active spreading where the cell surface area is increased by membrane recruitment from a reservoir of folded regions, and a slower one in which additional membrane is recruited through exocytosis of internal membranes.

III.1.3 Cell-Matrix adhesions are the mechanical anchors of the cell

Except in the specific case of chimneying, the keys to a successful spreading or migration are focal adhesions. Focal adhesions (FAs) create a mechanical link between intracellular actin bundles and the surrounding extra-cellular matrix or substrate [Abercrombie et al., 1970]. They are transmembrane multi-protein structures that anchor the cell membrane to the substrate and provide a scaffold for the cell. Besides, they are involved in signalling cascades [Schoenwaelder and Burridge, 1999] and are more generally described as the mechanosensory machines of the cell [Geiger and Yamada, 2011; Jansen et al., 2017]. Their formation and functions fall into five steps: initiation, clustering, growth, maturation and disassembly. Although there are other types of adhesions, we focus here on integrin-mediated ones. When integrins (cell-surface adhesion receptors) bind to extra-cellular matrix proteins like fibronectin, they initiate a series of signaling events that lead to contraction of the actin–myosin cytoskeleton, the so-called stress fibers, inside the cell. This cytoskeleton contraction then leads to clustering of integrins at the membrane [Partridge and Marcantonio, 2006] and the transmission of forces enables FAs growth and maturation [Roca-Cusachs et al., 2013]. The stress fibers are attached at one end, or even both ends, to FAs. Under constant tension from their contractile activity, these fibers form a major structuring element of the cell as they support its shape [Svitkina, 2018].

From focal adhesions to motion

Once they are formed, FAs have an essential role as anchoring points that restrain membrane contraction and promote protrusion at the leading edge by regulating actin assembly [Morgan et al., 2007; Geiger et al., 2009]. We can list here two interdependent methods that cooperate to generate a propulsive force at the leading edge. First, FAs help resist actin retrograde flow and thus indirectly boost the force produced by lamellipodial actin polymerization [Alexandrova et al., 2008]. Second, the myosin pulling forces are converted, through FAs, into traction forces against the substrate, hence pulling the cell body forward [Parsons et al., 2010] (see Fig. III.3).

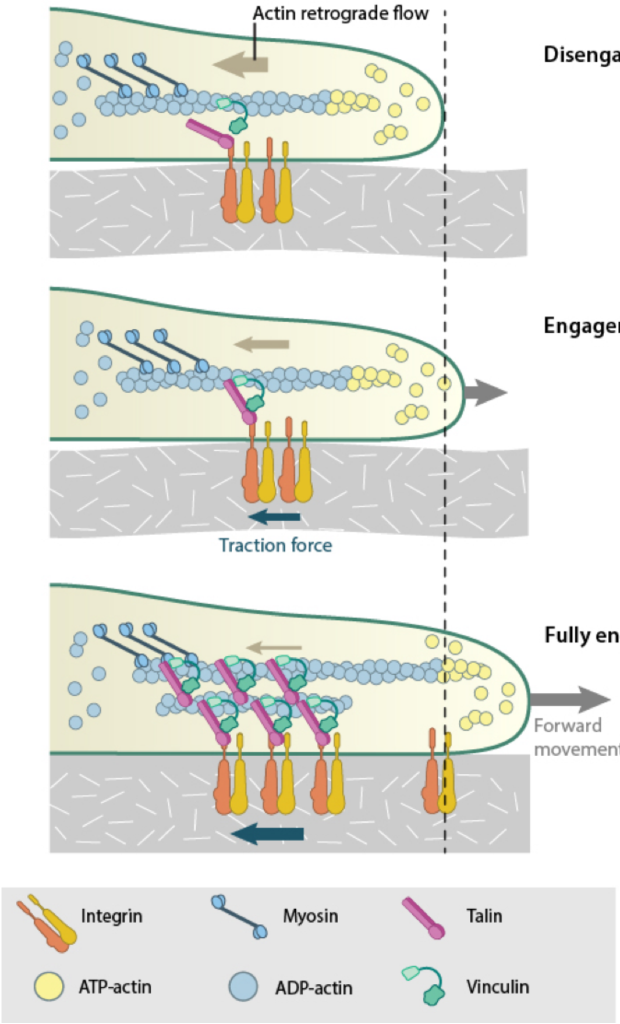

Figure III.3: Illustration of the engagement of the "molecular clutch" when actin filaments connect to integrins to build focal adhesions. Membrane protrusion is encouraged thanks to the resistance provided by FAs against retrograde flow. Besides, myosin-mediated contractile forces are converted to traction forces by the FAs. As the focal adhesions mature, the connection to actin is reinforced and the clutch becomes fully engaged. Image from MBInfo

III.1.4 Existing models of cell spreading on a flat substrate

Cell spreading and adhesion are complex and fascinating phenomena that are a prerequisite for many biological processes, such as cell migration. They are however not completely understood, and in that respect, offer a great field of investigation for modeling. The existing literature focuses on cell spreading on flat substrates. Different sorts of modeling and computational strategies have been developed. The early literature is thoroughly reviewed in [Loosli et al., 2010] and we will focus here on the more recent models. The models can be divided in three main families : analytical, discrete and continuum models.

a Analytical models

Analytical models are a powerful tool to tackle the overall spreading dynamics in various conditions as they do not require extensive computational implementation. On the other hand, they present a strong limitation since they only give global information about the modeled process but cannot provide local ones. The first models aimed at a better comprehension of the dynamics of the cell-substrate adhesion process. Mathematical models were used to describe the evolution of the contact surface [Cuvelier et al., 2007] and to investigate the influence of ligand density gradient on cell spreading kinematics [Sarvestani and Jabbari, 2008]. In later works, the models grew more complex, taking into account active forces from the acto-myosin network such as actin polymerization, kinetics and retrograde flow [Nisenholz et al., 2014] or mechanotransduction feedback from nucleus down to the focal adhesion sites [Cao et al., 2015].

b Discrete models

Discrete models offer a completely different perspective. Indeed, these models are mostly used to represent discrete filaments of the cell's cytoskeleton and to study their evolution and the way they transmit forces. Contrarily to previously cited models, they do not focus on the adhesion process but rather on the internal rearrangement. Tensegrity models, that treat cells as a tensed cytoskeleton network (see Fig. III.4), appear particularly relevant as they can help bridge the gap from molecular processes to mechanical forces [Ingber, 2003].

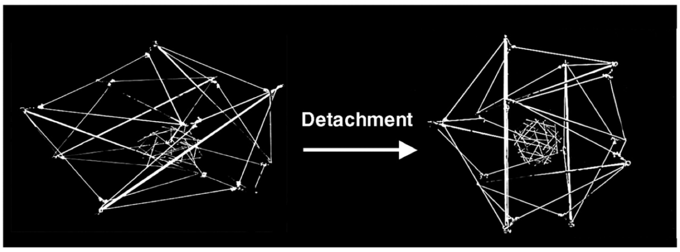

Figure III.4: Tensegrity model of a nucleated cell from a spread state (left) to a detached one (right). The cell model is composed of large beams representing microtubules and thin elastic cords representing microfilaments and intermediate filaments, which carry the tensional forces. Modified from [Ingber, 2003]

In the context of cell spreading, tensegrity has been coupled with divided-media theory to describe the forming of microtubules cytoskeleton from the centrosomes [Maurin et al., 2008]. This coupled approach, also known as the Cytoskeleton Divided Medium (CDM) model was taken further to investigate mechanotransduction during cell spreading with just one type of tensile filaments [Milan et al., 2013]. Recently, a very complete model accounting for actin filament, intermediate filaments and microtubules was proposed allowing to probe local mechanical properties at the sub-cellular level at any time during the adhesion process [Fang and Lai, 2016] and the influence of substrate's curvature was tackled [Vassaux and Milan, 2017].

c Continuum models

Continuum models are the most numerous ones. They offer another way of presenting the cell in 2D or 3D, compared to tensegrity. Indeed, the cell is now considered as a continuum mechanical solid or fluid material in which no organelle is physically represented, with the exception of the nucleus in certain cases. Such models are highly relevant since they account for constant mechanical interactions between all points of the model and provide local as well as global data. They can become even more powerful tools when coupled with additional analytical models [Cao et al., 2015; Roux et al., 2016]. Some studies focus on the first step of the spreading mechanism, modeling receptor-ligand binding, which can only lead to a limited deformation of the cell [Liu et al., 2007; Golestaneh and Nadler, 2016], although the use of membrane reservoirs can influence its extent [Etienne and Duperray, 2011]. Another method consists in modeling spreading mechanism through a unique force accounting both for ligand-receptor binding and for active acto-myosin cytoskeleton tension forces [Zeng and Li, 2011]. It can be used to study more specifically the dynamics of the nucleus during cell spreading [Li et al., 2015]. One work stands out though as it proposes a two-step model [Fan and Li, 2015]: the first spreading step is purely mechanical while, during the second on, actin comes in action at the moving contact line to help the cell spread further.

d Towards models of cell spreading on a structured substrate

While the influence of substrate micro-patterning on cell spreading has been studied and modeled [Albert and Schwarz, 2014], no model has explored the influence of substrate topography on cell spreading for now. As seen in Sec. III.1.1, many questions on the mechanism of cell spreading and nuclear re-positioning on micro-pillars have yet to be answered. A first attempt was made in [Hanson et al., 2015] to answer the question "Is the nucleus being pulled on pushed in pillars grooves ?". The cell is described as a purely elastic square material with a square nucleus within, and the pulling or pushing forces are applied as pressures either on the bottom or on the top of the nucleus, respectively. Although the experimental study is extremely interesting, the model is quite rudimentary but certainly offers preliminary results that are an interesting first taste of what a more complex model could unveil.

III.1.5 Modeling steps for cell spreading on micropillars

We present and explain here the main blocks of our model without getting into the equations yet. These will be further developed in Sec. III.2.4. We choose to use a continuum approach discretized by finite elements, in the continuation of previous work [Allena and Aubry, 2012; Aubry et al., 2014; Deveraux et al., 2017], to model the spreading of a cell and its nucleus mechanics over a substrate structured with micro-pillars. We represent an initially semi-circular suspended 2D cell with its nucleus by a visco-hyperelastic model and consider a condition of symmetry. The cells follows a four step process during which various forces and active strains come into action: the three phases of spreading and an active contractile step. Contrary to the other forces or active strains, the gravitational and contact forces are activated all along the process and are not time-dependent.

1. **Gravity:** the first step is a passive one in which the cell settles on the pillars under the sheer action of gravity.

2. **Repulsive contact force:** As the cell gets in contact with the substrate, it is submitted to a repulsive force from the latter. The contact is modeled, as in Chapter I, by a nonlinear spring along the penetration depth of the cell in the substrate.

3. **Adhesive spreading:** during the third step, the adhesive spreading force comes into action on the portions of the substrate coated with ECM proteins such as fibronectin. As in other works [Zeng and Li, 2011; Fang and Lai, 2016; Fan and Li, 2015], we do not get into the molecular details of spreading, but design a single force accounting for both actin polymerization and formation of adhesion complexes. This non-linear force, attracting the cell towards the substrate, is the novelty of this model. Inspired by the work of [Sauer, 2016], we consider an overlayer surrounding the substrate, in which the spreading force will act on the cell's membrane. Our model only considers the case of a homogeneous fibronectin distribution over the substrate and thus a continuous overlayer.

4. **Active strain:** the last step is the one during which we can test the main question: "Is the nucleus being pushed or pulled down ?". Indeed, intense contractile actin fibers have been observed at two locations in the cell: above the nucleus and around the pillars beneath the nucleus [Davidson et al., 2015; Hanson et al., 2015; Ghibaudo et al., 2011]. The fibers above the nucleus form a dome-like actin structure called the perinuclear actin cap (PAC) [Khatau et al., 2009]. This PAC has three fixation points in the cell : it is anchored at both end to a specific type of FAs and, in the middle, to the nuclear lamina via LINC complex [Maninova

et al., 2017]. The PAC thus form a direct mechanosensing link from the extracellular matrix to the nucleus [Kim et al., 2012] and has been found to be a regulator of cell migration [Kim et al., 2014]. In the model we then define a contractile cable representing the PAC above the nucleus and a contractile radial zone below the nucleus (See Fig. III.5).

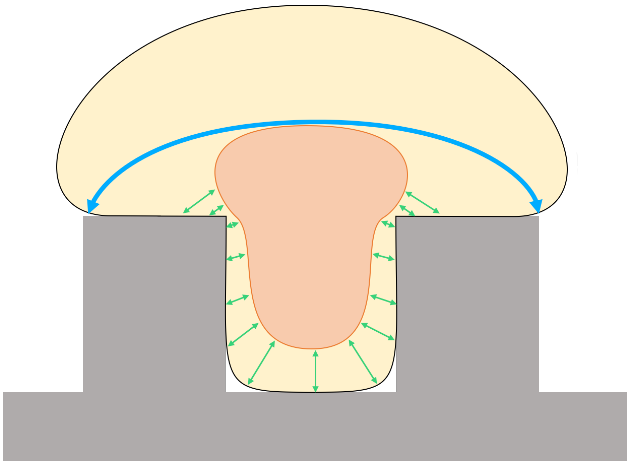

Figure III.5: "Push or pull" hypotheses: the cell nucleus is either pushed through the contraction of the perinuclear actin cap (in blue) or pulled by contractile fibers towards the pillars (in gray).

Compared to previous chapters, this model presents the novelty of a large strain Lagrangian approach that will be developed in Sec. III.2. Besides, this is the first time in this thesis that we introduce an adhesive spreading force since the gravity, contact and active strains all have been treated in the previous chapters. Our model will first be tested on a flat substrate to validate it without the influence of substrate topography. Then, we will test it on a micro-pillared substrate to investigate the mechanism behind nuclear deformation. Eventually, we will show that the gravity indeed plays no role in nuclear deformation [Pan et al., 2012] (setup illustrated in Fig. III.6).

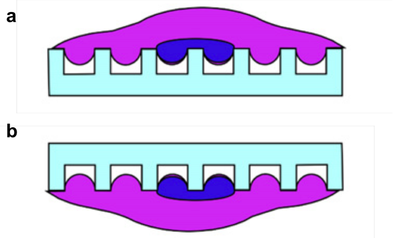

Figure III.6: Experimental process to test the influence of gravity on nuclear deformation during cell spreading: (a) "Control" spreading process, (b) Upside down setup, reversed after the spreading process is complete. Modified from [Pan et al., 2012]

III.2 The model

In this section, we introduce the governing equations of the model. Compared to the previous chapters, we address here directly the large strains of the cell through a Lagrangian approach. Indeed, we achieve extensive cell deformation that we previously tackled through Arbitrary Lagrangian-Eulerian (ALE) method, but wanted to eventually propose a more rigorous approach. We first discuss the dynamics of our model, then the constitutive laws describing the cell. Afterwards, we specify the implementation of active strain through gradient decomposition and the various forces applied to our system. Eventually, we detail the weak form implementation of our equations, which will lead directly to the discretized equations by the FE method.

III.2.1 Geometry and dynamics of the system

We consider the initial configuration of the cell (Ω_{cell}) composed of a nucleus (Ω_n) and a cytoplasm (Ω_{cp}). Besides, we geometrically define the cell membrane (Ω_m). We model only half the cell and use a symmetry boundary condition, described later on, in order to decrease calculation times. To describe Ω_{cell}, Ω_n, Ω_{cp} and Ω_m, we use characteristic functions g_{cell}, g_n, g_{cp} and g_m as described in the Appendix III.A. Then, the global equilibrium of the system in the deformed configuration $\mathbf{x}$ can be written on Ω_{cell} as

$$\mathbf{Div_x}(\boldsymbol{\sigma}_c) + \rho_x \mathbf{g} + \mathbf{f}_v = \rho_x \mathbf{a} \tag{III.1}$$

where $\boldsymbol{\sigma}_c$ is the cell's Cauchy stress, $\mathbf{g}$ the gravity field, $\mathbf{f}_v$ the other volume forces applied to the cell, ρ_x the cell density defined later on and $\mathbf{a}$ the acceleration.

In the large deformation theory, we choose to write the equations in the initial configuration rather than the current one since we do not precisely know the deformed configuration. By the principle of mass conservation, the cell density follows the following relation

$$\rho_x = \frac{\rho_p}{J_c} \tag{III.2}$$

where ρ_x and ρ_p are the cell densities in the current ($\mathbf{x}$) and reference ($\mathbf{p}$) configuration respectively. $\rho_p = \rho_n g_n(\mathbf{p}) + \rho_{cp} g_{cp}(\mathbf{p})$ with ρ_n and ρ_{cp} the densities of the nucleus and cytoplasm, respectively . $J_c = Det(\mathbf{F}_c)$ with $Det(\cdot)$ the determinant operator and $\mathbf{F}_c$ the cell's deformation gradient.

Then, classically, Eq. III.1 can be written in the initial configuration $\mathbf{p}$ as

$$\mathbf{Div_p}(J_c \boldsymbol{\sigma}_c \mathbf{F}_c^{-T}) + \rho_p \mathbf{g} + J_c \mathbf{f}_v = \rho_p \mathbf{a} \tag{III.3}$$

Besides, the second Piola-Kirchhoff stress tensor $\mathbf{S}_c$ can be expressed as

$$\mathbf{S}_c = J_c \mathbf{F}_c^{-1} \boldsymbol{\sigma}_c \mathbf{F}_c^{-T} \tag{III.4}$$

from which the Cauchy stress can be inversely found:

$$\boldsymbol{\sigma}_c = \frac{1}{J_c} \mathbf{F}_c \mathbf{S}_c \mathbf{F}_c^T \tag{III.5}$$

Then, Eq. III.3 reads

$$\mathbf{Div_p}(\mathbf{F}_c \mathbf{S}_c) + \rho_p \mathbf{g} + J_c \mathbf{f}_v = \rho_p \mathbf{a} \tag{III.6}$$

Boundary conditions

Since we model half the cell, we use a symmetry boundary condition on the displacement $\mathbf{u}(-\mathbf{p}) = \mathbf{u}(\mathbf{p})$ on the symmetry axis $\partial\Omega_{sym}$. The boundary conditions of the cell read

$$\boldsymbol{\sigma}_c(\mathbf{n}_{\mathbf{x},c}) dS_\mathbf{x} = \mathbf{f}_{s,\mathbf{x}} dS_\mathbf{x} \tag{III.7}$$

where $\mathbf{n}_{\mathbf{x},c}$ is the outward normal to the cell in the deformed configuration, $dS_\mathbf{x}$ its elementary surface and $\mathbf{f}_{s,\mathbf{x}}$ is the surface forces applied to the cell in the deformed configuration.

The only surface force applying to our system will be the contact force. It will be expressed in further details in Sec. III.2.4, but as a repulsive contact force directed by the normal to the substrate calculated in the deformed configuration $\mathbf{n}_{\mathbf{x},substrate}$, it will be of the form:

$$\mathbf{f}_{s,\mathbf{x}} dS_\mathbf{x} = \|\mathbf{f}_{contact}(\mathbf{x})\| \mathbf{n}_{\mathbf{x},substrate} dS_\mathbf{x} \tag{III.8}$$

where $\|\mathbf{f}_{contact}(\mathbf{x})\|$ is the norm of the contact force that will be defined in Sec. III.2.4.

As we write the equilibrium in the initial configuration, we need to transport the boundary condition in this frame. Working in the Lagragian framework, the normal vectors are to be transported back from the deformed configuration $\mathbf{x}$ to the initial one $\mathbf{p}$ using the cofactor. The normal and area transport is given by the Nanson formula [Gurtin, 1982]:

$$\mathbf{n}_\mathbf{x} dS_\mathbf{x} = J\mathbf{F}^{-T}(\mathbf{n}_\mathbf{p}) dS_\mathbf{p} \tag{III.9}$$

where $\mathbf{n}_\mathbf{x}$ is the normal vector to a surface $\partial\Omega_\mathbf{x}$ of elementary surface area $dS_\mathbf{x}$ in the deformed configuration and $\mathbf{n}_\mathbf{p}$ is the normal vector to a surface $\partial\Omega_\mathbf{p}$ of elementary surface area $dS_{\mathbf{p}}$ in the initial configuration.

Applying this to $\mathbf{n}_{\mathbf{x},substrate}$, we have

$$\mathbf{n}_{\mathbf{x},substrate} dS_{\mathbf{x}} = J_c \mathbf{F}_c^{-T}(\mathbf{n}_{\mathbf{p},substrate}) dS_{\mathbf{p}} \tag{III.10}$$

Then, since $\sigma_c = \frac{1}{J_c}\mathbf{F}_c\mathbf{S}_c\mathbf{F}_c^T$, the three previous equations can we combined and simplified as

$$\mathbf{F}_c\mathbf{S}_c(\mathbf{n}_{\mathbf{p},c}) dS_{\mathbf{p}} = \|\mathbf{f}_c(\mathbf{x})\| J_c \mathbf{F}_c^{-T}(\mathbf{n}_{\mathbf{p},substrate}) dS_{\mathbf{p}} \tag{III.11}$$

Or,

$$\mathbf{F}_c\mathbf{S}_c(\mathbf{n}_{\mathbf{p},c}) dS_{\mathbf{p}} = \mathbf{f}_{s,\mathbf{p}} dS_{\mathbf{p}} \tag{III.12}$$

where $\mathbf{f}_{s,\mathbf{p}} = \|\mathbf{f}_{contact}(\mathbf{x})\| J_c \mathbf{F}_c^{-T}(\mathbf{n}_{\mathbf{p},substrate})$ is the surface force in the initial configuration.

We now have the equilibrium and the boundary conditions of the system in the Lagrangian configuration. To implement a model, we need to work on the constitutive laws describing the internal behaviour of the cell.

III.2.2 Constitutive laws of the cell

We describe the cell as an overall visco-hyperelastic material composed of a solid and a fluid part in parallel. Indeed, we can say that the cell is a composite of organelles, proteins and various molecules surrounded by interstitial fluid. As such, we consider that both the fluid and the solid parts have equal participation to the overall stress while they undergo the same deformation. The elastic part is described as a Mooney-Rivlin material, while the viscous part is described through a fluid formulation. The problem of visco-elastic solids in the large deformations framework is an ongoing topic in material science, but has not been tackled often in biological materials. The approach we choose, equivalent to a generalized Maxwell model, has already been used to describe the visco-elastic behaviour of spine ligaments [Jiang et al., 2015]. As such, we can write

$$\begin{aligned} \mathbf{S}_c &= \mathbf{S}_s + \mathbf{S}_f \\ \mathbf{F}_c &= \mathbf{F}_s = \mathbf{F}_f \end{aligned} \tag{III.13}$$

where the subscripts c, s and f respectively designate the cell, the solid and the fluid part.

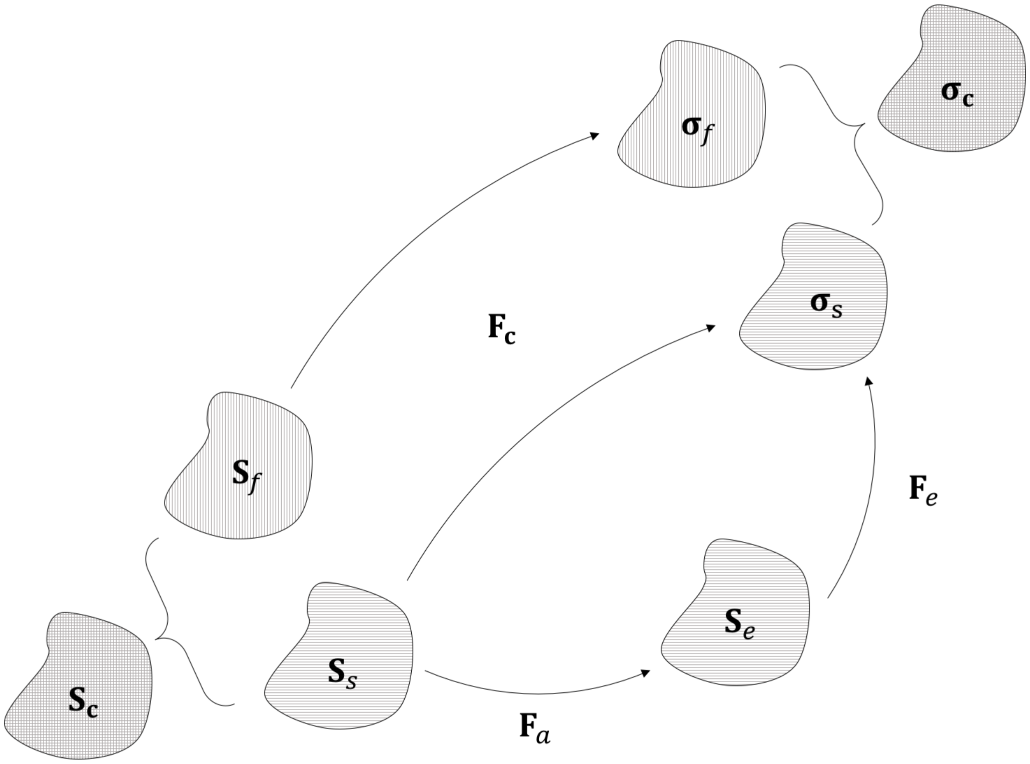

Figure III.7: Illustration of the material model and relationship between the configurations.

a The solid phase

When describing an elastic material in the large strain regime, a fundamental mathematical requirement for its strain energy function Ψ to be admissible is to be polyconvex, i.e. convex with respect to the three invariants [Itskov and Aksel, 2004; Bonet et al., 2015]. In the general case of an isotropic material for which we do not use any subscript, Ψ must be a function of the invariants of of the symmetric right Cauchy-Green tensor $\mathbf{C}$, I_1, I_2 and I_3 :

$$\Psi = W(I_1, I_2, I_3) \tag{III.14}$$

where the invariants are defined as follows [Holzapfel, 2000; Bonet and Wood, 1997]

$$\begin{aligned} I_1 &= Tr(\mathbf{C}) \\ I_2 &= det(\mathbf{C})\, Tr(\mathbf{C}^{-1}) = |cof(\mathbf{F})|^2 \\ I_3 &= det(\mathbf{C}) = J^2 \end{aligned} \tag{III.15}$$

with $|cof(\mathbf{F})|$ the norm of the cofactor of $\mathbf{F}$, defined as $cof(\mathbf{F}) = J\mathbf{F}^{-T}$ as long as $\mathbf{F}$ is invertible.

Let us now see how the three invariants I_1, I_2 and I_3 can be linked to the variations of length, surface and volume of the system, respectively.

First invariant

The transport of a vector from the initial to the deformed configuration is done through the deformation gradient tensor as $d\mathbf{x} = \mathbf{F}(d\mathbf{p})$. Then, if we want to know the elongation, we use the norm $\|d\mathbf{x}\|$ as

$$\begin{aligned} \|d\mathbf{x}\|^2 &= (d\mathbf{x}, d\mathbf{x}) \\ &= (\mathbf{F}(d\mathbf{p}), \mathbf{F}(d\mathbf{p})) \\ &= (\mathbf{C}(d\mathbf{p}), d\mathbf{p}) \end{aligned} \tag{III.16}$$

with $(,)$ the dot product operator. If we choose the first direction $d\mathbf{p} = \mathbf{i}_1$, then $\|d\mathbf{x}\|_1^2 = C_{11}$. Summing the result in all three directions, we get the sum of the square of the elongations in all three directions.

Besides, the first invariant reads

$$I_1 = Tr(\mathbf{C}) = \sum_{n=1}^{3} C_{ii} = \sum_{n=1}^{3} \left(\frac{d\mathbf{x}}{d\mathbf{p}}\right)_i^2 \tag{III.17}$$

where $\left(\frac{d\mathbf{x}}{d\mathbf{p}}\right)_i$ describes the length variation with respect to the initial configuration in the i-th direction.

I_1 then describes the sum of the squared length variations of the system in the three directions.

Second invariant

The second invariant reads $I_2 = |cof(\mathbf{F})|^2 = Tr(cof(\mathbf{F})cof(\mathbf{F})^T)$ since the norm of a matrix $\mathbf{A}$ is defined by $|\mathbf{A}|^2 = Tr(\mathbf{A}\mathbf{A}^T)$. As seen in Eq. III.9, the normal vectors are transported from the current to the initial configuration through the relationship

$$\mathbf{n_x} dS_\mathbf{x} = cof(\mathbf{F})(\mathbf{n_p}) dS_\mathbf{p} \tag{III.18}$$

Taking the squared norm of both sides of this equation, we get:

$$\begin{aligned} dS_\mathbf{x}^2 &= (cof(\mathbf{F})(\mathbf{n_p}), cof(\mathbf{F})(\mathbf{n_p}))dS_\mathbf{p}^2 \\ &= (cof(\mathbf{F})^T cof(\mathbf{F})(\mathbf{n_p}), \mathbf{n_p})dS_\mathbf{p}^2 \end{aligned} \tag{III.19}$$

For all orientations $\mathbf{n_p}$ I_2 then gives the maximum area deformation of the system.

Third invariant

The third invariant reads $I_3 = J^2 = (det(\mathbf{F}))^2$. If we take an elementary volume $d\Omega_\mathbf{x}$ in the deformed configuration and its corresponding volume in the initial configuration $d\Omega_\mathbf{p}$, we can write

$$d\Omega_{\mathbf{x}} = det(\mathbf{F}) d\Omega_{\mathbf{p}} \tag{III.20}$$

I_3 then describes the volume variations of the system. Consequently, the three invariants control the three limit situations in which a subdomain becomes very long or thin, extended or flat and local reversing of the volume.

In models describing the cell as a solid continuum, three levels of constitutive laws can be found:

1. Standard Saint-Venant meterials, depending on the first invariant only [Allena and Aubry, 2012; Fan and Li, 2015]
2. Neo-Hookean materials, based on a dependency on the first and third invariants, thus taking control of the volume variations [Jean et al., 2003; Mokbel et al., 2017]
3. Polyconvex Mooney-Rivlin materials, that control the surfaces evolution as well [Zeng and Li, 2011; Wang et al., 2017].

In a biomaterial, there can be extensive deformations along lines, surfaces and volumes. It is thus important to use a constitutive model which handles these three aspects. Moreover, to get a mathematically stable model, we choose to implement a Mooney-Rivlin material. Because of the extremely large deformations encountered in the simulation, this model is able to prevent elements reversal thanks to the energy depending on the volume invariant. The total energy W_{MR} of an elastic Mooney-Rivlin model can be written as

$$W_{MR}(\mathbf{C}) = \alpha I_1(\mathbf{C}) + \beta I_2(\mathbf{C}) + \Gamma(I_3(\mathbf{C})) \tag{III.21}$$

where α and β are positive material parameters, and Γ is a convex function of J. To go from the strain energy to the second Piola-Kirchhoff tensor, we write, accordingly to the classical thermodynamics equation of hyperelastic materials,

$$\mathbf{S} = 2\frac{\partial W_{MR}}{\partial \mathbf{C}} \tag{III.22}$$

Thus, for our hyperelastic material, we obtain

$$\mathbf{S} = 2\alpha \mathbf{I} + 2\beta(I_2\mathbf{C}^{-1} - I_3\mathbf{C}^{-2}) + \Gamma'(J) J\mathbf{C}^{-1} \tag{III.23}$$

with $\Gamma'(J)$ the derivative of the function Γ with respect to J. The Cayley-Hamilton theorem allows use to write

$$\mathbf{C}^3 - I_1\mathbf{C}^2 + I_2\mathbf{C} - I_3\mathbf{I} = 0 \tag{III.24}$$

from which we can get $\mathbf{C}^{-2}$ and simplify Eq. III.23:

$$\mathbf{S} = 2(\alpha + \beta I_1)\mathbf{I} - 2\beta\mathbf{C} + \Gamma'(J)J\mathbf{C}^{-1} \tag{III.25}$$

As stated before, the function Γ is a convex function with respect to J and must be chosen to fulfill the condition of vanishing Piola-Kirchhoff II energy at the initial configuration. We use the expression from [Fried and Johnson, 1988] where

$$\Gamma(J) = \frac{\lambda_{MR}}{2}(ln(J))^2 - 3\alpha J^{2/3} - 3\beta J^{4/3} \tag{III.26}$$

where λ_{MR} is a bulk modulus.

In this case, the strain energy function reads

$$W_{MR} = \alpha(I_1 - 3I_3^{1/3}) + \beta(I_2 - 3I_3^{2/3}) + \frac{\lambda_{MR}}{2}(ln(J))^2 \tag{III.27}$$

The function $w = \frac{\lambda_{MR}}{2}(ln(J))^2$ is a dilatoric contribution representing the energy stored in compression. The second Piola-Kirchhoff stress thus reads

$$\mathbf{S} = 2(\alpha + \beta Tr(\mathbf{C}))\mathbf{I} - 2\beta\mathbf{C} + (\lambda_{MR} ln(J) - 2\alpha J^{2/3} - 4\beta J^{4/3})\mathbf{C}^{-1} \tag{III.28}$$

In this configuration, we can easily verify that, in the initial configuration, $\mathbf{S}(0) = \mathbf{0}$ since $\mathbf{C}(0) = I$, $Tr(\mathbf{C}(0)) = 3$ and $J(0) = 1$. Then, following [Bonet et al., 2015], the material parameters α, β and λ_{MR} can be related to the classical Lamé parameters μ_e and λ_e in linearized elasticity through

$$\begin{aligned} \alpha + \beta &= \frac{\mu_e}{2} \\ \lambda_{MR} &= \lambda_e + \frac{2}{3}\mu_e \end{aligned} \tag{III.29}$$

We choose $\beta = 0.2\frac{\mu_e}{2}$ in order to solve this system, and μ_e and λ_e are the Lamé coefficient of the cell, defined as

$$\begin{aligned} \lambda_e &= \frac{E_c \nu_c}{(1+\nu_c)(1-2\nu_c)} \\ \mu_e &= \frac{E_c}{2(1+\nu_c)} \end{aligned} \tag{III.30}$$

where E_c and ν_c are the cell's Young modulus and Poisson's ratio, respectively.

As in previous works in various biomechanics fields [Rodriguez et al., 1994; Taber, 1995; Lubarda, 2004; Munoz et al., 2007; Goktepe et al., 2010; Golestaneh and Nadler, 2016; Deveraux et al., 2017], we model the cell active contractility (as represented in Fig. III.5) as an active strain through the decomposition of the deformation gradient tensor $\mathbf{F}_c$ as follows:

$$\mathbf{F}_c = \mathbf{F}_e\mathbf{F}_a \tag{III.31}$$

with $\mathbf{F}_e$ and $\mathbf{F}_a$ the elastic and active deformation gradient tensors, respectively. Thus, $\mathbf{F}_e = \mathbf{F}_c\mathbf{F}_a^{-1}$. Once we know $\mathbf{F}_e$, we can deduce $\mathbf{C}_e$ and J_e.

The total stress $\mathbf{S}_s$ from the solid part then reads

$$\mathbf{S}_s = J_a\mathbf{F}_a^{-1}\mathbf{S}_e\mathbf{F}_a^{-T} \tag{III.32}$$

Where $\mathbf{S}_e$ is of the form described in Eq. III.28 as:

$$\mathbf{S}_e = 2(\alpha + \beta Tr(\mathbf{C}_e))\mathbf{I} - 2\beta\mathbf{C}_e + (\lambda_{MR} ln(J_e) - 2\alpha J_e^{2/3} - 4\beta J_e^{4/3})\mathbf{C}_e^{-1} \tag{III.33}$$

The expression of the active deformation gradient tensor will be given in Sec. III.2.4.

b The fluid phase

For our material to be visco-hyperelastic, we add a fluid stress as the second Piola-Kirchhoff stress tensor $\mathbf{S}_f$. We start with the classical Newtonian viscous fluid behaviour in the Eulerian configuration and the fluid Cauchy stress $\boldsymbol{\sigma}_f$ reads

$$\boldsymbol{\sigma}_f = \lambda_f Tr(\mathbf{D}_f)\mathbf{I} + 2\mu_f\mathbf{D}_f \tag{III.34}$$

where λ_f and μ_f are the viscous Lamé coefficients, and $\mathbf{D}_f$ is the Eulerian cell's rate of deformation gradient defined as $\mathbf{D}_f = \frac{1}{2}(\mathbf{D_x v} + \mathbf{D_x v}^T)$ with $\mathbf{v}$ the velocity.

To ensure compatibility with the solid description, we compute this expression with respect to the Lagrangian coordinates in the reference configuration as:

$$\mathbf{D}_f = \frac{1}{2}(\mathbf{D_p v}\,\mathbf{F}_f^{-1} + \mathbf{F}_f^{-T}\mathbf{D_p v}^T) = \frac{1}{2}\left(\frac{d\mathbf{F}_f}{dt}\mathbf{F}_f^{-1} + \mathbf{F}_f^{-T}\frac{d\mathbf{F}_f^T}{dt}\right) \tag{III.35}$$

As $\mathbf{C}_f = \mathbf{F}_f^T\mathbf{F}_f$, then

$$\frac{d\mathbf{C}_f}{dt} = \mathbf{F}_f^T\frac{d\mathbf{F}_f}{dt} + \frac{d\mathbf{F}_f^T}{dt}\mathbf{F}_f \tag{III.36}$$

As a result,

$$\mathbf{F}_f^{-T}\frac{d\mathbf{C}_f}{dt}\mathbf{F}_f^{-1} = 2\mathbf{D}_f \tag{III.37}$$

As written in the previous section, and since $\mathbf{F}_f = \mathbf{F}_c$, we can write

$$\mathbf{S}_f = J_c\mathbf{F}_c^{-1}\boldsymbol{\sigma}_f\mathbf{F}_c^{-T} \tag{III.38}$$

Then, by substituting the expressions of $\boldsymbol{\sigma}_f$ and $\mathbf{D}_f$ in the previous equation, we obtain

$$\mathbf{S}_f = \frac{J_c\lambda_f}{2} Tr\left(\mathbf{F}_c^{-T}\frac{d\mathbf{C}_c}{dt}\mathbf{F}_c^{-1}\right)\mathbf{C}_c^{-1} + J_c\mu_f\mathbf{C}_c^{-1}\frac{d\mathbf{C}_c}{dt}\mathbf{C}_c^{-1} \tag{III.39}$$

Yet,

$$\frac{d\mathbf{C}_c^{-1}}{dt} = -\mathbf{C}_c^{-1}\frac{d\mathbf{C}_c}{dt}\mathbf{C}_c^{-1} \tag{III.40}$$

Hence, by commutativity of the trace operator, $\mathbf{S}_f$ can be written as

$$\mathbf{S}_f = \frac{J_c\lambda_f}{2} Tr(\mathbf{C}_c^{-1}\frac{d\mathbf{C}_c}{dt})\mathbf{C}_c^{-1} - J_c\mu_f\frac{d\mathbf{C}_c^{-1}}{dt} \tag{III.41}$$

III.2.3 Weak form implementation

We use a classic finite elements approximation to obtain the displacement field $\mathbf{u}$ by developing a weak form for Eq. III.6. To do so, we multiply the whole equation by $\mathbf{w}$ representing any kinematically admissible displacement test function and we integrate it on Ω_{cell}. These equations are written in the initial configuration $\Omega_{cell,p}$ of surface $\partial\Omega_{cell,p}$ and elementary surface and volume $dS_\mathbf{p}$ and $dV_\mathbf{p}$.

$$\int_{\Omega_{cell,\mathbf{p}}} (\mathbf{Div_p}(\mathbf{F}_c\mathbf{S}_c),\mathbf{w})dV_\mathbf{p} + \int_{\Omega_{cell,\mathbf{p}}} [(\rho_p\mathbf{g} + J_c\mathbf{f}_v - \rho_p\mathbf{a},\mathbf{w})]dV_\mathbf{p} = 0 \tag{III.42}$$

Through algebraic manipulations, for any matrix $\mathbf{A}$ and vector $\mathbf{a}$, we have

$$div_\mathbf{p}(\mathbf{A}^T(\mathbf{a})) = (\mathbf{Div_p}(\mathbf{A}),\mathbf{a}) + Tr(\mathbf{A}(\mathbf{D_p}\mathbf{a})^T) \tag{III.43}$$

Besides, the Stokes theorem states that, on a domain Ω with a boundary $\partial\Omega$ of outward normal $\mathbf{n}$,

$$\int_\Omega div(\mathbf{A}^T(\mathbf{a}))dV = \int_{\partial\Omega}(\mathbf{A}^T(\mathbf{a}),\mathbf{n})dS = \int_{\partial\Omega}(\mathbf{a},\mathbf{A}(\mathbf{n}))dS \tag{III.44}$$

Plugging Eq. III.44 in Eq. III.43, it can be written as

$$\int_\Omega(\mathbf{Div_p}(\mathbf{A}),\mathbf{a})dV = -\int_\Omega Tr(\mathbf{A}(\mathbf{D_p}\mathbf{a})^T)dV + \int_{\partial\Omega}(\mathbf{a},\mathbf{A}(\mathbf{n}))dS \tag{III.45}$$

and applying this last equality to Eq. III.42, with $\mathbf{A} = \mathbf{F}_c\mathbf{S}_c$ and $\mathbf{a} = \mathbf{w}$, we obtain

$$\int_{\Omega_{cell,\mathbf{p}}} (\mathbf{Div_p}(\mathbf{F}_c\mathbf{S}_c),\mathbf{w})dV_\mathbf{p} = -\int_{\Omega_{cell,\mathbf{p}}} Tr(\mathbf{F}_c\mathbf{S}_c(\mathbf{D_p}\mathbf{w})^T)dV_\mathbf{p} + \int_{\partial\Omega_{cell,\mathbf{p}}} (\mathbf{w},\mathbf{F}_c\mathbf{S}_c(\mathbf{n}_{\mathbf{p},c}))dS_\mathbf{p} \tag{III.46}$$

Hence, the weak form of the equilibrium equation reads

$$\begin{aligned} & -\int_{\Omega_{cell,\mathbf{p}}} Tr(\mathbf{F}_c\mathbf{S}_c(\mathbf{D_p w})^T)dV_{\mathbf{p}} + \int_{\partial\Omega_{cell,\mathbf{p}}} (\mathbf{w},\mathbf{F}_c\mathbf{S}_c(\mathbf{n}_{\mathbf{p},c}))dS_{\mathbf{p}} \\ & + \int_{\Omega_{cell,\mathbf{p}}} [(\rho_p\mathbf{g}+J_c\mathbf{f}_v-\rho_p\mathbf{a},\mathbf{w})]dV_{\mathbf{p}} = 0 \end{aligned} \tag{III.47}$$

In Eq. III.47, the first integral represents the stresses inside the system, and the third one directly represents the body forces applied to the cell. As demonstrated in Eq. III.12, the second integral represents the boundary condition of our system: the contact force. As such, we can write

$$-\int_{\Omega_{cell,\mathbf{p}}} Tr(\mathbf{F}_c\mathbf{S}_c(\mathbf{D_p w})^T)dV_{\mathbf{p}} + \int_{\partial\Omega_{cell,\mathbf{p}}} (\mathbf{w},\mathbf{f}_{s,\mathbf{p}})dS_{\mathbf{p}} + \int_{\Omega_{cell,\mathbf{p}}} [(\rho_p\mathbf{g}+J_c\mathbf{f}_v-\rho_p\mathbf{a},\mathbf{w})]dV_{\mathbf{p}} = 0 \tag{III.48}$$

Numerical implementation in a finite elements software

As we implement our model, the contact force is not applied as a surface force but as a body force. However, the amplitude of the repulsive contact force is chosen so that the interpenetration depth between the cell and the substrate is small. Let us demonstrate that, in such case, we can approximate the surface integral by a thick integral that we write in volume.

In the vicinity of the contact boundary we can parametrize it as a shell. We can then use a set of parameters linked to the curved plane, namely ξ_1, ξ_2 and ζ as:

$$\mathbf{p}(\xi_1,\xi_2,\zeta) = \mathbf{p}_s(\xi_1,\xi_2) + \zeta\mathbf{n_p}(\xi_1,\xi_2) \tag{III.49}$$

where $\mathbf{p}(\xi_1,\xi_2,\zeta)$ is the position vector in the initial configuration, $\mathbf{p}_s$ corresponds to the coordinates in the curved plane and $\mathbf{n_p}$ is the normal to such plane (see Fig. III.8).

Then, for a given function $\gamma(\mathbf{p})$ to be integrated on a volume Ω_p, we change variables as

$$\int_{\Omega_p} \gamma(\mathbf{p})dV_p = \int_{\Omega_\xi} \gamma(\mathbf{p}(\xi_1,\xi_2,\zeta))J_\xi(\xi_1,\xi_2,\zeta)d\xi_1 d\xi_2 d\zeta \tag{III.50}$$

Yet, because of the definition of the unit normals and the chosen parametrization:

$$J_\xi = det(\mathbf{F}_\xi) = det\left[\frac{d\mathbf{p}}{d\xi_1},\frac{d\mathbf{p}}{d\xi_2},\mathbf{n_p}\right] = \left(\frac{d\mathbf{p}}{d\xi_1}\wedge\frac{d\mathbf{p}}{d\xi_2},\mathbf{n_p}\right) = \left|\frac{d\mathbf{p}}{d\xi_1}\wedge\frac{d\mathbf{p}}{d\xi_2}\right| \tag{III.51}$$

Then,

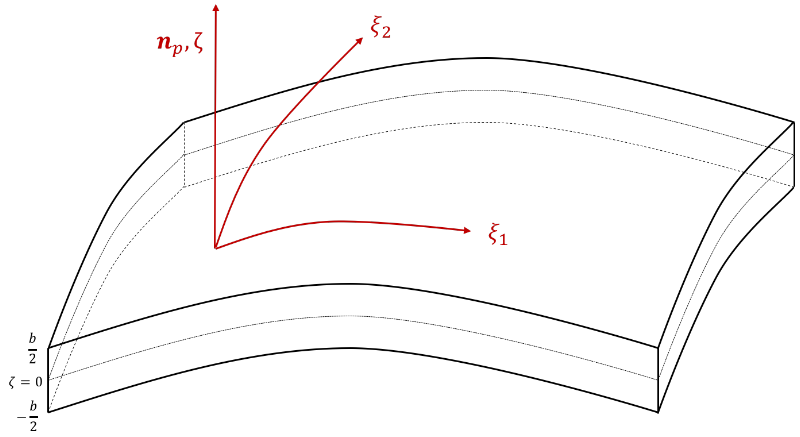

Figure III.8: Parametrization of the variables for a curved surface.

$$\int_{\Omega_p} \gamma(\mathbf{p}) dV_p = \int_{\Omega_\xi} \gamma(\mathbf{p}(\xi_1,\xi_2,\zeta)) \left| \frac{d\mathbf{p}}{d\xi_1} \wedge \frac{d\mathbf{p}}{d\xi_2} \right| d\xi_1 d\xi_2 d\zeta \tag{III.52}$$

If we suppose that the thickness of our overlapping volume is small, we can approximate it by a constant b and write the integral as:

$$\begin{aligned} \int_{\Omega_p} \gamma(\mathbf{p}) dV_p &\approx \int_{-b/2}^{b/2} d\zeta \int_{S_\xi} \gamma(\mathbf{p}(\xi_1,\xi_2,0)) \left| \frac{d\mathbf{p}}{d\xi_1} \wedge \frac{d\mathbf{p}}{d\xi_2} \right|_{\zeta=0} d\xi_1 d\xi_2 \\ &\approx b \int_{S_\xi} \gamma(\mathbf{p}(\xi_1,\xi_2,0)) \left| \frac{d\mathbf{p}}{d\xi_1} \wedge \frac{d\mathbf{p}}{d\xi_2} \right|_{\zeta=0} d\xi_1 d\xi_2 \end{aligned} \tag{III.53}$$

Besides, if we integrate the same function on the surface S_p where $\zeta = 0$, we have

$$\int_{S_p} \gamma(\mathbf{p}) dS_p = \int_{S_\xi} \gamma(\mathbf{p}(\xi_1,\xi_2,0)) \left| \frac{d\mathbf{p}}{d\xi_1} \wedge \frac{d\mathbf{p}}{d\xi_2} \right|_{\zeta=0} d\xi_1 d\xi_2 \tag{III.54}$$

Plugging Eq.III.54 in Eq.III.53, we obtain

$$\int_{\Omega_p} \gamma(\mathbf{p}) dV_p \approx b \int_{S_p} \gamma(\mathbf{p}) dS_p \tag{III.55}$$

Thus, if we take $\gamma(\mathbf{p}) = \mathbf{f}_{s,\mathbf{p}}$, we can write

$$\int_{\partial\Omega_{cell,\mathbf{p}}} (\mathbf{w}, \mathbf{f}_{s,\mathbf{p}}) dS_\mathbf{p} \approx \int_{\Omega_{cell,\mathbf{p}}} (\mathbf{w}, \mathbf{f}_{s\to v}) dV_\mathbf{p} \tag{III.56}$$

with $\mathbf{f}_{s\to v} = b\mathbf{f}_{s,\mathbf{p}}$ the volume average of the surface force over a thickness b which can be interpreted as the penalization depth of the contact.

Eventually, the weak form of the equilibrium equation that we implement is

$$-\int_{\Omega_{cell,\mathbf{p}}} Tr(\mathbf{S}_c(\mathbf{D}_{\mathbf{p}}\mathbf{w}\,\mathbf{F}_c)^T)\,dV_{\mathbf{p}} + \int_{\Omega_{cell,\mathbf{p}}} [(\rho_p\mathbf{g} + \mathbf{f}_{s\to v} + J_c\mathbf{f}_v - \rho_p\mathbf{a}, \mathbf{w})]\,dV_{\mathbf{p}} = 0 \quad \text{(III.57)}$$

In order to solve this problem, we directly implement Eq. III.57 in the finite elements (FE) software COMSOL Multiphysics ©. The principle is to discretize this equation both in space and in time. The discretization in space is achieved through quadratic functions over a mesh composed of nodes and elements. For the discretization in time, we use a second order backwards differentiation formula (BDF). In order to compute the solution, we use a highly nonlinear Newton method as our iterative algorithm.

III.2.4 Description of the modeled system and the forces in action

Through interactions with its environment, the cell is subject to forces in reactions to these chemo-mechanical cues. We review here the steps of the process presented in Sec. III.1.5 with a numerical point of view. The simulation is divided in four consecutive phases in which forces are applied progressively as smooth functions of time to ensure numerical convergence (see Fig. III.9 and Appendix III.D). We choose two study cases: the first one with a flat substrate, and the second one with a micro-pillared substrate.

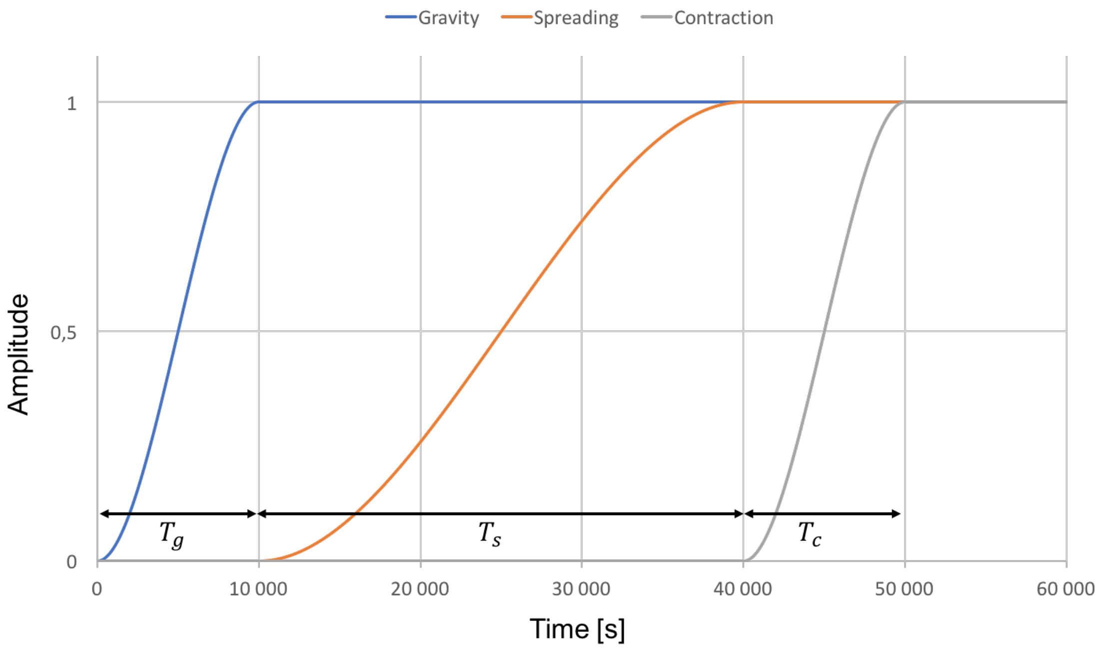

Figure III.9: Graphical representation of the successive phases of the simulation. In blue $h_g(t)$, in orange $h_{spread}(t)$ and in grey $h_{cont}(t)$ with their duration time T_g, T_s and T_c, respectively.

1. **Gravity**: First, the gravity $\rho_p \mathbf{g}$ is applied and the cell settles on the pillars.
2. **Repulsive contact force**: As the cell comes in contact with the substrate, a repulsive force $\mathbf{f}_{contact}$ from the substrate $g_{substrate}$ (defined in Appendix III.B) on the cell comes into play.
3. **Spreading**: Then, the cell is attracted towards the substrate through the adhesive spreading force $\mathbf{f}_{spread}$ active in the overlayer g_{layer} or $g_{ground,flat,layer}$ for the micro-pillared and the flat substrate, respectively, defined In Appendix III.B.
4. **Contraction**: Last, the contractile active strain, defined through $\mathbf{F}_a$, activates. Depending on the chosen scenario, either the PAC, the bottom or both zones contract. The active domains g_{PAC} and g_{bottom} are defined in Appendix III.C.

a Gravity

The gravity is applied through a function $h_g(t)$ in a time T_g. Then, we have

$$\rho_p \mathbf{g} = -\rho_p h_g(t) g \mathbf{i}_y \tag{III.58}$$

with g the gravitational acceleration and $\mathbf{i}_y$ the vertical direction vector.

b Repulsive contact force

This contact is modeled as a surface force, that is approximated to a body force. As in Chapter I, the contact between the cell and the micro-structured substrate is modeled through a normal repulsive force from the substrate. It behaves as non-linear spring defined through the levelset of the cell intersecting with the one of the substrate. As described in [Graveleau et al., 2015], the approach has the great advantage to define a precise contact zone without mesh constraints.

When the cell is not in contact with the substrate, its boundaries are free, so the norm of the contact force reads $\|\mathbf{f}_{contact}(\mathbf{x})\| = 0$. When the cell is in contact with the substrate, the norm of the surface contact force in the deformed configuration reads

$$\|\mathbf{f}_{contact}(\mathbf{x})\| = \mu_{contact} g_{substrate}(\mathbf{x}) \tag{III.59}$$

where $\mu_{contact}$ is the penalization coefficient and $g_{substrate} = g_{pillars} + g_{ground}$ is a characteristic function that varies non-linearly between 0 and 1 on a given interpenetration depth equal to 0.5 μm (see Appendix III.B). This depth can be adjusted by varying the scaling parameter of the regularized Heaviside function. In the case of a flat substrate, we have $g_{substrate} = g_{ground,flat}$. Fig. III.10 shows the interpenetration area between the cell and the substrate during contact. We see here nicely that, the

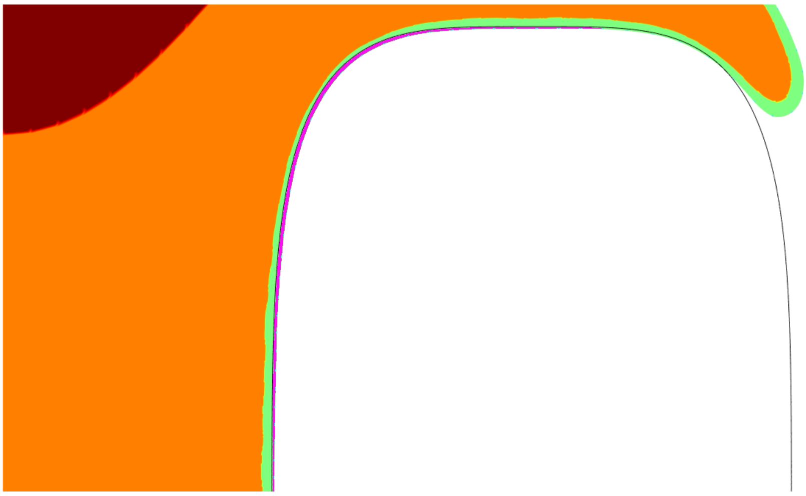

Figure III.10: Interpenetration depth (in magenta) of the contact between the cell and the pillars (black line) during the simulation

approximation of a surface force integral by a volume one (see Eq. III.56) is reasonable due to the narrowness of such volume.

c Adhesive spreading force

We choose to model cell spreading through a local attractive force $\mathbf{f}_{spread}$ from the pillars to the cell. Adhesion is a tricky problem to model in finite elements and different strategies can be adopted [Sauer, 2016]. We create a layer surrounding the substrate, where the adhesion process will take place (see Fig. III.11 and Appendix III.B). The spreading force is modeled as a volume force so, in Eq. III.48, $\mathbf{f}_v = \mathbf{f}_{spread}$.

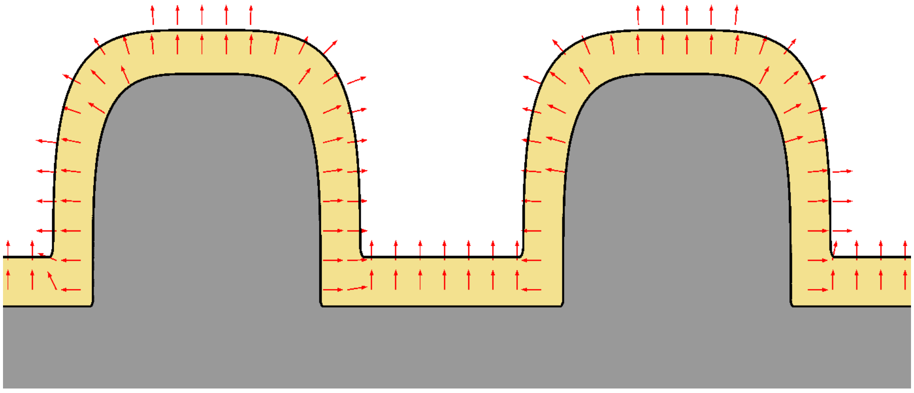

Figure III.11: Illustration of the adhesive layer (yellow) over the substrate (gray) in the case of the micro-pillared substrate.

The novelty of this model lies in the superposition of a repulsive contact force and an adhesive spreading one. Indeed, the cell needs to be attracted towards the substrate but must not penetrate into the substrate. Thus, the substrate levelsets are used to define the repulsive contact force, as defined in the previous paragraph, while a layer surrounding the pillars and substrate is built (g_{layer} or $g_{ground,flat,layer}$ in the case of the flat substrate), in which the spreading force will be activated. This force is radial to the cell (see Fig. III.12) and accounts for actin polymerization at the cell membrane, as well as the formation of adhesion complexes between the cell and its environment. It is defined in the cell membrane as

$$\mathbf{f}_{spread}(\mathbf{p}) = \mu_{spread}(\mathbf{p}, t)\, g_{m,layer}(\mathbf{p}+\mathbf{u})\, h_{spread}(t)\, J_c \mathbf{F}_c^{-T} \mathbf{n}_{\mathbf{p},c} \tag{III.60}$$

where μ_{spread} is the spreading coefficient, and $\mathbf{n}_{\mathbf{p},c}$ is the outward normal to the cell is the initial configuration. This normal is computed at the cell boundary, but it is easily extended inside the cell membrane through the gradient of the membrane levelset function g_m. $g_{m,layer} = g_{layer} \cap g_m$ for the micro-pillared substrate, and $g_{m,layer} = g_{ground,flat,layer} \cap g_m$ for the flat substrate. Eventually, h_{spread} is the time-dependent function that regulates the dynamics of the spreading force (see Fig. III.9).

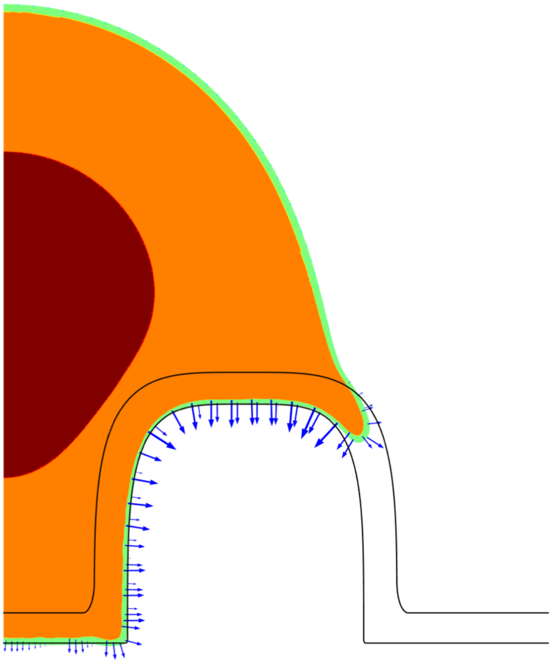

Figure III.12: Illustration image of $\mathbf{f}_{spread}$ (blue arrows), directed radially, thus effectively spreading the cell over the substrate and creating an adhesion.

By recruitment of scaffolding and signaling components, focal adhesions maturate and thus get stronger with time [Geiger et al., 2009]. The spreading coefficient is governed by a partial differential equation (PDE) so it will start increasing only when the membrane penetrates the adhesive layer and reach a plateau when it attains a maximum value. This is done to describe the maturation of FAs. The governing equation then reads:

$$\frac{\partial \mu_{spread}(\mathbf{p}+\mathbf{u},t)}{\partial t} = \begin{cases} v_{spread,0}\, g_{layer}(\mathbf{p}+\mathbf{u}) \text{ if } \mu_{spread} < \mu_{spread,max} \\ 0 \text{ otherwise} \end{cases} \tag{III.61}$$

where $v_{spread,0}$ is the maturation velocity and $\mu_{spread,max}$ is the maximum value of μ_{spread} allowed, reached when the adhesions are in their mature state.

d Active deformation

The active mechanism of cell spreading on a micro-structured substrate is not well understood. As such, different hypotheses can be made and could be tested on our model. An actin cap has been observed above the nucleus, as well as concentration of actin around the pillars where the cell is adhered. We thus model two regions where active strains occur : the PAC g_{PAC} above the nucleus, and a radial portion of the cytoplasm g_{bottom} which will be in contact with the substrate after spreading (see Fig. III.13). Both areas are defined in Appendix III.C.

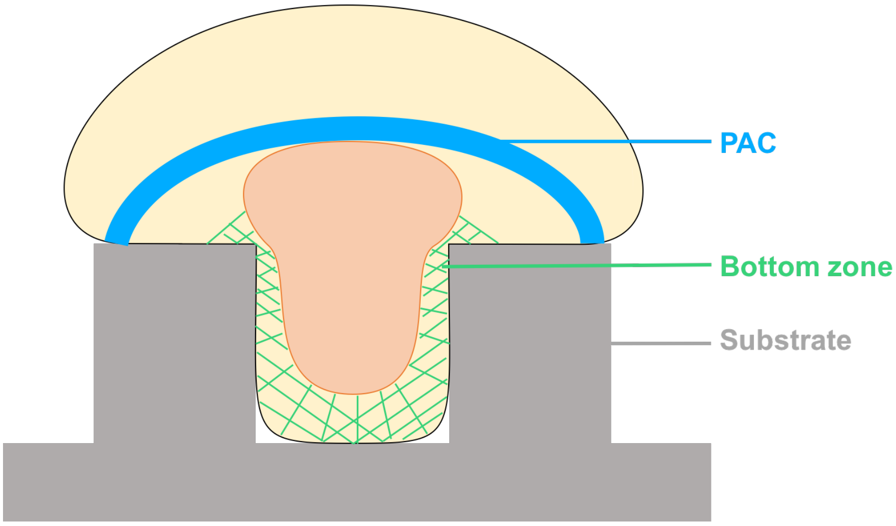

Figure III.13: Illustration of the active zones in the cell with the PAC in blue and the bottom zone checkered in green.

Then, the active strain tensor $\mathbf{F}_a$ is expressed as

$$\mathbf{F}_a = \mathbf{I} + \tilde{\mathbf{F}}_{a,PAC} + \tilde{\mathbf{F}}_{a,bottom} \tag{III.62}$$

with

$$\begin{aligned}\tilde{\mathbf{F}}_{a,PAC} &= g_{PAC} e_{PAC}(t) J_c^2 \mathbf{F}_c^{-T} \mathbf{i}_{t,PAC} \otimes \mathbf{F}_c^{-T} \mathbf{i}_{t,PAC} \\ \tilde{\mathbf{F}}_{a,bottom} &= g_{bottom} e_{bottom}(t) J_c^2 \mathbf{F}_c^{-T} \mathbf{n}_{\mathbf{p},c} \otimes \mathbf{F}_c^{-T} \mathbf{n}_{\mathbf{p},c}\end{aligned} \tag{III.63}$$

$\mathbf{i}_{t,PAC}$ labels the tangent to the PAC in the initial configuration. The time-dependent functions $e_{PAC}(t)$ and $e_{bottom}(t)$ drive the active deformation through regularized Heaviside functions h with a carefully chosen regularization step. In our model, we choose to incorporate actin polymerization in the spreading force. The active strain is then purely contractile.

$$\begin{aligned}e_{PAC}(t) &= e_{PAC,0} h_{cont}(t) \\ e_{bottom}(t) &= e_{bottom,0} h_{cont}(t)\end{aligned} \tag{III.64}$$

where t is the time, $e_{PAC,0}$ and $e_{bottom,0}$ are the amplitudes and $h_{cont}(t)$ is the time function regulating the active contraction (further developed in Sec. III.2.4).

To sum up, we model half a cell as a visco-hyperelastic solid composed of the nucleus and the cytoplasm. The simulation is a four-step process. First, the cell falls towards the substrate under the action of gravity. Second, as it comes into contact with the obstacle, the interpenetration is limited through a repulsive contact force. Third, the cell spreads on the substrate under the action of a radial adhesive force. Eventually, the active region(s) start contracting, thus deforming the nucleus. The following section presents the numerical results of this study that have been submitted to *Physical Biology*.

III.3 Numerical application and results

We implement our model in the finite elements software COMSOL Multiphysics ©. To begin with, we simulate the spreading of the cell on a flat substrate before going to the one with pillars. On the pillars, we first study the action of both contractile regions on the final nuclear deformation to unveil the underlying mechanism. Then, we test the influence of the gravitational force by putting our system upside down after spreading.

III.3.1 Cell geometry

The cell (Ω_{cell}) is considered circular in its original suspended state with a radius $r_{cell} = 10\mu m$. The model chosen here mechanically accounts for a circular nucleus (Ω_n) of radius $r_n = 5\mu m$ and a cytoplasm (Ω_{cp}). Besides, we geometrically define the cell membrane (Ω_m) of thickness $e_m = 250nm$ (see Fig. III.14 a). To describe Ω_{cell}, Ω_n, Ω_{cp} and Ω_m, we use characteristic functions g_{cell}), g_n, g_{cp} and g_m as described in the Appendix

III.A. We only model half the cell and use a symmetry boundary condition. Two active zones are defined through the characteristic function g_{PAC} and g_{bottom} (see Appendix III.C): one above the nucleus for the PAC and the other bellow it (see Fig. III.14 b).

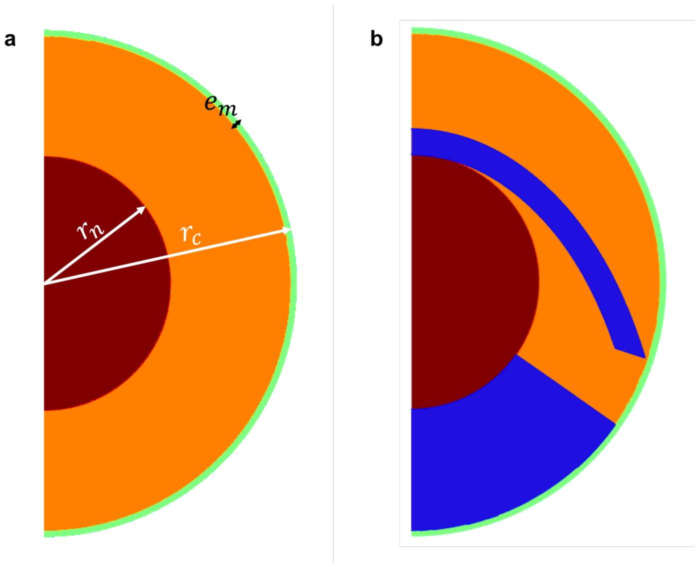

Figure III.14: Geometry of the cell in the initial condition of the system. (a) The cell's membrane in represented in light green, its cytosol in orange and the nucleus in dark red. (b) The active deformations zones are drawn in blue with the PAC forming a dome-like cable above the nucleus and the radial zone below the nucleus.

The nucleus and the cytoplasm have their own Young's modulus that are defined in the right regions through their characteristic functions as follows

$$E_c = E_n g_n + E_{cp} g_{cp} \tag{III.65}$$

This expression of the Young's modulus E_c is used in the Lamé coefficients of the Mooney-Rivlin model (see Eq. III.30).

III.3.2 Cell spreading on a flat substrate

The first step of our study is to confront the model to a flat substrate in order to validate its behaviour with respect to the existing literature before taking it to a structured substrate. The cell settles on a flat substrate and spreads under the action of the radial spreading force in a $2\mu m$-thick layer over the substrate. In this simulation, we do not consider any active contraction, but we study the sheer action of the spreading force (see Fig. III.15).

In all the simulations, the cell is initially positioned in the over layer, although not touching the substrate for the gravity step to converge more easily. In order to quantitatively evaluate these results, we plot the contact radius between the cell and the flat

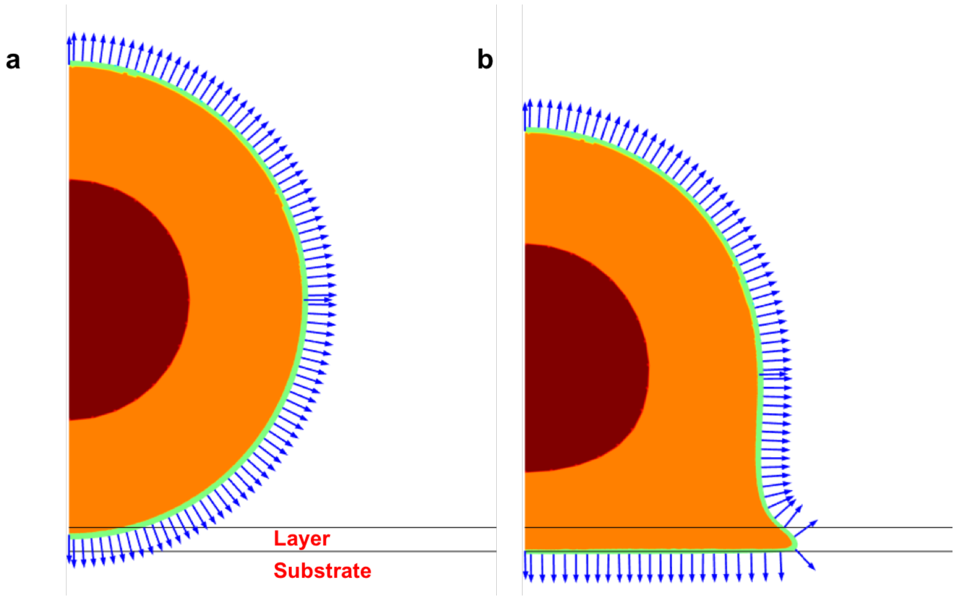

Figure III.15: Cell spreading on a flat substrate with its overlayer: (a) initial configuration, (b) deformed configuration at $t = T_g + T_s$. Blue arrows represent the normal to the cell.

substrate (see Fig. III.16). Gravity slightly increases the contact surface up to 1 μm. When the spreading process begins however, we observe a much faster spreading with a maximum contact radius of 8.8 μm. This is in agreement with the results presented in Cuvelier et al. [2007]. Our model is thus able to capture the essential features of cell spreading on a flat substrate.

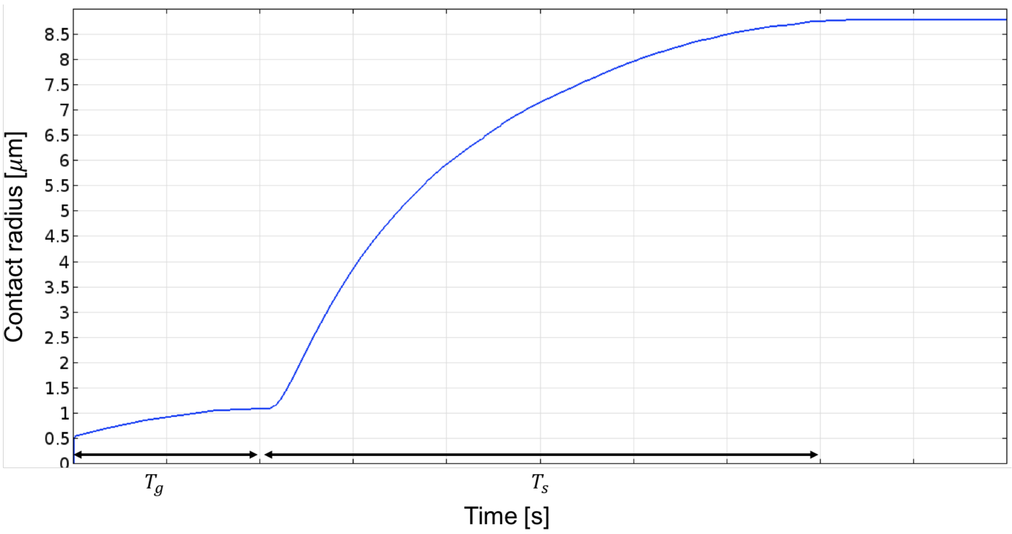

Figure III.16: Contact radius of the cell spreading over a flat substrate as function of time, as defined in [Cuvelier et al., 2007].

III.3.3 Cell spreading on a micro-pillared substrate

Once tested on a flat substrate, we now confront our model to a more complex topography. In the experiments we aim to reproduce, suspended cells are plated on an array of micro-fabricated pillars (see Fig. III.1 for experimental example) [Badique et al., 2013; Pan et al., 2012; Hanson et al., 2015; Ghibaudo et al., 2011]. For simplification reasons, we represent here a cross-section of a single cell between pillars in 2D (see Fig. III.17). The overall substrate is composed of the pillars and the ground plate on which they are set . It is represented through the characteristic function $g_{substrate}$ as detailed in Appendix III.B .

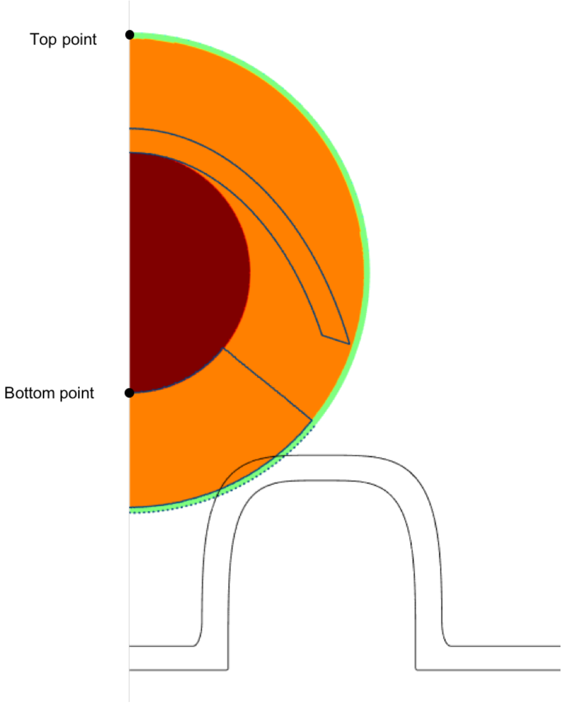

Figure III.17: Geometry of the cell and the micro-pillared substrate in the initial configuration of the system. The actin deformation zones are drawn in dark blue. The top and bottom points of the cell and nucleus,respectively, are highlighted in black dots.

From this configuration we want to tackle two important questions:

1. Is the nucleus being pushed or pulled in the inter-pillars gap ?
2. What is the role of the gravity in the cell spreading process ?

Numerical simulation is particularly relevant to answer such questions since we can implement the various hypotheses and analyze the results, with respect to the existing literature.

a Push or Pull ? Clarifying the mechanism behind nuclear deformation

The first matter we want to address in this study is the mechanism by which the nucleus deforms to fit in the inter-pillars space. We test whether the nucleus is being pushed by the PAC (Push), pulled from below by contractile fibers concentrated around the pillars (Pull) or a combination of both (Push & Pull). The results are presented in Fig. III.18.

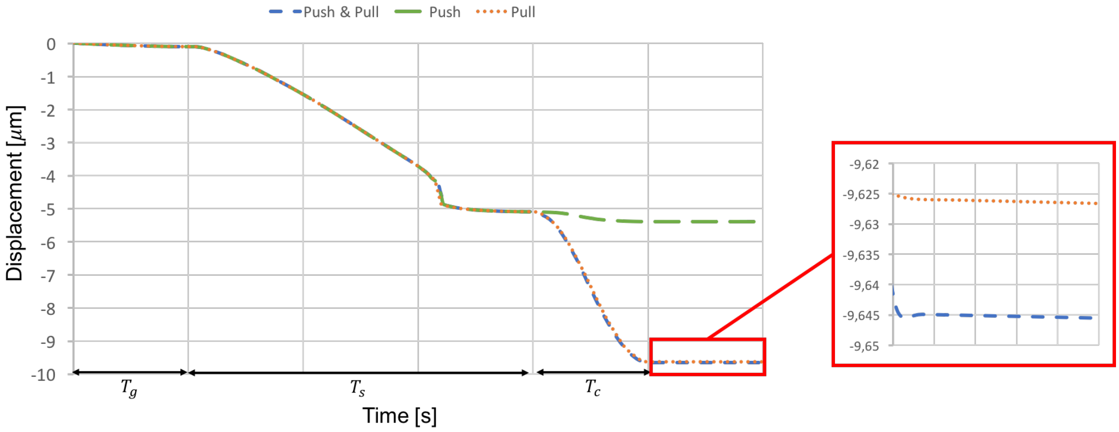

Figure III.18: Displacement d_n of the bottom point of the nucleus for different configuration: Push & Pull (blue), Push (green) and Pull (orange)

The gravity has very little effect on the displacement of the bottom of the cell nucleus d_n (see Fig. III.17), mostly corresponding to the cell simply settling down on the pillars, and $d_n = -0.1\mu m$ at $t = T_g$. During the spreading phase, for $T_g \leq t \leq T_g + T_s$, the nucleus gets positioned at the beginning of the gap but isn't fully engaged yet, with $d_n = -5\mu m$ (see Fig. III.19). Eventually, the contractile phase, for $T_g + T_s \leq t \leq T_g + T_s + T_c$, differs depending on the hypothesis made. When only the PAC contracts (Push - green line in Fig. III.18), we are in the least efficient case with a maximum displacement $d_n = -5.4\mu m$ (see Fig. III.19 A). The two curves for the Pull case (Orange line in Fig. III.18, and Fig. III.19 B), where the nucleus is being pulled radially around the pillar, and the Push & Pull case (Blue line in Fig. III.18, and Fig. III.19 C), where the two previous mechanisms are combined, are very close, reaching $d_n = 9.6\mu m$. Having a closer look shows that the combined strategy is slightly more efficient than the Pull strategy on itself. The difference is however only of $0.01\mu m$, which we consider insignificant here. We can thus conclude that the nucleus is mostly being pulled towards the substrate, although the Push & Pull combination gives similar results. In Hanson et al. [2015], the Push strategy is also the least efficient one, although the difference between the Push and the Push & Pull strategies is more pronounced. However, the difference in results can be explained by the varied pillars geometry and the simplified modeling choices.

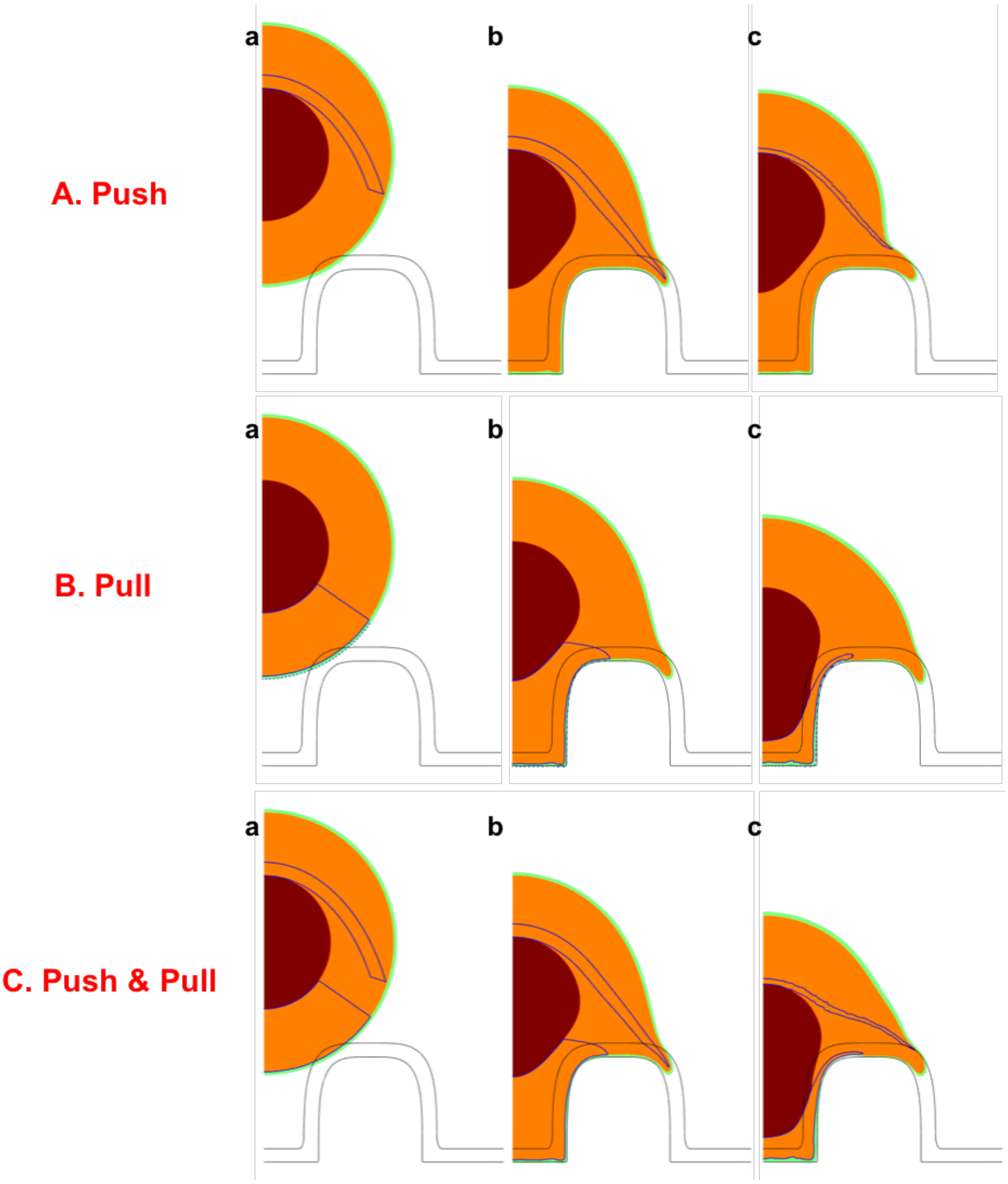

Figure III.19: Simulation results for (A) Push, (B) Pull and (C) Push & Pull simulation. Three time points are represented for each: (a) Initial configuration, (b) End of the spreading phase, (c) End of active contraction phase

b Gravity is not responsible for nuclear deformation

The second main question tackled here is the role of the gravity. As raised by Pan et al. [2012]: "Is gravity responsible for the deformation ?" To answer, they let the cell spread on micropillars and the nucleus deform. Once a stationary state was achieved, they put the device upside down and compared the nuclear deformation. To reproduce this experimental strategy, we consider a "control" case corresponding to the Push & Pull strategy from before and an "upside down" case. In the latter, the cell spreads as in the control case and then, the gravity is reversed for $t > T_g + T_s + T_c$: $\rho_p \mathbf{g}$ becomes $-\rho_p \mathbf{g}$. The results are presented in Fig. III.20. On the overall curves, we cannot spot any noticeable difference. If we zoom in on the time period where the gravity is reversed, we observe a light effect of the gravity that is however negligible: less than $0.1 \mu m$ compared to the total $7.5 \mu m$ displacement of the top of the nucleus. These results are perfectly in agreement with the experiments from Pan et al. [2012], thus validating this aspect of our model.

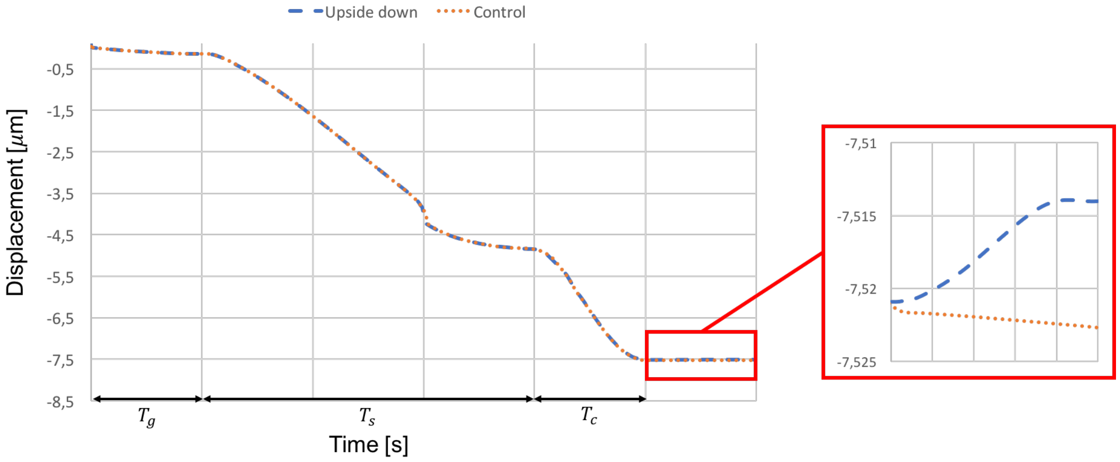

Figure III.20: Displacement of the top point of the cell for different configuration: Upside down (blue) and Control (orange)

III.4 Conclusion and discussion

The model we present here is the first advanced mechanical one to investigate the mechanism behind nuclear deformation during cell spreading over a micro-pillared substrate. Experiments on this topic have been developed and two possible strategies were outlined, based on the position of filamentous actin in the spread cells. The nucleus is thought to either be pushed from above by the contractile PAC, or pulled from below by contractile actin fibers gathered around the pillars. We build a 2D FE model of half a cell, with symmetry boundary conditions. It is subject to gravity, a repulsive contact force at the interface with the substrate, a radial spreading force and active contractile strains through deformation gradient decomposition. First, the cell is plated on a flat substrate and no contractile strains are activated. This first step enables us to validate the behaviour of our spreading model with respect to the existing literature. Then, we subject our cell model to a micro-pillared substrate. By spreading alone, the nucleus does not deform sufficiently to penetrate the inter-pillars gap, which supports the hypothesis of necessary active contraction in the cell. To evaluate the influence of each active deformation, we activate either one of them, and then both of them together. As a result, we observe that the PAC has very little influence on nuclear deformation after spreading, while bottom contraction alone is merely as efficient as the combination of both contractions. We can conclude from this study that the nucleus is mostly being pulled from below to achieve its deformation. The second question that had been raised in the literature was to expose whether gravity was responsible for nuclear deformation. As the experiments had shown, we confirm the validity of our model with respect to this hypothesis since we observe no significant influence of the inversion of gravity on the displacement of the nucleus.

Hence, our model appears as a great tool to examine to mechanical mechanisms involved in cell spreading over flat to topographically structured substrates. Nevertheless, some limitations may be drawn. First, we decided here to stick to a 2D representation for computing time reasons. However, a 3D representation of the system (i.e. both the cell and the micro-structured substrate) would allow to catch more realistically the cellular strains and the adaptability of the cell and the nucleus to their environment, specifically since the third dimension would give more space for the cell and the nucleus to deform. Secondly, the successive phases of our model (i.e. gravity, adhesion, spreading and active strains) are "user controlled" as they are fully determined by time-dependent functions that we designed. One great advance would be to let these steps depend on one or more specific physical quantities so that the system would be self-regulated based on its current state. Besides, we did not consider any stiffening if the stress fibers in our model that would be supplemented through Ogden and Holzapfel's theory on cross-linked F-actin networks [Holzapfel et al., 2014]. Then, we represent the cell here as a continuum but are currently working on a discrete description of the domain where the actin filaments are physically represented and will be the main actors of both the active strains and the adhesion sites. Indeed, our approach can be seen as a homogenization of such phenomenon which can lead to a loss of information. Our study could be further extended by studying the influence of the pillars geometry or of the cell's mechanical parameters on the system's evolution. We assume that the cell adheres uniformly on the substrate, but another path for development would be to localize the adhesion on certain zones of the pillars only. This would experimentally correspond to changing the distribution of the fibronectin coated on the substrate. Eventually, we did not take into account the membrane reservoir recruitment generated by the unfolding of wrinkles in the membrane that would lead to an eased spreading phase. More budding perspectives to take this model further are to be developed in the next Chapter.

Appendices

III.A Cell geometry

In this chapter, each cellular component is geometrically defined through a characteristic function g, which is a composition of a Heaviside function h and a spatial level set l as follows

$$g_i(\mathbf{x}) = h \circ l_i(\mathbf{x}) = \begin{cases} 1 & \text{for } l_i(\mathbf{x}) > 0 \\ 0 & \text{for } l_i(\mathbf{x}) < 0 \end{cases} \tag{III.66}$$

where where i = n, cp, m.

For the nucleus, we have

$$g_n(\mathbf{p}) = \begin{cases} 1 & \text{if } \|\mathbf{p} - \mathbf{c}_{cell}\| < r_n \\ 0 & \text{otherwise} \end{cases} \tag{III.67}$$

where $\mathbf{c}_{cell}$ is the position of the center of the cell.

For the cytoplasm, we have

$$g_{cp}(\mathbf{p}) = \begin{cases} 1 & \text{if } r_n < \|\mathbf{p} - \mathbf{c}_{cell}\| < r_{cell} \\ 0 & \text{otherwise} \end{cases} \tag{III.68}$$

Eventually, the membrane is defined by

$$g_m(\mathbf{p}) = \begin{cases} 1 & \text{if } (r_{cell} - e_m) < \|\mathbf{p} - \mathbf{c}_{cell}\| < r_{cell} \\ 0 & \text{otherwise} \end{cases} \tag{III.69}$$

The complete cell is the defined as $g_{cell} = g_n + g_{cp}$. For later use, we also define the cytosol $g_{cl} = g_{cp} - g_m$. Fig. III.14 illustrates the components of the cell.

III.B Substrate geometry

Pillared substrate

The complete substrate is represented as the sum of the pillars and the ground through the levelset function $l_{substrate} = l_{pillars} + l_{ground}$. The characteristic function of the substrate $g_{substrate}$ is then the Heaviside of the levelset function as $g_{substrate} = h \circ l_{substrate}$. For the pillars, we have

$$l_{pillars} = |x - x_{0,p} - (s_p + w_p) \cdot round(\frac{x - x_{0,p}}{s_p + w_p})|^4 + |y - y_{0,p}|^k - (\frac{w_p}{2})^4 \tag{III.70}$$

with (x, y) the coordinates of **p** and $round()$ the function that rounds to the nearest integer. $x_{0,p}$ and $y_{0,p}$ characterize the first pillar's position, while k, s_p and w_p define the pillars' height, the space between the pillars and the width of the pillars. This function thus defines an infinite number of pillars and we can simply choose to plot as many as we see fit.

The ground is defined by a semi-infinite plane at a y-position s_0 as

$$l_{ground} = -y + s_0 \tag{III.71}$$

The overlayer is defined through its characteristic function $g_{layer} = g_{pillars,layer} + g_{ground,layer}$. The layer is obtained by substracting a "larger" pillar $g_{pillars,L}$ from the normal one (and similarly for the ground $g_{ground,L}$), with a subscript L.

$$\begin{aligned} g_{pillars,layer} &= g_{pillars,L} - g_{pillars} \\ g_{ground,layer} &= g_{ground,L} - g_{ground} \end{aligned} \tag{III.72}$$

The corresponding levelset functions read

$$\begin{aligned} &l_{pillars,L} = |x - x_{0,p} - (s_p + w_p) \cdot round(\frac{x - x_{0,p}}{s_p + w_p})|^4 + |y - y_{0,p}|^{k_L} - (\frac{w_{p,L}}{2})^4 \\ &l_{ground,L} = -y + s_{0,L} \end{aligned} \tag{III.73}$$

Two pillars and the corresponding overlayer have been plotted in Fig. III.11.

Flat substrate

In the case of the flat substrate, we consider no pillars, and we only have :

$$l_{ground,flat} = -y + s_{0,flat} \tag{III.74}$$

Similarly as before, the overlayer $g_{ground,flat,layer} = g_{ground,flat,L} - g_{ground,flat}$ and

$$l_{ground,flat,L} = -y + s_{0,flat,L} \tag{III.75}$$

This specific setup is illustrated bi Fig. III.15.

III.C Active domains

As previously, the characteristic functions g_{PAC} and g_{bottom} are defined in the initial configuration as Heaviside functions of levelsets l_{PAC} and l_{bottom} respectively (see Fig. III.C.1). The PAC is characterized by the portion of an ellipse which parameters are chosen so that the deformed configuration is coherent. The bottom active domain is a radial portion of the cytoplasm chosen so that the deformed configuration is coherent as well.

$$g_{PAC}(\mathbf{p}) = g_{PAC,ext} - g_{PAC,int} \text{ for } \theta \geq \theta_{PAC} \tag{III.76}$$

where θ is the angle defined as $\theta = atan2\left(\frac{y-y_{0,cell}}{x-x_{0,cell}}\right)$, $x_{0,cell}$ and $y_{0,cell}$ being the coordinates of the center of the cell in the initial configuration. $g_{PAC,ext}$ and $g_{PAC,int}$ are Heavisides of two levelset functions of ellipses, in order to build an ellipsoidal shell. θ_{PAC} is the cutting angle of the ellipsoidal shell.

$$\begin{aligned} l_{PAC,ext}(\mathbf{p}) &= -\left(\frac{x-x_{0,PAC}}{a_{PAC,ext}}\right)^2 - \left(\frac{y-y_{0,PAC}}{b_{PAC,ext}}\right)^2 + 1 \\ l_{PAC,int}(\mathbf{p}) &= -\left(\frac{x-x_{0,PAC}}{a_{PAC,int}}\right)^2 - \left(\frac{y-y_{0,PAC}}{b_{PAC,int}}\right)^2 + 1 \end{aligned} \tag{III.77}$$

$$g_{bottom}(\mathbf{p}) = g_{cl}(\mathbf{p}) \text{ for } \theta \leq \theta_{bottom} \tag{III.78}$$

where θ_{bottom} is the cutting angle of the bottom radial zone.

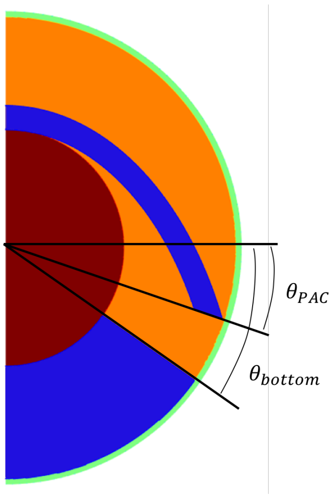

Figure III.C.1: Geometry of the active domains (in electric blue) in the cell and definition of θ_{PAC} and θ_{bottom}

III.D Time functions

The phases of the simulation are controlled by the functions $h_g(t)$, $h_{spread}(t)$ and $h_{cont}(t)$ defined through the regularized Heaviside function $h()$ as follows:

$$\begin{aligned} h_g(t) &= h(t - \frac{T_g}{2}, \frac{T_g}{2}) \\ h_{spread}(t) &= h(t - T_g - \frac{T_s}{2}, \frac{T_s}{2}) \\ h_{cont}(t) &= h(t - T_g - T_s - \frac{T_c}{2}, \frac{T_c}{2}) \end{aligned} \tag{III.79}$$

where T_g, T_c and T_s are the time spans of the gravity, spreading and contractile phases, respectively. $h(t - \frac{T_g}{2}, \frac{T_g}{2})$ defines a function that varies smoothly from 0 to 1 for $t \in [0, T_g]$ (see Fig. III.9). Similarly, $h_{spread}(t)$ is 0 for $t \leq T_g$, 1 at $t \geq T_g + T_s$ and varies smoothly in between. The same reasoning can be applied of $h_{cont}(t)$.

III.E Parameters of the problem

Some parameters of the problem have simply been chosen to reproduce experiments and defined the geometry and time phases of the simulation (see Table III.E.1). Others characterize the mechanical behaviour of the cell and can be open to discussion as they affect the results of our study (see Table III.E.2).

Table III.E.1: Values and description of the model's parameters

Parameter	Description	Value
	Geometrical parameters	
$x_{0,cell}$	x-position of the cell center	0 μm
$y_{0,cell}$	y-position of the cell center	8.5 μm
r_{cell}	Cell radius	10 μm
r_n	Nucleus radius	5 μm
e_m	Membrane thickness	0.25 μm
$x_{0,p}$	x-position of the center of the first pillar	8 μm
$y_{0,p}$	y-position of the center of the first pillar	-8 μm
s_p	Inter-pillars gaps	8 μm
w_p	Pillars width	8 μm
k	Pillar parameter	4.24
s_0	Ground height	-8 μm
s_{flat}	Ground height for the flat substrate case	-2 μm
k_L	Overlayer pillars parameter	4.20
$w_{p,L}$	Overlayer pillars parameter	10 μm
$s_{0,L}$	Overlayer ground height	-6 μm
$s_{flat,L}$	Overlayer ground height for the flat substrate case	0 μm
θ_{PAC}	Defining angle for the PAC active domain	-18°
θ_{bottom}	Defining angle for the bottom active domain	-35°
$a_{PAC,ext}$	External first semi-axis of the PAC active domain	10 μm
$a_{PAC,int}$	Internal first semi-axis of the PAC active domain	9 μm
$b_{PAC,ext}$	External second semi-axis of the PAC active domain	15 μm
$b_{PAC,int}$	Internal second semi-axis of the PAC active domain	14 μm
	Problem definition	
T_g	Duration of the gravity phase	10.000 s
T_s	Duration of the spreading phase	30.000 s
T_c	Duration of the contractile phase	10.000 s
$\mu_{contact}$	Contact coefficient	2.10^9 N
$v_{spread,0}$	FA maturation velocity	1.10^6 N/s
$\mu_{spread,max}$	Maximum spreading coefficient	$1.4.10^9$ N
$e_{PAC,0}$	Amplitude of active deformation in the PAC domain	0.7
$e_{bottom,0}$	Amplitude of active deformation in the bottom domain	0.7

Table III.E.2: Mechanical parameters

Parameter	Description	Value	Reference
ρ_{cp}	Cytoplasm density	1000 kg/m^3	[Milo and Phillips, 2015]
ρ_n	Nucleus density	1400 kg/m^3	[Milo and Phillips, 2015]
E_{cp}	Cytoplasm Young's modulus	100 Pa	[Caille et al., 2002]
E_n	Nucleus Young's modulus	500 Pa	[Caille et al., 2002]
ν_c	Cell's Poisson ratio	0.485	
λ_f	Isotropic viscosity	1000 Pa.s	
μ_f	Deviatoric viscosity	$2.10^{-3} Pa.s$	

Bibliography

Abercrombie, M., Heaysman, J. E., and Pegrum, S. M. (1970). The locomotion of fibroblasts in culture I. Movements of the leading edge. *Experimental Cell Research*, 59(3):393–398. 94

Albert, P. J. and Schwarz, U. S. (2014). Dynamics of Cell Shape and Forces on Micropatterned Substrates Predicted by a Cellular Potts Model. *Biophysical Journal*, 106(11):2340–2352. 97

Alexandrova, A. Y., Arnold, K., Schaub, S., Vasiliev, J. M., Meister, J.-J., Bershadsky, A. D., and Verkhovsky, A. B. (2008). Comparative dynamics of retrograde actin flow and focal adhesions: formation of nascent adhesions triggers transition from fast to slow flow. *PloS one*, 3(9):e3234. 94

Allena, R. and Aubry, D. (2012). 'Run-and-tumble' or 'look-and-run'? A mechanical model to explore the behavior of a migrating amoeboid cell. *Journal of Theoretical Biology*, 306:15–31. 98, 105

Aubry, D., Thiam, H., Piel, M., and Allena, R. (2014). A computational mechanics approach to assess the link between cell morphology and forces during confined migration. *Biomechanics and Modeling in Mechanobiology*, 14(1):143–157. 98

Badique, F., Stamov, D. R., Davidson, P. M., Veuillet, M., Reiter, G., Freund, J.-N., Franz, C. M., and Anselme, K. (2013). Directing nuclear deformation on micropillared surfaces by substrate geometry and cytoskeleton organization. *Biomaterials*, 34(12):2991–3001. 92, 93, 119, 154

Benjamin, M. and Hillen, B. (2003). Mechanical influences on cells, tissues and organs - 'Mechanical Morphogenesis'. *European Journal of Morphology*, 41(1):3–7. 92

Bonet, J., Gil, A. J., and Ortigosa, R. (2015). A computational framework for polyconvex large strain elasticity. *Computer Methods in Applied Mechanics and Engineering*, 283:1061–1094. 103, 106

Bonet, J. and Wood, R. D. (1997). *Nonlinear continuum mechanics for finite element analysis*. Cambridge University Press, Cambridge ; New York, NY, USA. 103

Cai, Y., Biais, N., Giannone, G., Tanase, M., Jiang, G., Hofman, J. M., Wiggins, C. H., Silberzan, P., Buguin, A., Ladoux, B., and Sheetz, M. P. (2006). Nonmuscle Myosin IIA-Dependent Force Inhibits Cell Spreading and Drives F-Actin Flow. *Biophysical Journal*, 91(10):3907–3920. 93

Caille, N., Thoumine, O., Tardy, Y., and Meister, J.-J. (2002). Contribution of the nucleus to the mechanical properties of endothelial cells. *Journal of Biomechanics*, 35(2):177–187. 129

Cao, X., Lin, Y., Driscoll, T. P., Franco-Barraza, J., Cukierman, E., Mauck, R. L., and Shenoy, V. B. (2015). A Chemomechanical Model of Matrix and Nuclear Rigidity Regulation of Focal Adhesion Size. *Biophysical Journal*, 109(9):1807–1817. 96, 97

Cuvelier, D., Théry, M., Chu, Y.-S., Dufour, S., Thiéry, J.-P., Bornens, M., Nassoy, P., and Mahadevan, L. (2007). The Universal Dynamics of Cell Spreading. *Current Biology*, 17(8):694–699. 93, 96, 118, 154

Davidson, P. M., Fromigué, O., Marie, P. J., Hasirci, V., Reiter, G., and Anselme, K. (2010). Topographically induced self-deformation of the nuclei of cells: dependence on cell type and proposed mechanisms. *Journal of Materials Science: Materials in Medicine*, 21(3):939–946. 92

Davidson, P. M., Sliz, J., Isermann, P., Denais, C., and Lammerding, J. (2015). Design of a microfluidic device to quantify dynamic intra-nuclear deformation during cell migration through confining environments. *Integr. Biol.*, 7(12):1534–1546. 92, 98

Davidson, P. M., Özçelik, H., Hasirci, V., Reiter, G., and Anselme, K. (2009). Microstructured Surfaces Cause Severe but Non-Detrimental Deformation of the Cell Nucleus. *Advanced Materials*, 21(35):3586–3590. 92

Deveraux, S., Allena, R., and Aubry, D. (2017). A numerical model suggests the interplay between nuclear plasticity and stiffness during a perfusion assay. *Journal of Theoretical Biology*, 435:62–77. 98, 106

Döbereiner, H.-G., Dubin-Thaler, B., Giannone, G., Xenias, H. S., and Sheetz, M. P. (2004). Dynamic Phase Transitions in Cell Spreading. *Physical Review Letters*, 93(10). 93

Eichhorn, M., Stannard, C., Anselme, K., and Rühe, J. (2015). Nucleus deformation of SaOs-2 cells on rhombic µ-pillars. *Journal of Materials Science: Materials in Medicine*, 26(2). 92

Ermis, M., Akkaynak, D., Chen, P., Demirci, U., and Hasirci, V. (2016). A high throughput approach for analysis of cell nuclear deformability at single cell level. *Scientific Reports*, 6(1). 92

Etienne, J. and Duperray, A. (2011). Initial Dynamics of Cell Spreading Are Governed by Dissipation in the Actin Cortex. *Biophysical Journal*, 101(3):611–621. 97

Fan, H. and Li, S. (2015). Modeling universal dynamics of cell spreading on elastic substrates. *Biomechanics and Modeling in Mechanobiology*, 14(6):1265–1280. 97, 98, 105

Fang, Y. and Lai, K. W. C. (2016). Modeling the mechanics of cells in the cell-spreading process driven by traction forces. *Physical Review E*, 93(4). 97, 98

Fried, I. and Johnson, A. R. (1988). A note on elastic energy density functions for largely deformed compressible rubber solids. *Computer Methods in Applied Mechanics and Engineering*, 69(1):53–64. 106

Gauthier, N. C., Fardin, M. A., Roca-Cusachs, P., and Sheetz, M. P. (2011). Temporary increase in plasma membrane tension coordinates the activation of exocytosis and contraction during cell spreading. *Proceedings of the National Academy of Sciences*, 108(35):14467–14472. 93

Geiger, B., Spatz, J. P., and Bershadsky, A. D. (2009). Environmental sensing through focal adhesions. *Nature Reviews Molecular Cell Biology*, 10(1):21–33. 94, 114

Geiger, B. and Yamada, K. M. (2011). Molecular Architecture and Function of Matrix Adhesions. *Cold Spring Harbor Perspectives in Biology*, 3(5):a005033–a005033. 94

Ghibaudo, M., Di Meglio, J.-M., Hersen, P., and Ladoux, B. (2011). Mechanics of cell spreading within 3d-micropatterned environments. *Lab on a Chip*, 11(5):805–812. 92, 98, 119

Goktepe, S., Abilez, O. J., Parker, K. K., and Kuhl, E. (2010). A multiscale model for eccentric and concentric cardiac growth through sarcomerogenesis. *Journal of Theoretical Biology*, 265(3):433–442. 106

Golestaneh, A. F. and Nadler, B. (2016). Modeling of cell adhesion and deformation mediated by receptor-ligand interactions. *Biomechanics and Modeling in Mechanobiology*, 15(2):371–387. 97, 106

Gossett, D. R., Tse, H. T. K., Lee, S. A., Ying, Y., Lindgren, A. G., Yang, O. O., Rao, J., Clark, A. T., and Di Carlo, D. (2012). Hydrodynamic stretching of single cells for large population mechanical phenotyping. *Proceedings of the National Academy of Sciences*, 109(20):7630–7635. 92

Graveleau, M., Chevaugeon, N., and Moës, N. (2015). The inequality level-set approach to handle contact: membrane case. *Advanced Modeling and Simulation in Engineering Sciences*, 2(1). 112

Gurtin, M. E. (1982). *An Introduction to Continuum Mechanics*. Academic Press. 101

Hanson, L., Zhao, W., Lou, H.-Y., Lin, Z. C., Lee, S. W., Chowdary, P., Cui, Y., and Cui, B. (2015). Vertical nanopillars for in situ probing of nuclear mechanics in adherent cells. *Nature nanotechnology*, 10(6):554–562. 92, 97, 98, 119, 120

Holzapfel, G. A. (2000). *Nonlinear solid mechanics : a continuum approach for engineering*. Wiley, Chichester. 103

Holzapfel, G. A., Unterberger, M. J., and Ogden, R. W. (2014). An affine continuum mechanical model for cross-linked F-actin networks with compliant linker proteins. *Journal of the Mechanical Behavior of Biomedical Materials*, 38:78–90. 123

Hou, H. W., Li, Q. S., Lee, G. Y. H., Kumar, A. P., Ong, C. N., and Lim, C. T. (2009). Deformability study of breast cancer cells using microfluidics. *Biomedical Microdevices*, 11(3):557–564. 92

Ingber, D. E. (2003). Tensegrity I. Cell structure and hierarchical systems biology. *Journal of Cell Science*, 116(7):1157–1173. 96, 154

Isermann, P., Davidson, P. M., Sliz, J. D., and Lammerding, J. (2012). Assays to Measure Nuclear Mechanics in Interphase Cells. In *Current Protocols in Cell Biology*. John Wiley & Sons, Inc. 92

Itskov, M. and Aksel, N. (2004). A class of orthotropic and transversely isotropic hyperelastic constitutive models based on a polyconvex strain energy function. *International Journal of Solids and Structures*, 41(14):3833–3848. 103

Jansen, K. A., Atherton, P., and Ballestrem, C. (2017). Mechanotransduction at the cell-matrix interface. *Seminars in Cell & Developmental Biology*, 71:75–83. 94

Jean, R. P., Chen, C. S., and Spector, A. A. (2003). Analysis of the Deformation of the Nucleus as a Result of Alterations of the Cell Adhesion Area. pages 121–122. 105

Jiang, Y., Wang, Y., and Peng, X. (2015). A Visco-Hyperelastic Constitutive Model for Human Spine Ligaments. *Cell Biochemistry and Biophysics*, 71(2):1147–1156. 102

Keren, K. (2011). Membrane tension leads the way. *Proceedings of the National Academy of Sciences*, 108(35):14379–14380. 93

Khatau, S. B., Hale, C. M., Stewart-Hutchinson, P. J., Patel, M. S., Stewart, C. L., Searson, P. C., Hodzic, D., and Wirtz, D. (2009). A perinuclear actin cap regulates nuclear shape. *Proceedings of the National Academy of Sciences*, 106(45):19017–19022. 98

Kim, D.-H., Cho, S., and Wirtz, D. (2014). Tight coupling between nucleus and cell migration through the perinuclear actin cap. *Journal of Cell Science*, 127(11):2528–2541. WOS:000337217400015. 99

Kim, D.-H., Khatau, S. B., Feng, Y., Walcott, S., Sun, S. X., Longmore, G. D., and Wirtz, D. (2012). Actin cap associated focal adhesions and their distinct role in cellular mechanosensing. *Scientific Reports*, 2(1). 99

Li, Y., Lovett, D., Zhang, Q., Neelam, S., Kuchibhotla, R. A., Zhu, R., Gundersen, G. G., Lele, T. P., and Dickinson, R. B. (2015). Moving Cell Boundaries Drive Nuclear Shaping during Cell Spreading. *Biophysical Journal*, 109(4):670–686. 97

Liu, P., Zhang, Y. W., Cheng, Q. H., and Lu, C. (2007). Simulations of the spreading of a vesicle on a substrate surface mediated by receptor-ligand binding. *Journal of the Mechanics and Physics of Solids*, 55(6):1166–1181. 97

Loosli, Y., Luginbuehl, R., and Snedeker, J. G. (2010). Cytoskeleton reorganization of spreading cells on micro-patterned islands: a functional model. *Philosophical Transactions of the Royal Society A: Mathematical, Physical and Engineering Sciences*, 368(1920):2629–2652. 95

Lu, H., Koo, L. Y., Wang, W. C. M., Lauffenburger, D. A., Griffith, L. G., and Jensen, K. F. (2004). Microfluidic shear devices for quantitative analysis of cell adhesion. *Analytical Chemistry*, 76(18):5257–5264. WOS:000223928800003. 92

Lubarda, V. A. (2004). Constitutive theories based on the multiplicative decomposition of deformation gradient: Thermoelasticity, elastoplasticity, and biomechanics. *Applied Mechanics Reviews*, 57(2):95. 106

Mammoto, T. and Ingber, D. E. (2010). Mechanical control of tissue and organ development. *Development*, 137(9):1407–1420. 92

Maninova, M., Caslavsky, J., and Vomastek, T. (2017). The assembly and function of perinuclear actin cap in migrating cells. *Protoplasma*, 254(3):1207–1218. 98

Maurin, B., Canadas, P., Baudriller, H., Montcourrier, P., and Bettache, N. (2008). Mechanical model of cytoskeleton structuration during cell adhesion and spreading. *Journal of Biomechanics*, 41(9):2036–2041. 96

McGrath, J. L. (2007). Cell Spreading: The Power to Simplify. *Current Biology*, 17(10):R357–R358. 93, 154

Milan, J.-L., Lavenus, S., Pilet, P., Louarn, G., Wendling, S., Heymann, D., Layrolle, P., and Chabrand, P. (2013). Computational model combined with in vitro experiments to analyse mechanotransduction during mesenchymal stem cell adhesion. *European cells & materials*, 25:97–113. 96

Milo, R. and Phillips, R. (2015). *Cell Biology by the Numbers*. Garland Science. Google-Books-ID: 9NPRCgAAQBAJ. 129

Mokbel, M., Mokbel, D., Mietke, A., TrÃ€ber, N., Girardo, S., Otto, O., Guck, J., and Aland, S. (2017). Numerical Simulation of Real-Time Deformability Cytometry To Extract Cell Mechanical Properties. *ACS Biomaterials Science & Engineering*, 3(11):2962–2973. 105

Morgan, M. R., Humphries, M. J., and Bass, M. D. (2007). Synergistic control of cell adhesion by integrins and syndecans. *Nature Reviews Molecular Cell Biology*, 8(12):957–969. 94

Munoz, J. J., Barrett, K., and Miodownik, M. (2007). A deformation gradient decomposition method for the analysis of the mechanics of morphogenesis. *Journal of Biomechanics*, 40(6):1372–1380. 106

Nisenholz, N., Rajendran, K., Dang, Q., Chen, H., Kemkemer, R., Krishnan, R., and Zemel, A. (2014). Active mechanics and dynamics of cell spreading on elastic substrates. *Soft Matter*, 10(37):7234. 96

Pan, Z., Yan, C., Peng, R., Zhao, Y., He, Y., and Ding, J. (2012). Control of cell nucleus shapes via micropillar patterns. *Biomaterials*, 33(6):1730–1735. 92, 99, 119, 121, 122, 154

Parsons, J. T., Horwitz, A. R., and Schwartz, M. A. (2010). Cell adhesion: integrating cytoskeletal dynamics and cellular tension. *Nature reviews. Molecular cell biology*, 11(9):633–643. 94

Partridge, M. A. and Marcantonio, E. E. (2006). Initiation of attachment and generation of mature focal adhesions by integrin-containing filopodia in cell spreading., Initiation of Attachment and Generation of Mature Focal Adhesions by Integrin-containing Filopodia in Cell Spreading. *Molecular biology of the cell, Molecular Biology of the Cell*, 17, 17(10, 10):4237, 4237–4248. 94

Polacheck, W. J., Charest, J. L., and Kamm, R. D. (2011). Interstitial flow influences direction of tumor cell migration through competing mechanisms. *Proceedings of the National Academy of Sciences*, 108(27):11115–11120. 92

Roca-Cusachs, P., Rio, A. d., Puklin-Faucher, E., Gauthier, N. C., Biais, N., and Sheetz, M. P. (2013). Integrin-dependent force transmission to the extracellular matrix by Î±-actinin triggers adhesion maturation. *Proceedings of the National Academy of Sciences*, 110(15):E1361–E1370. 94

Rodriguez, E. K., Hoger, A., and McCulloch, A. D. (1994). Stress-dependent finite growth in soft elastic tissues. *Journal of Biomechanics*, 27(4):455–467. 106

Rosenbluth, M. J., Lam, W. A., and Fletcher, D. A. (2008). Analyzing cell mechanics in hematologic diseases with microfluidic biophysical flow cytometry. *Lab on a Chip*, 8(7):1062. 92

Roux, C., Duperray, A., Laurent, V. M., Michel, R., Peschetola, V., Verdier, C., and Étienne, J. (2016). Prediction of traction forces of motile cells. *Interface Focus*, 6(5):20160042. 97

Sarvestani, A. S. and Jabbari, E. (2008). Modeling the kinetics of cell membrane spreading on substrates with ligand density gradient. *Journal of Biomechanics*, 41(4):921–925. 96

Sauer, R. A. (2016). A Survey of Computational Models for Adhesion. *The Journal of Adhesion*, 92(2):81–120. 98, 113

Schirmer, E. C. and Heras, J. I. d. l., editors (2014). *Cancer Biology and the Nuclear Envelope: Recent Advances May Elucidate Past Paradoxes*. Advances in Experimental Medicine and Biology. Springer-Verlag, New York. 92

Schoenwaelder, S. M. and Burridge, K. (1999). Bidirectional signaling between the cytoskeleton and integrins. *Current Opinion in Cell Biology*, 11(2):274–286. 94

Style, R. W., Boltyanskiy, R., German, G. K., Hyland, C., MacMinn, C. W., Mertz, A. F., Wilen, L. A., Xu, Y., and Dufresne, E. R. (2014). Traction force microscopy in physics and biology. *Soft Matter*, 10(23):4047. 92

Svitkina, T. (2018). The Actin Cytoskeleton and Actin-Based Motility. *Cold Spring Harbor Perspectives in Biology*, 10(1):a018267. 94

Swift, J., Ivanovska, I. L., Buxboim, A., Harada, T., Dingal, P. C. D. P., Pinter, J., Pajerowski, J. D., Spinler, K. R., Shin, J.-W., Tewari, M., Rehfeldt, F., Speicher, D. W., and Discher, D. E. (2013). Nuclear Lamin-A Scales with Tissue Stiffness and Enhances Matrix-Directed Differentiation. *Science*, 341(6149):1240104. WOS:000323652300034. 92

Taber, L. A. (1995). Biomechanics of Growth, Remodeling, and Morphogenesis. *Applied Mechanics Reviews*, 48(8):487–545. 106

Vassaux, M. and Milan, J. L. (2017). Stem cell mechanical behaviour modelling: substrate's curvature influence during adhesion. *Biomechanics and Modeling in Mechanobiology*, 16(4):1295–1308. 97

Versaevel, M., Grevesse, T., and Gabriele, S. (2012). Spatial coordination between cell and nuclear shape within micropatterned endothelial cells. *Nature Communications*, 3:671. 92

Wakatsuki, T. (2003). Mechanics of cell spreading: role of myosin II. *Journal of Cell Science*, 116(8):1617–1625. 93

Wang, H., Biao, Y., Chunlai, Y., and Wen, L. (2017). Simulation of AFM indentation of soft biomaterials with hyperelasticity. In *2017 IEEE 12th International Conference on Nano/Micro Engineered and Molecular Systems (NEMS)*, pages 550–553. 105

Zeng, X. and Li, S. (2011). Multiscale modeling and simulation of soft adhesion and contact of stem cells. *Journal of the Mechanical Behavior of Biomedical Materials*, 4(2):180–189. 97, 98, 105

Chapter IV

Conclusion and Perspectives

Cell migration is a very exciting topic in the light of biomechanics. It is under very strict scrutiny from experimental biologists in order to unveil the signaling pathways that regulate it. However, when it comes to a multi-material object submitted to various internal and external forces, a mechanical modeling approach sheds a new light on this complex phenomenon. To tackle the challenges raised by confinement (i.e. contact, friction, adhesion forces, as well as active strain from actin polymerization and acto-myosin contractility), we decided to model the cell in the framework of confined migration.

Thesis review

Cell migration in confinement is such an intricate phenomenon, that one model cannot account for all of its aspects. It rather needs to be divided into smaller problems first, that can later be congregated. In this thesis, we thus broach three distinct problems revolving around confined cell migration : the mechanical behaviour of the nucleus, the workings of adhesion-free chimneying migration, and cell spreading on a micro-pillared substrate. All our models feature a generic cell rather than a specific cell type and can be adapted to fit a specific phenotype by adapting the mechanical parameters.

First, during migration through tight constrictions, as would occur in the mesh of the extra-cellular matrix, the nucleus has a crucial role due to its size and stiffness. Observations have revealed a plastic behaviour that makes it easier for the cell to pass through consecutive constrictions. To analyze the influence of such behaviour, we design a visco-elasto-plastic model of the nucleus that we validate against the literature in a compression test. Then, we implement it in a viscoelastic model of the cell passively flowing through a constriction in a perfusion experiment. Our model unveils an interesting mechanical interplay where the cytoplasm can "pull" on the nucleus and regulate its shape, which meets experimental observations from the literature.

Then, for the cell to squeeze through tight gaps, it requires adaptation. It can alter the mechanical behaviour of its constituents, such as the nucleus, but it can also adapt its migration mode to the surrounding environment. In the chimneying mode, the cell does not form any adhesions with its environment, but pushes against the confining walls to generate friction. Our model succeeds in showing that rear active contraction, coupled with a poroelastic description of the cytoplasm and the friction force against the walls are mechanically sufficient for the cell to efficiently move forward. The synchronization between active strains and external forces is managed here by the friction force itself: it is completely self-regulated in this regard, which is a great step towards a more autonomous model.

Micro-pillared substrates are a great tool to study cell confined migration *in vitro*. Before migration begins, the cell spreads on the pillars and its nucleus somehow ends up deformed in the pits between the pillars. In the third chapter, we then develop a complete cell model with an adhesive spreading force to test whether the nucleus is being pushed from above by the perinuclear actin cap or pulled down by actin fibers towards the pillars. We first validate our model on a flat substrate. Then, we test three configurations : "Push" only, "Pull" only and "Push & Pull". As it turns out, the pulling force is much stronger than the pushing one and the "Pull only" case is almost as efficient as the "Push & Pull" one. The nucleus then appears to be mostly pulled town towards the substrate. Besides, our model mechanically validates that gravity is not responsible for the deformation of the nucleus.

All in all, our models are great tools to confront experimental hypotheses and offer a new type of information about the cell. They allow us to apprehend the keys to cell migration with a mechanical perspective. They are all built on a common foundation made of three columns: a material characteristic law to describe the cell and its nucleus, active strains in the cell, and their synchronization with the external forces acting on the cell. Each of these columns can be suited to a specific situation through different bricks. We developed three models here, for three different situations. However, based on this common foundation, we could address many more problems where mechanics is involved.

Modeling perspectives

In this work, we chose to have an exploratory strategy. That is to say, we developed the tools to model three separate issues rather than perfect a single, "polished" model. We thus designed various bricks that will be of use for future work. As mentioned earlier, our models are based on three columns and the perspective developments can be classified along those same lines: the characteristic behaviour of the cell, the active strains, and their synchronization with the external forces on the cell.

To begin with the characteristic behaviour of the cell, it would be interesting to assemble the bricks of the material laws and build a unified model of the passive cell, featuring no active strains or external forces. In our first model, we developed a visco-elasto-plastic material law for the nucleus in small deformations. In the second one, we developed a poroelastic model of the cell in small deformations. In the third one, we eventually tackled the issue of large deformations through a Lagrangian formulation and implemented a visco-hyperelastic description of the cell and its nucleus. A combined model would then be made of a poro-hyperelastic cytoplasm and a visco-hyperelasto-plastic nucleus. It could be used to characterize the passive behaviour of the cell, taking into account the interstitial fluid transport in the cytoplasm, as well as the plasticity of the nucleus. This passive unified model would be the basis of further active development. We could broaden the model with the different kinds of active strains and external forces that we developed: polymerizing or contractile strains, repulsive contact, friction, and adhesive spreading. In the case of adhesive migration between pillars for instance, the poroelasticity of the cytoplasm could lead to a "piston effect" of the nucleus that would be highly interesting to study. Besides, nuclear plasticity would certainly be relevant since the cell would go through successive constrictions.

Looking at the active strains in the cell, there are two types of deformations. Protrusive ones, that symbolize the polymerization of the filamentous actin network, and contractile ones, that depict the acto-myosin dynamics. In our previous and current works, the active strains were controlled by pre-established functions. These functions were designed to fit the modeled situation but were disconnected from the internal biology of the cell. In reality, complex interactions between filamentous actin, globular actin, microtubules, myosin and other regulatory proteins occur in the cell. This internal dynamic drives the formation of protrusions and the cell's contractility. An interesting development of our model would be to include a self-regulation of myosin-based contractility (and extend it to actin polymerization) through Partial Differential Equations (PDEs) describing the internal molecular dynamics of the cell. Such chemo-mechanical approaches have already been developed in the literature. It would not be a far stretch to implement it in our model. Then, the active strains could directly be controlled by these PDEs and this multi-physics model would be less user-driven and more autonomous.

The next bolt to unlock in order to move towards a fully autonomous model is the self-synchronization of active strains with the external forces generated by the environment. In previous adhesive migration models, as well as in the cell spreading model, the protrusion and contraction phases are governed by user defined synchronization functions. Only in our poroelastic model of chimneying are the contractile strains self-synchronized with the friction force through the mechanical description of friction itself. This autonomous regulation is however what we aim to achieve in all our models. Looking at our cell spreading model for instance, we controlled the succession of the phases by Heaviside functions purely dependant on time and not on any physical parameter. As we saw in the literature, the active spreading phase only starts once the cells has passively spread beyond a certain point. We could then imagine a Heaviside function with a threshold defined not by time but by the contact area between the cell and the substrate. Likewise, the contractile phase could be triggered by the spreading state of the cell rather than by a mere time threshold. If all active phases of our models were controlled in such a manner, they could be fully autonomous, regulating themselves depending on their current mechanical state. In the context of my master's thesis at the TU Wien, we developed a model of semi-confined migration with self-regulated protrusive and retractile phases based on the contact state with the confining micro-channel (see Fig. IV.1 and Appendix A.4). The active phases were regulated by a combination of Heaviside functions defining the start and stop conditions for protrusion and retraction. These conditions were based on the current state of the cell (which part was protruded or retracted) and on the detection of sufficient contact with the confining wall. This model successfully managed to adapt its behaviour to pass a local expansion of the channel, showing the feasibility of this approach and the promises it holds.

To put it in a nutshell, we have most necessary tools to implement a unified autonomous multi-physics cell model. We could take into account the plasticity of the nucleus and the interstitial fluid flows of a visco-hyperelastic cell. The active strains could be "biologized" by regulating protrusion and contraction through PDEs accounting for the cell's internal molecular dynamics. Eventually, the synchronization between active processes and external forces or mechanical state of the cell could be achieved by using Heaviside step functions linked to physical parameters that will naturally evolve during the simulation. All the models we developed so far are 2D, or even 1D in the case of chimneying. For cell spreading over micro-pillars at least, the 2D reduction might be too restrictive to capture all aspects of the problem. Indeed, the third dimension may facilitate nuclear deformation in the pits since it would not be constrained in this direction. It would thus be necessary to develop our model in 3D for it to faithfully reproduce the mechanical behaviour of the cell in a given situation. Eventually, our models do not account for substrate deformability. It is probably irrelevant in the case of perfusion, but might have a greater impact on the behaviour of our system for chimneying and spreading on micro-pillars. As it goes, the ECM fibers on which the cell may push or pull *in vivo* are compliant and the surrounding environment can be deformed by the cell, thus influencing the migratory dynamics.

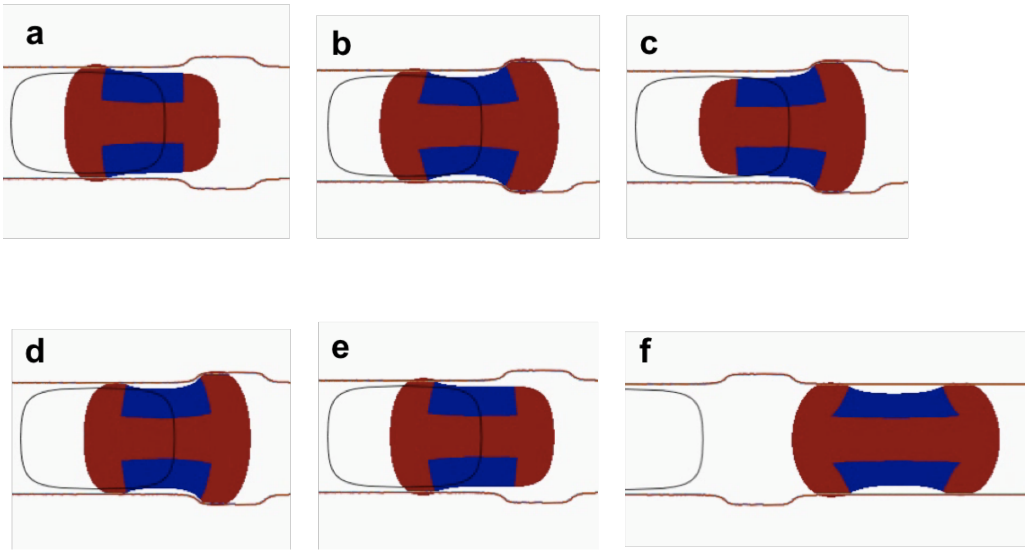

Figure IV.1: Numerical simulation of a self-synchronized pseudo-confined cell migration model. The red parts indicate the active segments of the cell while the blue parts are passive. Once the cell rear pushes on the micro-channel walls to anchor itself (a), the front part starts protruding until it pushes hard enough on the walls (b). Once the front is anchored, the rear retracts (c) and then protrudes again (d). The front can thus retract (e) and the cycle resumes. Thanks to the self-synchronization, the protrusion length adapts to the surrounding geometry and the model is then able to pass a local expansion of the channel.

Experimental perspectives

We have developed very interesting models, offering new insights on the mechanics of the cell, particularly in the context of confined migration. However, we must not forget that our *in silico* approach must be confronted to the *in vivo* reality. The results of a model can only be trusted as long as you trust the initial hypotheses feeding that model. We saw it through parametric studies: the outcome of the model directly depends on the mechanical parameters taken in input. The question is: do we trust our inputs ? Let's take the examples of the constitutive law describing the cell's parts and the mechanical parameters of such laws. Looking in the literature, research groups have developed all sorts of material laws to describe the cell: power law rheology, visco-elastic, hyperelastic or poroelastic for instance. It would be deluding to think that one is right and everyone else is wrong. They probably all tell something of the very complex behaviour of the cell. Models are often fitted to an experiment to prove their validity. But, if we fit a model on an experiment, it should be no surprise that it predicts correctly the experimental results. How should we proceed then ? One could fit a model on an experiment, and then challenge it on a different experiment to check its validity. Models designed this way can nevertheless be somewhat disconnected from the physical reality of the cell. In this respect, we took the stand to build a structure-based model. That is to say, we started from the cell's internal structure to build a reasonable mechanical model and then confronted this model to experimental results.

The constitutive law is one thing, but there is still the question of the choice of the mechanical parameters. Changing from one cell type to another, the mechanical properties will not be the same. In simulation, that would not be a problem since we could simply adjust the parameters of the model. If we choose one cell phenotype, various methods can be used to characterize it, but all of them are necessarily biased in a way. Indeed, by probing a spread cell for example, we might sense the stiffness of the actin network resulting of the spreading process. Since cells adapt to their surrounding, it is hard to know if we measure the actual cell property or the one resulting from such adaptation. In general, these methods are reliable to give relative values, but we must keep in mind that the absolute values might be biased. Besides, even inside a single cell line, there is a great variably of its properties over two to three orders of magnitude. This may explain why the absolute values of the mechanical parameters found in the literature present such inconsistency. One lead to minimize this effect would be to design experimental setups that allow good reproducibility. The Jan Lammerding Lab, for instance, is developing micro-fluidic devices containing 18 micro-pipettes per device, so that 18 experiments can be done in the very same conditions (unpublished work). Eventually, I think it is fairly honest to assume that we cannot trust the absolute values taken as inputs for our models. But what can we make of this ? We strongly believe mechanical models have a lot to offer in this area. We can actually do reverse engineering and test various parameters and find which ones give the most coherent results compared to the experiments. The values we find to be acceptable are often in the lower range of what can be described in the literature, reinforcing our belief that experimentally probed cells might stiffen as a result of the probing setup.

The last question now is: what is the long-term goal of this kind of research? Cell migration has become a thoroughly researched topic due to its implications in cancer metastasis. Currently, cancer is mostly being treated by surgery, chemo- or radiotherapy, and often a combination of those. But these methods are very aggressive on the body. Chemotherapy, for instance, targets all fast-dividing cells, which includes cancer cells but, unfortunately, also healthy ones. Recent advances have seen the development of immunotherapies and targeted therapies. Immunotherapy targets the immune system to boost it in its fight against cancer, while targeted therapy technically is a chemotherapy refined to specifically target cancerous cells only. The world of cancer treatments is rapidly evolving and current drugs mostly target cells' inner workings. But, seeing the importance of cell mechanics during confined migration and thus cancer metastasis, we can imagine future treatments that could focus on the cells' mechanical pathways in order to exacerbate or inhibit specific phenomena.

Appendices

Appendix A

Activity Portfolio

A.1 Teaching activities

During the three years of my thesis, I was a teaching assistant at CentraleSupélec for the following courses:

Mechanics - Bachelor students: 25 hours per year of tutorial in continuum solid mechanics, beams and point dynamics

Biomechanics - Master students: 36 hours per year of practical work on biomechanical materials (material characterization, finite elements modeling, CT scan analysis, porosimetry tests analysis and microscope observations)

Micro-Electro-Mechanical Systems (MEMS) - Master students: 36 hours per year of supervising numerical modeling projects using COMSOL Multiphysics software. The aim is to design a MEMS and to study the Multiphysics interactions using finite elements.

Besides, I also supervised a Bachelor project of a 6-students team on the optimization of isolation and resistance properties of latex gloves for an electricity distribution company.

A.2 Coursework

In order to sharpen my professional project after my thesis, I enlisted for a 3 years-long doctoral program at the Institut de Formation Supérieure Biomédicale (I.F.S.B.M.), from the Université Paris-Sud. This program allowed me to discover the medical and clinical world through various themes, all applied to cancer:

- Medical innovation in Biotech & Medtech companies (21h)
- The art of scientific presentation (21h)
- Introduction to Hematology & Immunology (17h)
- Cancer treatment and management (21h)
- Medical imaging research : principles and practical work (36h)
- Medical technologies and health care organization in peri-operative medicine (21h)
- Getting started in health care: research and industrial landscape (21h)
- Prosthetic joint replacement (16h)
- Bio-Design & Bio-Engineering (14h)

I also followed an English course on "Presenting your research" and a seminar on "Ethics in research".

A.3 Research collaboration

From the beginning of my thesis, we collaborated with Jan Lammerding, from the Lammerding Lab at Cornell University, USA. His lab's work on the nuclear lamina and the nuclear deformation of cancer cells during confined migration were of great interest for us. I was invited to spend three months at the Lammerding Lab in 2016, which was a great opportunity for me to discover experimental biology. During this exchange, I learned how to do cell culture, and how to fabricate the microfluidic devices used in the lab. I designed my own experiments in order to study the influence of the pressure drop in a micro-pipette aspiration device on nuclear deformation in wild-type and lamin-deficient Mouse Embryo-Fibroblasts (MEFs). During my stay, I encountered various problems, the biggest one being mislabelled cells. Despite the short duration of my stay, I experienced first hand some of the possible problems and bias of experimental work. Overall, this helped me develop a more critical approach of experimental literature.

A.4 Publications

1. Collaboration with the Lammerding Lab for an article on an innovative multiple micro-pipette aspiration device. We validated their device by modeling the flux inside of it, *under construction.*

2. Mondésert-Deveraux, S., Aubry, D., and Allena, R. (2018). In silico approach to investigate nucleus behaviour during cell spreading over micropillared substrates. *Submitted to Physical Biology*

3. Mondésert-Deveraux, S., Allena, R., and Aubry, D. (2018). A coupled friction-poroelasticity model of chimneying shows that confined cells can mechanically migrate without adhesions. Molecular & Cellular Biomechanics, vol.15, no.3, pp.1-22, *Accepted*

4. Deveraux, S., Allena, R., and Aubry, D. (2017). A numerical model suggests the interplay between nuclear plasticity and stiffness during a perfusion assay. Journal of Theoretical Biology, 435:62–77. 88, 89, 91, 97, 106

5. Deveraux, S., (2016). Mechanical models of confined cell migration. AV Akademikerverlag. ISBN: 978-3-639-87239-2. *Master's thesis*

A.5 Conference presentations and posters

I had the chance to participate and present my work in many international conferences:

10th European Solid Mechanics Conference - July 2018

Oral presentation of a visco-hyperelastic model of cell spreading on a micro-pillared substrate

MultiBioMe 2017, ECCOMAS Thematic Conference - September 2017

Oral presentation of a poroelastic cell model during confined bleb-based migration

7th European Cell Mechanics Meeting - June 2017

Poster entitled “Cytoplasm stiffness can reverse nuclear plasticity in lamin deficient cells” - *Best Poster Award*

22nd Congress of the European Society of Biomecanics - July 2016

Poster entitled “Experimental validation of a confined migration cell model during amoeboid migration”

ECCOMAS Congress - June 2016

Oral presentation of a poroelastic model of a cell during chimneying migration through a micro-channel

MECAMAT Congress on human and animal tissues - January 2016

Poster entitled "How can cancerous cells invade a healthy tissue?"

40th Congress of the French Society of Biomechanics - October 2015

Oral presentation of a visco-elasto-plastic model of the cell nucleus in compression

4th International CMBBE Conference - June 2015

Oral presentation of mechanical models of bleb-based migration in pseudo and fully confined medium

Appendix B

Résumé de la thèse

La capacité de migrer activement à travers l'organisme est une des propriétés fondamentales des cellules. De l'embryogénèse à la métastase tumorale, certaines cellules sont capables de se déplacer à travers le corps afin de remplir des missions bien particulières. Dans un organisme sain il s'agit de maintenir l'homéostasie de celui-ci. Mais si la fonction migratoire est altérée, des cellules cancéreuses peuvent devenir agressives et des métastases peuvent se disséminer dans l'organisme. Lors de la migration, les cellules subissent d'importantes déformations lorsqu'elles doivent se faufiler à travers des constrictions très étroites. Puisque la mécanique est très impliquée dans le processus migratoire, nous pouvons nous demander : qu'est-ce qu'une modélisation numérique de la mécanique de la migration peut nous apprendre sur ce phénomène ? Nous avons par conséquent choisi d'implémenter des modèles en éléments finis afin d'explorer différents aspects de la migration.

Si nous nous intéressons de plus près à la cellule, deux structures sont impliquées de manière très importante dans le processus de migration : le noyau et le cytosquelette. Le noyau est à la fois le plus gros et le plus rigide des organelles de la cellule. Lorsque la cellule migre et doit se déformer, il est un frein au mouvement car il se déforme moins facilement que le cytoplasme. À l'inverse, le cytosquelette est le moteur de la migration. C'est en effet la polymérisation de filaments d'actine et la présence de fibres contractiles d'acto-myosine qui vont permettre à la cellule de créer et rétracter des protrusions et de contracter des parties du cytoplasme. Outre la contraction et la polymérisation, le troisième pilier de la migration est la formation d'adhésions entre la cellule et son environnement. Si elle n'est pas ancrée, la cellule ne fait que pulser sur place, sans générer de mouvement net. Ces trois piliers sont présents de manière plus ou moins importante selon le mode de migration choisi par la cellule, puisque cette dernière peut adapter son comportement à son environnement. Elle peut alors passer d'un mode migratoire à un autre en favorisant l'un ou l'autre de ces piliers.

Dans cette thèse, nous nous efforcerons de répondre à trois questions autour de la migration cellulaire. Soulevées dans la littérature expérimentale, ces interrogations se prêtent particulièrement bien à une étude numérique :

1. Quel est le rôle de la plasticité du noyau dans la migration confinée ?
2. 1. Par quel mécanisme une cellule peut-elle avancer lors de la migration confinée non-adhésive appelée ‘chimneying’ ?
3. Sur un substrat microstructuré avec des piliers, comment le noyau de la cellule peut-il se déformer et se placer dans les creux ?

Chacune de ces questions nous a permis de développer un point de modélisation pertinent. Tous les modèles développés reposent cependant sur un même socle, et c’est bien là la puissance de cet outil : un modèle de base qui nous permet d’étudier trois problèmes différents, et qui pourrait être décliné pour de nombreux autres. Les briques constituant ce socle sont (i) la loi constitutive du matériau, (ii) les déformations actives dans la cellule et (iii) la synchronisation entre ces déformations et les forces extérieurs appliquées à la cellule.

Le premier chapitre présente un modèle visco-élasto-plastique du noyau de la cellule. Un noyau plastique faciliterait en effet la migration à travers des constrictions multiples en gardant une déformation résiduelle après la première constriction. Afin de supprimer tout interférence possible entre le comportement du noyau et les déformations actives du cytoplasme, ce modèle a été testé dans deux cas purement passifs. Nous avons d’abord simulé un test d’écrasement du noyau isolé du reste de la cellule. Une fois le comportement plastique de notre modèle validé, nous avons implémenté un modèle de cellule complète, avec un cytoplasme viscoélastique. Nous avons ensuite simulé un test de perfusion, dans lequel la cellule passe à travers une constriction de taille sub-nucléaire sous l’action d’un flux liquide. Deux tailles de constrictions ont été testées : 5 et 1 μm de diamètre (sachant que le noyau a un diamètre de 8 μm). En ajustant les paramètres mécaniques du modèle, nous avons pu tester deux lignées cellulaires : une lignée "contrôle" et une lignée où la lamina est affaiblie, rendant ainsi le noyau moins rigide. Dans la constriction la plus large, le noyau ne se déforme pas suffisamment pour observer une déformation plastique. Cette plasticité est cependant observée avec la constriction de 1 micron. Il est intéressant de noter qu’elle disparaît lorsque la lamina est affaiblie. Il semblerait alors que le cytoplasme vienne "tirer" sur le noyau pour inverser la déformation plastique. Il y a donc là une interaction mécanique fondamentale entre le cytoplasme et le noyau

Le deuxième chapitre aborde un mode migratoire appelé chimneying. Dans ce cas, la cellule confinée migre sans adhérer à son environnement. Ce mode est également particulier puisqu’il n’y a aucune polymérisation de filaments d’actine ; la seule déformation active est une contraction à l’arrière de la cellule. Une hypothèse généralement avancée pour expliquer le chimneying est le couplage entre un comportement poroélastique du cytoplasme et la friction contre les parois environnantes. En effet, les flux de fluide interstitiel dans le cytoplasme semblent avoir un rôle majeur lors de la migration confinée. Nous choisissons alors une description poroélastique du cytoplasme afin de rendre compte de ces flux et de leur influence mécanique. Par ailleurs, si la cellule ne forme pas d'adhésions, elle doit cependant s'ancrer d'une manière ou d'une autre pour ne pas osciller sur place. L'hypothèse du chimneying est donc qu'en poussant contre les parois qui la confinent, la cellule génère des forces de friction suffisantes pour ne pas glisser. Le modèle implémenté repose donc sur la loi de comportement poroélastique du cytoplasme, la contraction active de l'arrière de la cellule et la force de friction. Si, pour des raisons numériques, nous avons ici choisi un modèle 1D, la force de ce modèle réside dans l'auto-synchronisation entre la friction et les déformations actives. En effet, dans les travaux précédant cette thèse, la synchronisation était pilotée manuelle et nous avons donc franchi un pas ici vers un modèle plus autonome. Par ce modèle, nous montrons donc mécaniquement que la simple contraction arrière, couplée à la friction et à la poroélasticité suffisent à créer un mouvement net vers l'avant.

Enfin, dans le troisième chapitre, nous nous sommes intéressés à l'étalement de la cellule sur un substrat microstructuré. Afin d'étudier la migration cellulaire, de nombreux dispositifs micro-fluidiques existent. Des substrats microstructurés avec des piliers ont récemment été développés afin d'étudier le processus de déformation du noyau pendant la phase d'étalement qui précède la migration. Lorsque la cellule s'étale sur les piliers, on observe une déformation du noyau qui vient alors se placer dans les creux entre les piliers. La question posée est alors celle du mécanisme à l'origine de cette déformation du noyau. Dans les cellules étalées, il y a une forte concentration d'actine autour des piliers ainsi qu'au-dessus du noyau. Le noyau pourrait donc être tiré par les fibres d'actine vers les piliers ou bien poussé par la contraction du dôme d'actine qui le surplombe. Le modèle développé dans ce chapitre nous permet également de valider que la gravité n'est pas responsable de la déformation du noyau. Les briques qui composent ce modèle sont : une loi de comportement visco-hyperélastique de type Mooney-Rivlin, une contraction active dans chacune des zones à tester et les forces extérieures (i.e. la force d'étalement et celle de contact). Notre modèle montre alors que les filaments qui tirent le noyau vers les piliers sont bien plus puissants que le dôme d'actine.

Nous montrons ici que notre modèle de base peut se décliner selon différents cas à simuler. Sa versatilité est un atout puisque cela permet de le confronter à de nombreuses expériences. Ici, nous avons voulu explorer trois situations très différentes. L'étape suivante consisterait à synthétiser nos résultats en un seul modèle qui pourrait alors aborder la migration cellulaire de manière très concrète. Couplé avec une approche plus moléculaire, cela permettrait d'avoir une vision plus ample de ce processus. Un tel modèle permettrait de mieux comprendre les phénomènes multiphysiques qui régissent la migration cellulaire, et d'appliquer ces connaissances dans un cadre médical. Dans le cas des métastases tumorales, on pourrait alors imaginer développer de nouveaux types de médicaments qui cibleraient les propriétés mécaniques des cellules ou de leur environnement.

List of Figures

université PARIS-SACLAY

ÉCOLE DOCTORALE
Sciences mécaniques et énergétiques, matériaux et géosciences (SMEMAG)

Modélisation de la mécanique de la cellule et son noyau dans le cadre de la migration confinée

Mots clés : Mécanique cellulaire, Déformations active, Plasticité du noyau, Migration chimneying, Étalement

Résumé : Les cellules possèdent une capacité fondamentale à leur survie : la migration. De l'embryogénèse aux métastases tumorales, lors de la migration, les cellules doivent se faufiler à travers des mailles sub-nucléaires pour atteindre leur localisation cible. Pour ce faire, elles peuvent adapter leur mode locomotion ou leurs propriétés mécaniques à l'environnement qui les entoure. La cellule ainsi que son noyau subissent d'importantes déformations lors de la migration en milieu confiné. Le noyau étant l'organelle le plus gros et le plus rigide, il peut limiter la capacité migratoire de la cellule. Ses propriétés mécaniques sont donc décisives afin de migrer à travers un environnement complexe. Dans la littérature, les signaux moléculaires pendant le processus migratoire ont été abondamment décrits, mais la modélisation mécanique d'une cellule en migration peut-elle nous révéler de nouveaux éléments sur les mécanismes sous-jacents ?

La migration cellulaire est un procédé d'une complexité mécano-biologique telle, que tous ses aspects ne peuvent être modélisés à ce jour. Nous en choisissons donc trois que nous développerons ici. Nous nous intéressons d'abord à l'interaction mécanique entre le noyau et le cytoplasme lors d'une constriction de la cellule, puisque la plasticité du noyau semble avoir un rôle primordial. Nous étudions ensuite le chimneying, un mode migratoire sans adhésion dont le mécanisme repose sur des forces de friction couplées à la poroélasticité du cytoplasme. Enfin, les substrats avec des micro-piliers sont depuis peu utilisés pour étudier les propriétés mécaniques de la cellule et de son noyau, mais la mécanique de ce phénomène est peu comprise. Nous modélisons le processus par lequel le noyau se déforme afin de déterminer s'il est poussé ou tiré dans l'espace inter-piliers.

Modeling cellular and nuclear mechanics in the context of confined migration

Keywords: Cell mechanics, Active strain, Nuclear plasticity, Chimneying migration, Spreading

Abstract: One of the fundamental properties in cells is their ability to migrate. From embryogenesis to tumor metastasis, migrating cells must overcome mechanical obstacles to reach their intended location, squeezing through sub-cellular and sub-nuclear gaps. It can be done by adapting the locomotion mode to the surrounding environment or by tuning the cell's own mechanical properties. Migrating in a confined space leads to intensive deformation of the cell and thus its nucleus. Being the largest and stiffest organelle, the nucleus can hamper the migratory process. Its mechanical properties hence are key to a successful migration in a complex environment. Molecular signals behind cell migration have been extensively studied in the literature, but what can computational mechanics modeling unveil about the mechanisms behind cell migration?

Cell migration is such a complex mechano-biological process, that all aspects cannot be modeled at once for now. We choose three distinct situations for in-depth study. We first seek to understand the mechanical interplay between the nucleus and the cytoplasm, since nuclear plasticity seems decisive for migration through sub-nuclear gaps. Second, we investigate the mechanics of chimneying, a specific confined migratory mode, in which no adhesion in needed for the cell to move forward. Poroelasticity, coupled with friction, appears as the key to successful locomotion. Eventually, cell spreading on micro-pillared substrates has recently been developed to study nuclear mechanical properties. The mechanism behind this process being however unclear, we designed a large deformation model to determine whether the nucleus is being pushed or pulled in the inter-pillars gaps.